

CONCEPTS OF HEAVY-ION PHYSICS*

Ulrich Heinz

Department of Physics, The Ohio State University, Columbus, OH 43210, USA

Abstract

In these lectures I present the key ideas driving the field of relativistic heavy-ion physics and develop some of the theoretical tools needed for the description and interpretation of heavy-ion collision experiments.

1 PROLOGUE: THE BIG BANG AND THE EARLY UNIVERSE

Matter as we know it, made up from molecules which consist of atoms which consist of electrons circling around a nucleus which consists of protons and neutrons which themselves are bound states of quarks and gluons, has not existed forever. Our universe originated in a “Big Bang” from a state of almost infinite energy density and temperature. During the first few microseconds of its life the energy density in our universe was so high that hadrons (color singlet bound states of quarks, antiquarks and gluons), such as the nucleons inside a nucleus, could not form. Instead, the quarks, antiquarks and gluons were deconfined and permeated the entire universe in a thermalized state known as **quark-gluon plasma** (QGP). Only when the energy density of the universe dropped below the critical value $e_{\text{cr}} \simeq 1 \text{ GeV/fm}^3$ and its temperature decreased below $T_{\text{cr}} \approx 170 \text{ MeV}$, colored degrees of freedom became confined into color singlet objects of about 1 fm diameter: the first hadrons formed.

After the universe hadronized, it took another 200 s or so until its temperature dropped below $\sim 100 \text{ keV}$ such that small atomic nuclei could form and survive. This is known as *primordial nucleosynthesis*. At this point (i.e. after “The First 3 Minutes”) the chemical composition of the early universe was fixed (“**chemical freeze-out**”). All unstable hadrons had decayed and all antiparticles had annihilated, leaving only a small fraction of excess protons, neutrons and electrons, with all surviving neutrons bound inside small atomic nuclei. The chemical composition of the universe began to change again only several hundred million years later when the cores of the first stars ignited and nuclear fusion processes set in.

After primordial nucleosynthesis the universe was still ionized and therefore completely opaque to electromagnetic radiation. About 300 000 years after the Big Bang, when the temperature had reached about 3000 K, electrons and atomic nuclei were finally able to combine into electrically neutral atoms, and the universe became transparent. At this point the electromagnetic radiation decoupled, with a perfectly thermal blackbody spectrum of $T \approx 3000 \text{ K}$ (“**thermal freeze-out**”). Due to the continuing expansion of our universe this thermal photon spectrum has now been redshifted to a temperature of about 2.7 K and turned into the “cosmic microwave background”. The number of photons in this microwave background is huge (about 250 photons in every cm^3 of the universe), and they carry the bulk of the entropy of the universe. The entropy-to-baryon ratio of the universe is $S/A \simeq 10^{9\pm 1}$; its inverse provides a measure for the tiny baryon-antibaryon asymmetry of our universe when it hadronized – a still incompletely understood small number.

The only other surviving feature of the Big Bang is the ongoing **Hubble expansion** of our universe, and the structure of its density fluctuations, amplified over eons by the action of gravity and reflected in today’s distribution of stars, galaxies, galactic and supergalactic clusters, and dark matter. Using these 3 or 4 observational pillars (today’s expansion rate or “Hubble constant”, the microwave background spectrum and its fluctuations, the primordial nuclear abundances and, most recently, also today’s spectrum

*These lecture notes are an expanded version of the lectures I gave a year earlier at the 2002 European School of High-Energy Physics in Pylos (Greece) whose proceedings were published as a CERN Yellow Report (CERN-2004-001, N. Ellis and R. Fleischer, eds.). The online version of these lecture notes on the arXiv has most graphs presented in color.

of density fluctuations) together with the equations of motion of general relativity, we have been able to reconstruct the cosmological evolution of our universe from its origin in the Big Bang. However, try as you want, we will never be able to directly see anything that happened before 300 000 years after the Big Bang, due to the opacity of the Early Universe. In particular, the all-permeating quark-gluon plasma which filled our universe during the first few microseconds will always remain hidden behind the curtain of the cosmic microwave background. This is where relativistic heavy-ion collisions come in: It turns out that we can recreate this thermalized QGP matter (or at least some decent approximation to it) by colliding large nuclei at high energies. To elaborate on this is the subject of these lectures.

2 A FEW IMPORTANT RESULTS FROM LATTICE QCD

2.1 Lattice QCD in 3 minutes

We know from lattice QCD that the quark-gluon plasma exists (see Ref. [1] for a recent review). Lattice QCD is a method for calculating equilibrium properties of strongly interacting systems directly from the QCD Lagrangian by numerical evaluation of the corresponding path integrals. One starts from the vacuum-to-vacuum transition amplitude in the Feynman path integral formulation

$$Z = \int \mathcal{D}A_\mu^a(x) \mathcal{D}\bar{\psi}(x) \mathcal{D}\psi(x) e^{i \int d^4x \mathcal{L}[A_\mu^a, \bar{\psi}, \psi]}, \quad (1)$$

where the phase factor depending on the classical action $\int d^4x \mathcal{L}[A, \bar{\psi}, \psi]$ is integrated over all classical field configurations for the gluon fields, $A_\mu(x)$, and quark and antiquark fields, $\psi(x)$ and $\bar{\psi}(x)$. The path integral is dominated by those field configurations $(A_\mu(x), \bar{\psi}(x), \psi(x))$ which minimize the classical action and render the phase factor stationary, i.e. which satisfy the classical Euler-Lagrange equations of motion. These classical solutions define the classical chromodynamic field theory. Dirac and Feynman showed that integrating over *all* field configurations instead of only the solutions of the classical equations of motion produces the corresponding quantum field theory. The Pauli principle for fermions is implemented by postulating that the classical fermion fields $\psi(x)$ and $\bar{\psi}(x)$ are Grassmann variables satisfying $\psi(x_1)\psi(x_2) + \psi(x_2)\psi(x_1) = 0$ etc.

Starting from Eq. (1), one obtains an expression for the grand canonical partition function of an ensemble of quarks, antiquarks and gluons in thermal equilibrium by an almost trivial step: One replaces time t everywhere by imaginary time τ , $t \rightarrow i\tau$, and restricts the integration range over τ in the action to the interval $[0, \beta = \frac{1}{T}]$ where T is the temperature of the system:

$$\mathcal{Z} = \int \mathcal{D}A_\mu^a(\mathbf{x}, \tau) \mathcal{D}\bar{\psi}(\mathbf{x}, \tau) \mathcal{D}\psi(\mathbf{x}, \tau) e^{-\int_0^\beta d\tau \int d^3x \mathcal{L}_E[A_\mu^a, \bar{\psi}, \psi]}. \quad (2)$$

The origin of this replacement is the realization that the partition function is defined as $\mathcal{Z} = \text{tr } \hat{\rho}$ and that the density operator $\hat{\rho} = e^{-\beta \hat{H}}$ for the grand canonical thermal equilibrium ensemble looks just like the time-evolution operator $e^{i\hat{H}t}$ in the vacuum theory, with t replaced by $i\beta$. The *Euclidean* Lagrangian density $\mathcal{L}_E[A, \bar{\psi}, \psi]$ arises from the normal QCD Lagrangian

$$\mathcal{L}_{\text{QCD}} = -\frac{1}{4}F_{\mu\nu}^a F_{\mu\nu}^a + i\bar{\psi}\gamma^\mu \left(\partial_\mu - ig\frac{\lambda_a}{2}A_\mu^a \right) \psi - m\bar{\psi}\psi, \quad (3)$$

with the non-Abelian gluon field strength tensor

$$F_{\mu\nu}^a = \partial_\mu A_\nu^a - \partial_\nu A_\mu^a + gf_{abc}A_\mu^b A_\nu^c, \quad (4)$$

by replacing $\partial_t = -i\partial_\tau$ as well as $A_0^a = iA_4^a$ and $j_0^a = ij_4^a$ (where $j_\mu^a = g\bar{\psi}\gamma_\mu \frac{\lambda_a}{2}\psi$ is the color current vector of the quarks), and summing Lorentz indices over 1 through 4 (instead of 0 through 3) with unit metric tensor. In addition, in order to preserve the invariance of $\mathcal{Z}[A, \bar{\psi}, \psi] = \text{tr } \hat{\rho}[\hat{A}, \hat{\bar{\psi}}, \hat{\psi}]$ under cyclic permutations of the field operators under the trace, the classical gluon fields in the path integral must

be periodic in imaginary time, $A_\mu^a(\mathbf{x}, \tau) = A_\mu^a(\mathbf{x}, \tau + \beta)$, whereas the Grassmannian fermion fields obey antiperiodic boundary conditions, $\psi(\mathbf{x}, \tau) = -\psi(\mathbf{x}, \tau + \beta)$ etc. Note that τ is not really a time, it only plays a similar formal role in the path integral as real time does at zero temperature; a system in global thermal equilibrium is completely time independent.

Similar to Eq. (2) one can write down a path integral for the thermal equilibrium ensemble average $\langle \hat{O} \rangle = \text{tr}(\hat{\rho} \hat{O})$ of an arbitrary observable $\hat{O}[\hat{A}, \hat{\bar{\psi}}, \hat{\psi}]$ which depends on the quark and gluon fields:

$$\langle \hat{O} \rangle = \frac{\int \mathcal{D}A_\mu^a(\mathbf{x}, \tau) \mathcal{D}\bar{\psi}(\mathbf{x}, \tau) \mathcal{D}\psi(\mathbf{x}, \tau) O[A, \bar{\psi}, \psi] e^{-\int_0^\beta d\tau \int d^3x \mathcal{L}_E[A, \bar{\psi}, \psi]}}{\int \mathcal{D}A_\mu(\mathbf{x}, \tau) \mathcal{D}\bar{\psi}(\mathbf{x}, \tau) \mathcal{D}\psi(\mathbf{x}, \tau) e^{-\int_0^\beta d\tau \int d^3x \mathcal{L}_E[A, \bar{\psi}, \psi]}}. \quad (5)$$

Here $O[A, \bar{\psi}, \psi]$ is the *classical* observable, expressed through the *classical* fields $A_\mu^a(\mathbf{x}, \tau)$, $\psi(\mathbf{x}, \tau)$ and $\bar{\psi}(\mathbf{x}, \tau)$.

So far this expression is exact. Since the QCD Lagrangian is bilinear in the quark fields, the path integral over the Grassmann field variables can be done analytically, resulting in an infinite-dimensional determinant over all space-time points:

$$\langle \hat{O} \rangle = \frac{\int \mathcal{D}A_\mu(\mathbf{x}, \tau) \tilde{O}[A] \det \left[i\gamma^\mu \left(\partial_\mu - ig \frac{\lambda_a}{2} A_\mu^a \right) - m \right] e^{-\int_0^\beta d\tau \int d^3x \mathcal{L}_E[A]}}{\int \mathcal{D}A_\mu(\mathbf{x}, \tau) \det \left[i\gamma^\mu \left(\partial_\mu - ig \frac{\lambda_a}{2} A_\mu^a \right) - m \right] e^{-\int_0^\beta d\tau \int d^3x \mathcal{L}_E[A]}}. \quad (6)$$

Here $\mathcal{L}_E[A] = -\frac{1}{4} F_{\mu\nu}^a F_a^{\mu\nu}$ is the purely gluonic part of the euclidean QCD Lagrangian, and $\tilde{O}[A]$ arises from $O[A, \bar{\psi}, \psi]$ when doing the Gaussian integral over ψ and $\bar{\psi}$.

The words *Lattice QCD* stand for an algorithm to numerically evaluate this path integral, by discretizing space and time into $N_s^3 N_\tau$ space-time lattice points, evaluating the corresponding $N_s^3 N_\tau$ -dimensional fermion determinant, and integrating over the 4×8 gluon fields A_μ^a from $-\infty$ to ∞ at each of the $N_s^3 N_\tau$ lattice points. The integrals are performed by Monte Carlo integration, using the Metropolis method of importance sampling. This method works well as long as the fermion determinant is positive. This is indeed the case for the expression given in Eq. (6) for the grand canonical ensemble at zero chemical potential. It describes a quark-gluon plasma with vanishing net baryon density, which is a good approximation for the Early Universe. Heavy-ion collisions, on the other hand, involve systems with non-zero net baryon number, brought into the collision by the colliding nuclei. This requires introduction of a baryon chemical potential μ_B which enters into the fermion determinant in Eq. (6) with a factor i and leads to oscillations of the latter. The resulting “sign problem” has been a stumbling block for lattice QCD at finite net baryon density for almost 25 years, and only recently significant progress was made, resulting in first lattice QCD results for the hadronization phase transition in a quark-gluon plasma with nonzero baryon chemical potential [2] (although still limited to $m_B \lesssim 3T_{\text{cr}}$ [3]).

2.2 Color deconfinement and chiral symmetry restoration

For our discussion two observables are of particular importance: the *Polyakov loop operator*

$$L = \frac{1}{3} \text{tr} \left(\mathcal{P} e^{ig \int_0^\beta A_4(\mathbf{x}, \tau) d\tau} \right) \quad (7)$$

(where $A_4 = A_4^a \frac{\lambda_a}{2}$ is a 3×3 matrix and \mathcal{P} stands for path ordering), and the scalar quark density $\bar{\psi}(x)\psi(x)$. Due to translational invariance of the medium both have \mathbf{x} -independent thermal expectation values which, however, show a strong temperature dependence. This is shown in Fig. 1. The argument of the exponential function in the Polyakov loop operator L is gauge-dependent although L itself is not (due to the trace and the periodicity condition $A_4^a(\mathbf{x}, \beta) = A_4^a(\mathbf{x}, 0)$); we can thus choose a gauge in which its τ -dependence vanishes. It can then be interpreted as the interaction energy of

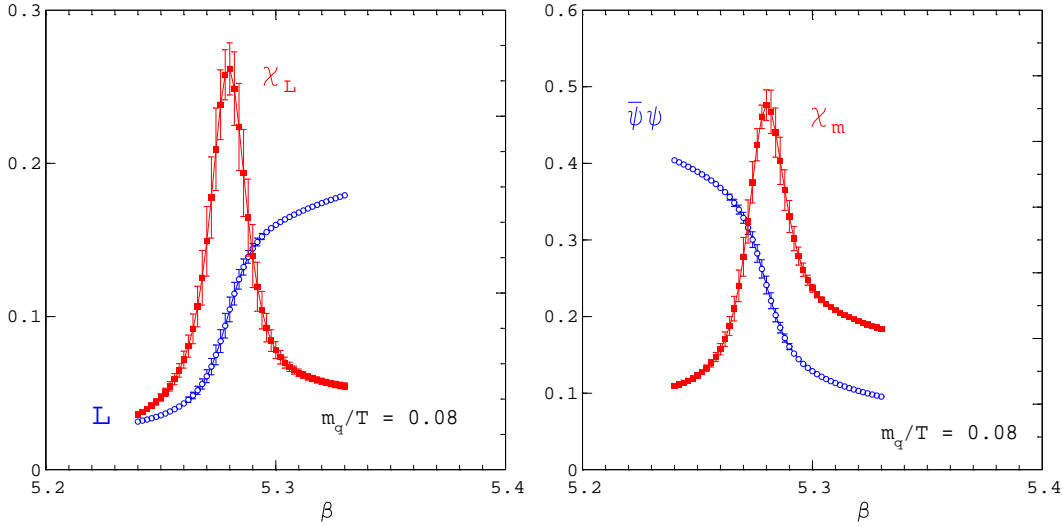


Fig. 1: Left: Polyakov loop expectation value $\langle L \rangle$ and its temperature derivative (Polyakov loop susceptibility χ_L) as a function of the lattice coupling $\beta = 6/g^2$ which is monotonically related to the temperature T (larger β correspond to larger T). Right: The chiral condensate $\langle \bar{\psi}\psi \rangle$ and the negative of its temperature derivative (chiral susceptibility χ_m) as a function of temperature. (From Ref. [4].)

an infinitely heavy quark at position \mathbf{x} (whose euclidean color current density four-vector is given by $J_\mu^a(y) = ig \frac{\lambda_a}{2} \delta(\mathbf{y}-\mathbf{x}) (1, 0, 0, 0)$) with the gluon field $A_\mu^a(y)$:

$$e^{ig \int_0^\beta d\tau A_4(\mathbf{x}, \tau)} = e^{ig\beta A_4^a(\mathbf{x}) \frac{\lambda_a}{2}} = e^{-\beta H_{\text{int}}} \quad (8)$$

where

$$H_{\text{int}} = -L_{\text{int}} = \sum_{\mu=1}^4 \int d^3y J_\mu^a(\mathbf{y}) A_\mu^a(\mathbf{y}) = \int d^3y J_4^a(\mathbf{y}) A_4^a(\mathbf{y}) = ig \frac{\lambda_a}{2} A_4^a(\mathbf{x}). \quad (9)$$

A vanishing thermal expectation value $\langle L \rangle$ of the Polyakov loop operator thus indicates infinite energy for a free quark, i.e. quark confinement. The left panel of Fig. 1 shows this to be the case at small temperatures. However, as the temperature increases, $\langle L \rangle$ increases rapidly to a nonzero value at high temperatures, with a relatively sharp peak of its derivative at a critical coupling β_{cr} . This indicates that quark confinement is broken at the corresponding critical temperature T_{cr} .

In the right panel of Fig. 1 we see that at low temperatures the scalar quark density has a nonvanishing expectation value (“chiral condensate”) which evaporates above a critical coupling. Again the corresponding susceptibility shows a relatively sharp peak, at the same value β_{cr} . In the absence of quark masses the QCD Lagrangian is chirally symmetric, i.e. invariant under separate flavor rotations of right- and left-handed quarks. Since the up and down quark masses in \mathcal{L}_{QCD} are very small, neglecting them is a good approximation. The nonvanishing chiral condensate at $T=0$ breaks this chiral symmetry and generates a dynamic mass of order 300 MeV for the quarks; the corresponding “constituent” masses in vacuum are thus about 300 MeV for the up and down quarks and about 450 MeV for the strange quark (whose bare mass in \mathcal{L}_{QCD} is already about 150 MeV). According to the right panel of Fig. 1 the dynamically generated mass melts away at T_{cr} , making the quarks light again above T_{cr} : the approximate chiral symmetry of QCD is restored.

Obviously deconfinement and chiral symmetry restoration happen at the same critical temperature T_{cr} . Figure 1 shows this for one specific, temperature-dependent value of the quark mass used in the lattice calculation ($m_q = 0.8 T$). This value is unrealistically large, but calculations with realistic and temperature-independent masses are very costly and not yet available. Instead, one repeats the calculations for several unrealistically large masses and tries to extrapolate to zero mass. The perfect coincidence of the peaks in the chiral and Polyakov loop susceptibilities is seen for all quark masses [4] and thus expected to survive in the chiral limit.

Both deconfinement and chiral symmetry restoration are phenomenologically important. Deconfinement leads to the liberation of a large number of gluons which can produce extra quark-antiquark pairs and drive the system towards chemical equilibrium among quarks, antiquarks and gluons. The melting of the dynamical quark masses above T_{cr} makes the quarks lighter and lowers the quark-antiquark pair production threshold. This is particularly important for strange quarks whose constituent quark mass is much higher than the critical temperature while its current mass is comparable to T_{cr} . Above T_{cr} thermal processes are therefore much more likely to equilibrate strange quark and antiquark abundances during the relatively short lifetime time of a heavy-ion collision.

The dissolution of massive hadrons into almost massless quarks and gluons at T_{cr} leads to a very rapid rise of the energy density near the deconfinement transition. This is shown in Fig. 2. For a massless

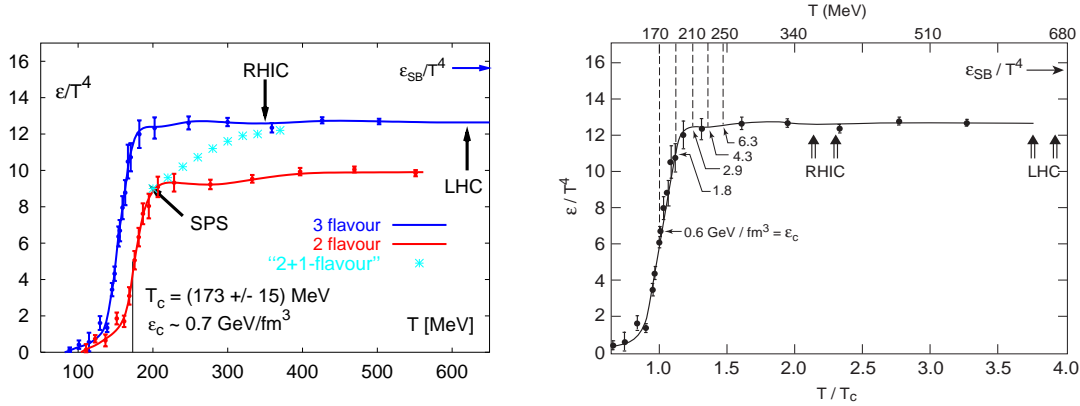


Fig. 2: Energy density in units of T^4 for QCD with two and three dynamical quark flavors [5, 6]. (The symbol ϵ is here used for the energy density e .) The curves labelled “2 flavour” and “3 flavor” were calculated for two and three light quark flavors of mass $\frac{m_q}{T} = 0.4$, respectively. “2+1 flavour” indicates a calculation for two light and one heavier strange quark flavor of $\frac{m_q}{T} = 1$. In this case the ratio ϵ/T^4 interpolates between two light flavors at $T \lesssim T_{\text{cr}}$ and three light flavors at $T \gtrsim 2T_{\text{cr}}$ [6]. For 2 and 2+1 flavors the critical temperature is $T_{\text{cr}} = 173 \pm 15 \text{ MeV}$ [6]. The right figure indicates, for the case of 3 light flavors, absolute values for the energy density ϵ at several temperatures.

gas of quarks and gluons the energy density is proportional to T^4 . The proportionality constant reflects the number of massless degrees of freedom, multiplied by $\frac{\pi^2}{30}$ for bosons and by $\frac{7}{8} \frac{\pi^2}{30}$ for fermions. The arrow in the upper right of Fig. 2 indicates this constant evaluated for 2(helicity) \times 8(color) = 16 gluon degrees of freedom plus 2(spin) \times 3(color) \times 3(flavor) \times 2($q + \bar{q}$) = 36 massless quark and antiquark degrees of freedom. We see that for $T < 4T_{\text{cr}}$ the lattice data remain about 20% below this Stefan-Boltzmann limit. Near T_{cr} the ratio e/T^4 drops rapidly by more than a factor 10. This is due to hadronization. The much heavier hadrons are exponentially suppressed below T_{cr} , leading to a much smaller number of equivalent massless degrees of freedom. (Due to the somewhat too large quark masses in the simulations presented in Fig. 2 this effect is slightly exaggerated.) According to Fig. 2 the critical energy density for deconfinement is about 0.6–0.7 GeV/fm^3 . The $\pm 15 \text{ MeV}$ uncertainty in T_{cr} induces a $\pm 40\%$ uncertainty in the critical energy density which could be as large as 1 GeV/fm^3 or as small as 500 MeV/fm^3 . I’ll use $e_{\text{cr}} = 1 \text{ GeV/fm}^3$ as a ball-park number. It is easy to remember because it is the energy density in the center of a proton and corresponds to one proton mass in a cube of 1 fm along each side.

The right panel of Fig. 2 also illustrates how painful the factor T^4 is: if we want to exceed the critical temperature by only 30% in order to reach the upper edge of the transition region, we already need an energy density $e \simeq 3.5 \text{ GeV/fm}^3$, five times the critical value! And to reach $2T_{\text{cr}}$ requires $e \simeq 23 \text{ GeV/fm}^3$. The former number is approximately the value one was able to reach at the CERN SPS in Pb+Pb collisions at $\sqrt{s_{\text{NN}}} = 17 \text{ GeV}$. The latter value has been achieved at the Relativistic Heavy Ion Collider (RHIC) in Au+Au collisions at $\sqrt{s_{\text{NN}}} = 130 \text{ GeV}$ (see later). An estimate where the Large Hadron Collider (LHC) at CERN will take us in 2008 is indicated near the right edge of the Figure. The corresponding energy densities are of the order of 500 GeV/fm^3 !

2.3 The QCD phase diagram and how to probe it with heavy-ion collisions

Figure 3 shows the phase diagram of strongly interacting matter in the temperature vs. baryon chemical potential plane (T, μ_B). Cold nuclear matter, such as in the interior of, say, a Pb nucleus, sits at $T = 0$ and $\mu_B \approx m_N = 940$ MeV. The short line emerging from this blob indicates the nuclear liquid-gas phase transition, with a critical endpoint at a temperature of about 7.5 MeV. At higher temperatures more and more hadron resonances are excited and we have a hadron resonance gas. From QCD lattice calculations we know the phase structure along the temperature axis, with the deconfinement transition from a hadron resonance gas to a quark-gluon plasma at $T_{cr} \approx 170$ MeV. Lattice QCD tells us that even for realistically small up and down quark masses the transition at $\mu_B = 0$ is most likely not a sharp phase transition but a rapid crossover as shown in Fig. 2 [6]. Phenomenological models have long indicated [7] that at non-zero μ_B the QGP and hadron gas are separated by a critical line of roughly constant critical energy density $e_{cr} \simeq 1$ GeV/fm³. Improved QCD inspired models [8] and recent lattice calculations at moderate non-zero baryon chemical potential [2, 3] indicate that the transition becomes first order at non-zero μ_B although the precise value where this happens still remains to be determined by performing calculations with more realistic smaller quark masses. At low temperatures and asymptotically large baryon densities quarks are also deconfined, although not in a quark-gluon plasma state but rather in a color superconductor [8]. The superconducting state is separated from the QGP by a first order transition at a critical temperature estimated to be of order 30-50 MeV [8]. Whether it has a direct transition to normal nuclear matter as indicated in my sketch or if other phases (e.g. involving pion or kaon condensates) intervene is presently not known. There exists a rich spectrum of theoretical possibilities [8, 9].

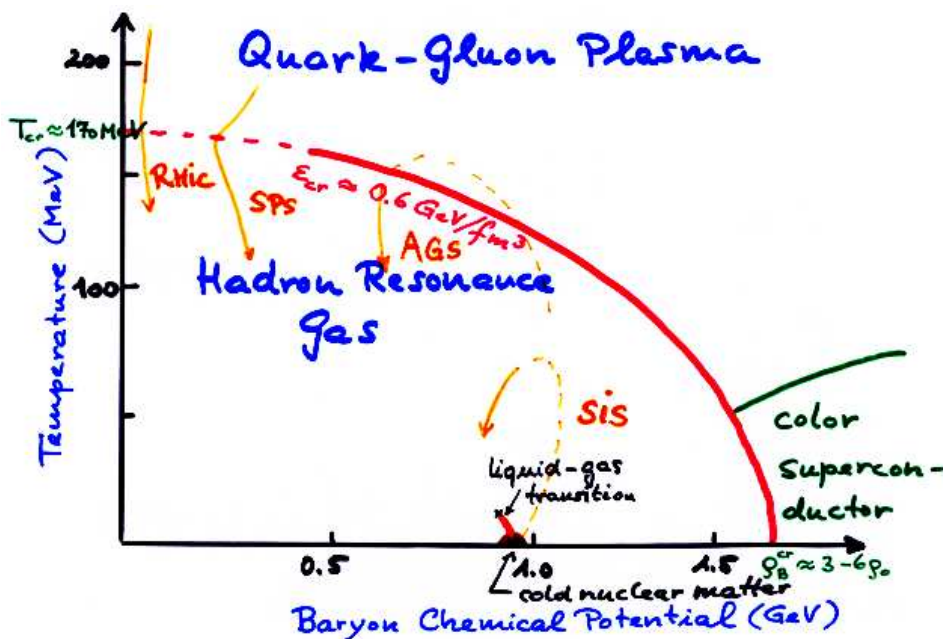


Fig. 3: The QCD phase diagram.

Figure 3 also indicates a few typical trajectories through the phase diagram which we can follow in relativistic heavy-ion collisions. The collisions start at the cold nuclear matter point in the phase diagram, go through an early non-equilibrium stage which can not be mapped onto the phase diagram (indicated by dotted lines), and then reappear in the phase diagram after having thermalized at some high temperature. Unfortunately, one cannot use heavy-ion collisions to compress nuclear matter without producing a lot of entropy and therefore also heating it; hence it seems impossible to probe with them the color superconducting phase of strongly interacting matter.

At the SIS (heavy-ion synchrotron) at the GSI facility in Darmstadt, with beam energies of order 1-2 GeV/nucleon, the center of mass collision energy is not large enough to reach the deconfined state

of QCD. At the Brookhaven AGS (beam energies of about 10 GeV/nucleon) we may have straddled the transition line. First clear indications that we had crossed into a new state of matter beyond the hadron resonance gas came from Pb+Pb collisions at 160 GeV/nucleon beam energy [10]. Au+Au collisions at RHIC thermalize at an initial temperature $T_0 \approx 2T_{\text{cr}}$ (see later). By collective expansion the collision fireball cools down and passes through the hadronization phase transition from above. In this sense heavy-ion collisions do not probe the *de-confinement*, but rather the *confinement* phase transition, just as the early universe. As the center of mass collision energy increases, the colliding nuclei become more and more transparent, meaning that a decreasing fraction of the beam energy and of the incoming baryons get stopped in the center of mass system. The midrapidity collision fireball therefore contains fewer and fewer of the incoming net baryons, becoming more and more baryon-antibaryon symmetric (i.e. μ_B decreases). At RHIC the entropy per baryon ratio is between 200 and 300, depending on collision energy. At the LHC one expects S/A to go up to several thousand. While still far from the early universe ratio of 10^9 , this is, for all practical purposes, “baryon-free” ($\mu_B = 0$) QCD matter.

3 THE DIFFERENT STAGES OF A HEAVY-ION COLLISION – THE LITTLE BANG

3.1 The production of hard probes during the early collision stage

Figure 4 summarizes the key stages of relativistic heavy-ion collisions: thermalization, expansion, and decoupling. In the very early collision stages, before the bulk of the quanta, which are created from the fraction of the beam energy lost in the collision, have time to rescatter, “hard” particles with either a large mass or large transverse momenta $p_{\perp} \gg 1 \text{ GeV}/c$ are created. Their creation involves large momentum transfers $Q^2 \sim p_{\perp}^2 \gg 1 \text{ GeV}^2$, therefore their production can be calculated in perturbative QCD, using factorization theorems, from the nuclear structure functions. According to the uncertainty relation hard particle *production* happens on a time scale $\tau_{\text{form}} \simeq 1/\sqrt{Q^2}$; for a 2 GeV particle this means $\tau_{\text{form}} \simeq 0.1 \text{ fm}/c$.

At SPS energies and below, hard particles are essentially only produced in the primary collisions between the projectile and target nucleons; the bulk of the produced particles have transverse momenta below $2 \text{ GeV}/c$ and are too soft to produce hard particles via secondary collisions. High- p_{\perp} jets from the fragmentation of hard partons have practically relevant cross sections only at RHIC energies and above. Once produced, one can use them to probe the soft matter created by the bulk of soft particles [11]: In a central collision between two Pb or Au nuclei the nuclear reaction zone has a transverse diameter of about 12 fm, so a hard particle created near the edge and moving in the “wrong” direction (namely straight inward) needs 12 fm/c before it emerges on the other side. During this time the soft matter thermalizes, expands, cools down and almost reaches decoupling, all of which is probed by the fast particle on its way to the other side. It does so by scattering off the evolving medium and losing energy which can be measured. The energy loss is proportional to the density of the medium times the scattering cross section between the probe and the medium constituents, integrated along the probe’s trajectory.

At SPS energies the “hardest” particles which can be produced and well identified by their distinctive decay pattern are $c\bar{c}$ pairs. If produced in a proton-proton collision where either no hot soft matter is created or the charmed quarks leave the region in which soft particles are formed before that happens, these charmed quarks and antiquarks form either a bound charmonium state (J/ψ , ψ' , or χ , “hidden charm” production) or they find light quark partners to hadronize into “open charm” states (D and \bar{D} mesons or charmed baryons). The corresponding branching ratios are well-known – the hidden charm states form a very small fraction (less than 1%) of all final states. If the $c\bar{c}$ pair is created in a heavy-ion collision, something similar as with the jets discussed above happens: the two heavy quarks have to travel through a dense medium of soft particles which interferes with their intention to hadronize and modifies their branching ratios into open and hidden charm states. In particular, if the soft medium thermalizes into a quark-gluon plasma, the color interaction between the c and \bar{c} is Debye screened by the colored quarks and gluons in the plasma, thereby prohibiting their normal binding into one of the charmonium states. This should cause “ J/ψ suppression” [12].

resulting from electromagnetic and weak decays of hadrons after hadronic freeze-out. This renders the measurement of these clean electromagnetic signals difficult.

3.2 Thermalization and expansion

The key difference between elementary particle and nucleus-nucleus collisions is that the quanta created in the primary collisions between the incoming nucleons can't right away escape into the surrounding vacuum, but rescatter off each other. In this way they create a form of dense, strongly interacting matter which, when it thermalizes quickly enough and at sufficiently large energy density, is a quark-gluon plasma. This is why with heavy-ion collisions we have a chance to recreate the matter in the very early universe whereas with high energy collisions between leptons or single hadrons we don't.

The produced partons rescatter both elastically and inelastically. Both types of collisions lead to equipartitioning of the deposited energy, but only the inelastic collisions change the relative abundances of gluons, light and strange quarks. (To also change the abundance of the heavier charm quarks ($m_c \simeq 1200$ MeV) requires secondary collisions of sufficient energy which do not happen at the SPS but may play a role at RHIC and above.) From the phenomenology of pp collisions it is known [14, 15] that the produced hadron abundances are distributed statistically, but that strange hadrons are systematically suppressed (probably because strange quarks are not present in the initial state and their large constituent mass of $\simeq 450$ MeV makes them hard to create from the vacuum as the produced partons hadronize). In a heavy-ion collision, if the reaction zone thermalizes at energy density $> e_{\text{cr}}$ such that gluons are deconfined and chiral symmetry is restored, strange quarks are much lighter ($m_s \simeq 150$ MeV) and can be relatively easily created by secondary collisions among the many gluons, leading to chemical equilibration between light and strange quarks [16]. The observed strangeness suppression in pp collisions should thus be reduced or absent in relativistic heavy-ion collisions [17].

A thermalized system has thermal pressure which, when acting against the surrounding vacuum, leads to collective (hydrodynamic) expansion of the collision fireball. As a consequence, the fireball cools and its energy density decreases. When the latter reaches $e_{\text{cr}} \simeq 1$ GeV/fm³, the partons convert to hadrons. During this phase transition the entropy density drops steeply over a small temperature interval (similar to the energy density shown in Fig. 2). Since the total entropy cannot decrease this implies that the fireball volume must increase by a large factor while the temperature remains approximately constant. The growth of the fireball volume takes time, so the fireball ends up spending significant time near T_{cr} . Furthermore, while the matter hadronizes its speed of sound $c_s = \sqrt{\partial p / \partial e}$ is small [6], causing inefficient acceleration so that the collective flow does not increase during this period. This may be visible in the direct photon spectrum: an inverse Laplace transform should show a particularly strong weight at the transition temperature, blueshifted by the prevailing radial flow as the system crosses T_{cr} [18]. The softness of the equation of state near the phase transition should also manifest itself in the center-of-mass energy dependence of the collective flow, as discussed later.

3.3 Hadronic freeze-out and post-freeze-out decays

After hadronization of the fireball, the hadrons keep rescattering with each other for a while, continuing to build up expansion flow, until the matter becomes so dilute that the average distance between hadrons exceeds the range of the strong interactions. At this point all scattering stops and the hadrons decouple ("freeze out"). Actually, their *abundances* already freeze out earlier when the rates for inelastic processes, in which the hadrons change their identity, become too small to keep up with the expansion. Since the corresponding inelastic cross sections are only a small fraction of the total cross section, inelastic processes stop long before the elastic ones, leading to earlier freeze-out for the hadron abundances than for their momenta: *chemical freeze-out* precedes *thermal* or *kinetic freeze-out*. What I call "elastic" includes resonant processes such as $\pi + N \rightarrow \Delta \rightarrow \pi + N$ where two hadrons form a short-lived resonance which subsequently decays back into the same particles (possible with different electric charge

assignments). Such processes don't change the finally observed chemical composition, but they contribute to the thermalization of the momenta and have large "resonant" cross sections. Since most of the hadrons in a relativistic heavy-ion fireball are pions (since they are so light), resonances with pions are very efficient in keeping the system in thermal equilibrium (even after chemical equilibrium has been broken). For scattering among pions the ρ resonance plays a large role while kaons and (anti)baryons couple to the pion fluid via the K^* , Δ and Y^* resonances. Due to the particularly large Δ and Y^* resonance cross sections, even at RHIC and LHC (where the net baryon density is small) baryon-antibaryon pairs play an important role as part of the "glue" that keeps the expanding pion fluid thermalized well below the chemical freeze-out point.

At kinetic freeze-out all hadrons, including the then present unstable resonances, have an approximately exponential transverse momentum spectrum reflecting the temperature of the fireball at that point, blueshifted by the average transverse collective flow. The unstable resonances decay, however, producing daughter particles with, on average, smaller transverse momenta. The experimentally measured spectra off stable hadrons cannot be understood without adding these decay products to the originally emitted spectra. Since most resonances decay by emitting a pion, this effect is particularly important for the pion spectrum which at low p_\perp are completely dominated by decay products. This seriously affects the slope of their spectrum out to $p_\perp \simeq 700$ MeV [19, 20], making it steeper than the blueshifted thermal spectrum of the directly emitted hadrons.

3.4 Theoretical tools

The idea that the parton production process factorizes into a perturbatively calculable "hard" QCD cross section and a non-perturbative, experimentally determined nuclear parton structure function (or parton distribution function) can be used to describe the initial production of hard partons, with $p_T > p_0$ where $p_0 \gtrsim 1-2$ GeV describes the lower applicability limit of this type of approach [21, 22]. The production of soft partons is usually non-perturbative and requires phenomenological models, such as string models [23], for their description. At very high collision energies particle production at midrapidity (i.e. particles with small longitudinal momenta in the center-of-momentum frame) probes the nuclear structure functions at small x where x is the fraction of the beam momentum carried by the partons whose collision produces the secondary partons. At small x the gluon distribution function becomes very big and gluons begin to fill the transverse area of the colliding nuclei densely [24, 25]. The gluons start to recombine, leading to gluon saturation, and low p_T gluon modes are occupied by a macroscopic number of gluons $\sim 1/\alpha_s$ where the effective strong coupling α_s is small due to the high density of gluons [26]. As a result, the initial gluons can be effectively described by a classical gluon field [26, 27] in which the coupling is weak but nonlinear density effects are important (this state has become known as the "color glass condensate" [28]). The production of soft secondary gluons can be understood as the liberation of these gluons by breaking the coherence of their multiparticle wavefunction [27, 29]. The collision energies where these modern ideas become applicable lie probably beyond the RHIC range, but this is an exciting and active field of ongoing research which may come to fruition at the LHC.

After the initial parton production or "liberation" process one must describe the rescattering and thermalization of the produced quanta. For not too dense systems this can be done with classical kinetic transport theory (relativistic Boltzmann equation), also known as parton cascade [30, 31]. In the early collision stages at RHIC and LHC energies the densities are probably too high for this to remain a reliable approach, and one must switch to quantum transport theory [32]. This formalism has not yet been developed very well for practical applications, and much interesting work is presently going on in this direction (e.g. [33, 34]). None of these approaches, which usually invoke perturbative QCD arguments to describe the microscopic scattering processes, has so far been able to produce parton thermalization time scales at RHIC which are shorter than about 5 fm/c [33]. This is too long for heavy-ion collisions whose typical expansion time scale (Hubble time) is only a couple of fm/c. As I will show later there is strong phenomenological evidence that thermalization must happen much more quickly. This presents

an interesting challenge for theory and indicates the importance of strong non-perturbative effects in the early collision stages and the QGP.

Once local thermal equilibrium has been reached, the further evolution can be described hydrodynamically. The simplest version of such an approach is ideal fluid dynamics which will be discussed in more detail later. The fireball can be described as an ideal fluid if the microscopic scattering time scale is much shorter than any macroscopic time scale associated with the fireball evolution. If this is not the case, one should include non-ideal effects such as shear, diffusion and heat conduction. This requires the calculation of the corresponding transport coefficients in a partonic system close to thermal equilibrium. Much work is going on in this direction (see e.g. [35, 36, 37]), but systematic approaches based on perturbatively resummed thermal QCD [35, 36, 37] give phenomenologically unacceptable large values for these transport coefficients, again indicating the importance of non-perturbative effects.

The hydrodynamic equations require knowledge of the equation of state, i.e. the relationship $p(e, n_B)$ between the pressure, energy density and baryon density. For small n_B this is known from lattice QCD; for large n_B one extrapolates the lattice results with phenomenological models (see [9] for a recent review). Hydrodynamics is the ideal language for relating observed collective flow phenomena to the equation of state. Since it only requires the equation of state but no detailed knowledge of the microscopic collision dynamics, it allows for an easy description of the hadronization phase transition without any need for a microscopic understanding of how hadrons form from quarks and gluons. Of course, the underlying assumption is that all these microscopic processes happen so fast that the system never strays appreciably from a local thermal equilibrium.

After hadronization the system continues to expand and dilute until the average distance between hadrons becomes larger than the range of the strong interaction. At this point the hadrons decouple, i.e. their momenta stop changing until they are recorded by the detector. One can implement this decoupling or “kinetic freeze-out” in different ways, either by truncating the hydrodynamic phase abruptly with the Cooper-Frye algorithm (see below) or by switching back from hydrodynamics to a (this time hadronic) cascade [38, 39, 40] in which decoupling happens automatically and selfconsistently. In the Cooper-Frye algorithm one also must take into account that in this approach all kinds of hadrons decouple simultaneously, and that unstable hadron resonances decay subsequently by strong (and in some situations also by weak) interactions before their stable daughter products reach the detector. To compute the measured spectra one must therefore fold the initially emitted Cooper-Frye hadron spectra with these decays [19]. Some studies, such as two-particle momentum correlations, also require the computation of long-range final state interaction effects, such as the Coulomb repulsion/attraction between charged hadrons which continues long after their strong interactions with each other have ceased.

3.5 Strategies for reconstructing the Little Bang

The bulk (over 99%) of the particles produced in heavy-ion collisions are hadrons. These are strongly interacting particles which cannot decouple from the fireball before the system is so dilute that strong interactions cease. Their observed momenta thus provide a snapshot of the kinetic decoupling stage (“thermal freeze-out”). In this sense hadrons are the Little Bang analogue of the cosmic microwave background in the Big Bang. As discussed in Sec. 3.3, hadron abundances freeze-out earlier. As we will see later, this “chemical freeze-out” happens right after hadronization, i.e. the finally observed hadron abundances are generated by the hadronization process itself. This *primordial hadrosynthesis* is the Little Bang analogue of primordial nucleosynthesis in the Big Bang. As the hadrons decouple, they carry not only thermal information about the prevalent temperature at chemical resp. thermal freeze-out, but in the momentum spectra this information is folded with (i.e. blueshifted by) the collective expansion flow, just as the temperature of the cosmic microwave radiation is redshifted by the cosmological expansion. The hydrodynamic expansion flow is the Little Bang analogue of the cosmic Hubble expansion in the Big Bang. (Of course, the origin of the expansion is entirely different in the two cases: in heavy-ion collisions it is generated hydrodynamically by pressure gradients whereas in the Big Bang it reflects an

initial condition, modified over billions of years by the effects of the gravitational interaction. But the velocity *profiles* turn out to be surprisingly similar, as we will see!)

We reconstruct the Little Bang from these “late” hadronic observables very much like we reconstructed the Big Bang from the 3 pillars of cosmology, Hubble expansion, CMB, and primordial nuclear abundances. The hadronic observables are abundant and can be measured with high statistical accuracy. As I will show, their theoretical analysis allows to separate the thermal from the collective motion. The collective flow provides a memory of the pressure and other thermodynamic conditions during the earlier collision stages. In fact, we will see that certain anisotropies in the flow patterns seen in non-central heavy-ion collisions (“elliptic flow”) provide a unique window into the very early collision stages and are no longer changed after about 5 fm/c after initial impact. As you will see, a (in my opinion) watertight proof for thermalization during this early stage, at a time $\tau_{\text{therm}} < 1$ fm/c and at prevalent energy densities which exceed the critical value e_{cr} for deconfinement by at least an order of magnitude, can be based on the accurately measured elliptic flow of the final state hadrons. (This is a bit analogous to the indelible imprint that cosmic inflation has left on the density fluctuations in the universe, which can be accurately measured through the anisotropy of the cosmic microwave radiation which only decoupled 300 000 years later.)

The reconstruction of the global space-time evolution of the reaction zone from the finally observed soft hadrons is the cornerstone of the program. The reconstructed dynamical picture will be the basis on which other rarer observables, in particular the “deep” or “hard” probes, will be interpreted. For example, jet quenching and heavy quarkonium suppression cannot be quantitatively interpreted without knowledge of the fireball density and its space-time evolution, and direct photon and dilepton spectra cannot be properly understood without a relatively accurate idea about the transverse flow patterns at the time of photon emission. Still, these probes will in the end be the only *direct access* we will ever have to the temperature and energy density at the beginning of the expansion when the system was a quark-gluon plasma, and although they cannot be fully interpreted and exploited without the later emitted soft particles they are still an indispensable part of the picture. This illustrates the network-like interdependence between soft and hard observables in their role for elucidating heavy-ion collision and quark-gluon plasma dynamics.

4 THE LITTLE BANG – COLLECTIVE EXPLOSION OF A THERMALIZED SYSTEM

An unavoidable consequence of quark-gluon plasma formation in heavy-ion collisions is collective flow. Since a quark-gluon plasma is by definition an (approximately) thermalized system of quarks and gluons, it has thermal pressure, and the pressure gradients with respect to the surrounding vacuum cause the quark-gluon plasma to explode. Absence of collective flow would indicate absence of pressure and imply absence of a hot thermalized system and, *a fortiori*, of a quark-gluon plasma.

In this chapter we’ll therefore do two things: (i) learn how to analyze the measured particle spectra for the presence of collective flow and how to separate it from random thermal motion, and (ii) compute the expected collective flow patterns from reasonable initial conditions using a hydrodynamic model. By comparing with experiments we can fine-tune the initial conditions, learn about the equation of state of the hot expanding matter and, most importantly, find out about when and at which energy densities the thermal pressure builds up and begins to drive the collective expansion.

4.1 Radial flow

4.1.1 Flow defined

Consider a nuclear fireball undergoing collective expansion. Collective flow is defined by the following operational procedure: at any space-time point x in the fireball, we consider an infinitesimal volume element centered at that point and add up all the 4-momenta of the quanta in it. The total 3-momentum \mathbf{P} obtained in this way, divided by the associated total energy P^0 , defines the average “flow” velocity $\mathbf{v}(x)$

of the matter at point x through the relation $\mathbf{P}/P^0 = \mathbf{v}$. Collective flow thus describes a correlation between the average momentum of the particles with their space-time position, a so-called *x-p-correlation*. With $\mathbf{v}(x)$ we can associate a normalized 4-velocity $u^\mu = \gamma(1, \mathbf{v})$ where $\gamma(x) = 1/\sqrt{1-\mathbf{v}^2(x)}$ is the corresponding Lorentz dilation factor and $u \cdot u = u^\mu u_\mu = 1$ (in units where the speed of light $c = 1$).

I separate the flow velocity $\mathbf{v}(x)$ into its components along the beam direction (“longitudinal flow” v_L) and in the plane perpendicular to the beam (“transverse plane”) which I call “transverse flow” \mathbf{v}_\perp . The magnitude v_\perp may depend on the azimuthal angle around the beam direction, i.e. on the angle between \mathbf{v}_\perp and the impact parameter \mathbf{b} of the collision. In this case we call the transverse flow “anisotropic”. Its azimuthal average we call *radial flow*.

4.1.2 Local thermodynamic equilibrium

If the fireball is in local thermodynamic equilibrium, we can not only define a local flow 4-velocity $u^\mu(x)$, but also a local temperature $T(x)$ and, for each particle species i , a chemical potential $\mu_i(x)$ which controls its particle density at point x . In this case the phase-space distribution of particles of type i is given by the Lorentz covariant local equilibrium distribution

$$f_{i,\text{eq}}(x, p) = \frac{g_i}{e^{[p \cdot u(x) - \mu_i(x)]/T(x)} \pm 1} = g_i \sum_{n=1}^{\infty} (\mp)^{n+1} e^{-n[p \cdot u(x) - \mu_i(x)]/T(x)}. \quad (10)$$

Here g_i is a spin-isospin-color-flavor-etc. degeneracy factor which counts all particles with the same mass m_i and chemical potential μ_i . The factor $p \cdot u(x)$ in the exponent is the energy of the particle in the local rest frame (local heat bath frame), boosted to the observer frame by the flow 4-velocity $u^\mu(x)$ of the fluid cell at point x ($p \cdot u \rightarrow p^0 = E$ when $u^\mu \rightarrow (1, \mathbf{0})$). The ± 1 in the denominator accounts for the proper quantum statistics of particle species i [upper (lower) sign for fermions (bosons)]. The Boltzmann approximation corresponds to keeping only the first term in the sum over n in the last expression. In our applications this is an excellent analytical approximation for all hadrons except for the pion. Pions and quarks and gluons are too light, $m_i \lesssim T$, and one must use the proper quantum statistical distributions.

4.1.3 Rapidity coordinates

At relativistic energies it is convenient to parametrize the longitudinal flow velocities and momenta in terms of rapidities (for any velocity v the associated rapidity is $\eta = \frac{1}{2} \ln \frac{1+v}{1-v}$ or $v = \tanh \eta$):

$$\eta_L = \frac{1}{2} \ln \frac{1+v_L}{1-v_L}, \quad y = \frac{1}{2} \ln \frac{1+\frac{p_L}{E}}{1-\frac{p_L}{E}} = \frac{1}{2} \ln \frac{E+p_L}{E-p_L}. \quad (11)$$

As $v_L \rightarrow 1$, $\eta_L \rightarrow \infty$. Rapidity has the advantage over longitudinal velocities that they are additive under longitudinal boosts: a fluid cell with flow rapidity η_L in a given inertial frame has rapidity $\eta'_L = \eta_L + \Delta\eta$ in another inertial frame which moves relative to the first frame with rapidity $\Delta\eta$ in the $-z$ direction. The flow 4-vector $(u^0, \mathbf{u}) = (u^0, \mathbf{u}_\perp, u_L)$ is then parametrized as

$$u^\mu = \gamma_\perp (\cosh \eta_L, v_x, v_y, \sinh \eta_L) \quad \text{with} \quad \gamma_\perp = \frac{1}{\sqrt{1-v_\perp^2}} = \frac{1}{\sqrt{1-v_x^2-v_y^2}} \quad (12)$$

where $\mathbf{v}_\perp = (v_x, v_y)$ is the transverse flow velocity. Similarly the 4-momentum $p^\mu = (E, \mathbf{p}_\perp, p_L)$ is written as

$$p^\mu = (m_\perp \cosh y, p_x, p_y, m_\perp \sinh y) \quad \text{with} \quad m_\perp = \sqrt{m^2 + p_\perp^2} = \sqrt{m^2 + p_x^2 + p_y^2} \quad (13)$$

which obviously satisfies the mass-shell constraint $p^2 = p^\mu p_\mu = m^2$. [We use the notations $p_\perp = p_T$ interchangeably for the transverse momentum, and similarly $m_T = m_\perp$ for the “transverse mass” – in

the literature one often also finds the notations p_t and m_t .] The scalar product $p \cdot u(x)$ in the exponent of the Boltzmann factor then becomes

$$p \cdot u = \gamma_{\perp} \left(m_{\perp} \cosh(y - \eta_L) - \mathbf{v}_{\perp} \cdot \mathbf{p}_{\perp} \right). \quad (14)$$

4.1.4 Longitudinal boost-invariance and Bjorken scaling

So far no approximations have been made as long as we allow \mathbf{v}_{\perp} and η_L to be arbitrary functions of $x^{\mu} = (t, \mathbf{r}_{\perp}, z)$ where $\mathbf{r}_{\perp} = (x, y)$ denotes the transverse coordinates. Things simplify, however, enormously if one assumes longitudinal boost-invariance. Bjorken [41] argued that at asymptotically high energies the physics of secondary particle production should be independent of the longitudinal reference frame. This condition can be easily expressed if one puts the nuclear collision at longitudinal position $z = 0$ and introduces, instead of z and t , the following “space-time rapidity” and “longitudinal proper time” coordinates to describe the forward light cone emanating from the collision point:

$$\eta = \frac{1}{2} \ln \frac{t+z}{t-z} = \frac{1}{2} \ln \frac{1+\frac{z}{t}}{1-\frac{z}{t}}, \quad \tau = \sqrt{t^2 - z^2}. \quad (15)$$

In these coordinates $x^{\mu} = (t, \mathbf{r}_{\perp}, z)$ reads $x^{\mu} = (\tau \cosh \eta, \mathbf{r}_{\perp}, \tau \sinh \eta)$, and the space-time integration measure takes the form $d^4x = \tau d\tau d\eta d^2r_{\perp}$. In a t - z -diagram, lines of constant space-time rapidity are rays through the origin with slope $1/\tanh \eta$. Longitudinal boost-invariance of particle production then implies that the initial conditions for local observables (such as particle and energy densities) are only functions of τ and \mathbf{r}_{\perp} , but independent of η [41]. Furthermore, the boost-invariance of these initial conditions is preserved in longitudinal proper time if the system expands collectively along the longitudinal direction with a very specific “scaling” velocity profile $v_L = \frac{z}{t}$ [41]. Inserting this into the definition (11) for the longitudinal fluid rapidity η_L and comparing with (15) we see that longitudinal boost-invariance implies the identity

$$\eta_L = \eta \quad (\text{Bjorken scaling}) \quad (16)$$

of the longitudinal fluid rapidity with the space-time rapidity. Since $\eta_L(x)$ characterizes the average longitudinal momentum of the produced particles at point x whereas η characterizes the coordinate x itself, this identity implies a very strong correlation between the average longitudinal momentum and the longitudinal position.

The Bjorken scaling approximation is expected to be good at high energies and not too close to the beam and target rapidities, i.e. in safe distance from the longitudinal kinematic limits. We will use it to describe particle production near midrapidity ($y \approx 0$ in the c.m. frame). As a result of Bjorken scaling, the Boltzmann exponent reduces to

$$p \cdot u(x) = \gamma_{\perp}(\mathbf{r}_{\perp}, \tau) \left(m_{\perp} \cosh(y - \eta) - \mathbf{p}_{\perp} \cdot \mathbf{v}_{\perp}(\mathbf{r}_{\perp}, \tau) \right). \quad (17)$$

Due to the additivity of rapidities, this is manifestly invariant under longitudinal boosts since it only involves rapidity differences. The transverse flow velocity, as well as the temperature T and chemical potential μ_i , are independent of η and depend only on the transverse position \mathbf{r}_{\perp} and longitudinal proper time τ .

4.1.5 The Cooper-Frye formula

Suppose we want to count the total number of particles of species i after produced in the collision. Since this number does not depend on the reference frame of the observer, we must be able to express it in a Lorentz-invariant way. We define a three-dimensional hypersurface $\Sigma(x)$ in 4-dimensional space-time along which we perform the counting. The simplest case would be a measurement in all space at a fixed

global time t . In a space-time diagram this would correspond to a horizontal line at fixed t . But this is not how a real detector works. In an ideal detector, we surround the collision region hermetically by detector elements which sit stationary at a fixed distance from the collision point, and we wait until the particles pass through these detector elements (which particles with different velocities will do at different times). Assuming, for example, a spherical detector of radius R , the corresponding detection hypersurface would in a (t, r) space-time diagram be represented by a vertical line at fixed $r = R$, extending from $t = -\infty$ to $t = \infty$. In this case the hypersurface is a 2-dimensional sphere extending over all time, i.e. it is again 3-dimensional.

You see that different choices for the 3-dimensional hypersurface Σ are possible as long as it completely closes off the future light cone emerging from the collision point. We count particles crossing the surface by subdividing it into infinitesimal elements $d^3\sigma$, defining an outward-pointing 4-vector $d^3\sigma_\mu(x)$ perpendicular to $\Sigma(x)$ at point x with the magnitude $d^3\sigma$, computing the scalar product of the 4-vector $j_i^\mu(x)$ describing the current of particles i through point x , and summing over all such infinitesimal hypersurface elements:

$$N_i = \int_{\Sigma} d^3\sigma_\mu(x) j_i^\mu(x) = \int_{\Sigma} d^3\sigma_\mu(x) \left(\frac{1}{(2\pi)^3} \int \frac{d^3p}{E} p^\mu f_i(x, p) \right). \quad (18)$$

The particle number current density $j_i^\mu(x)$ is given in terms of the Lorentz-invariant phase-space distribution (giving the probability of finding a particle with momentum p at point x) by multiplying it with the velocity $\frac{p^\mu}{E}$ and integrating over all momenta with measure $\frac{d^3p}{h^3} = \frac{d^3p}{(2\pi\hbar)^3}$ where $h = 2\pi\hbar = 2\pi$ is Planck's quantum of action and we are using units where $\hbar = 1$.

Dividing by the Lorentz-invariant momentum-space measure $\frac{d^3p}{E}$ (which in rapidity coordinates reads $dy p_\perp dp_\perp d\varphi_p = dy m_\perp dm_\perp d\varphi_p$ where φ_p is the azimuthal angle of \mathbf{p}_\perp) we obtain the invariant momentum distribution for particle species i :

$$E \frac{dN_i}{d^3p} = \frac{dN_i}{dy p_\perp dp_\perp d\varphi_p} = \frac{dN_i}{dy m_\perp dm_\perp d\varphi_p} = \frac{1}{(2\pi)^3} \int_{\Sigma} p \cdot d^3\sigma_\mu(x) f_i(x, p). \quad (19)$$

This is the **Cooper-Frye formula** [42]. One can show that two different surfaces Σ_1 and Σ_2 give the *same particle number* N_i if between Σ_1 and Σ_2 the distribution function $f_i(x, p)$ evolves via a Boltzmann equation with a collision kernel which preserves the number of particles i , and that we obtain the *same momentum spectrum* if and only if $f_i(x, p)$ evolves from Σ_1 to Σ_2 by free-streaming, i.e. if f_i is a solution of the collisionless Boltzmann equation. To compute the measured momentum spectrum we can therefore replace the surface Σ corresponding to the detector by shrinking it to the smallest and earliest surface that still encloses all scattering processes. We call this the “surface of last scattering” or “freeze-out surface” Σ_f .

Any 3-dimensional space can be parametrized by a set of three locally orthogonal coordinates u, v, w . The points on the surface $\Sigma(x)$ then have coordinates $\Sigma^\mu(u, v, w)$, $\mu = 0, 1, 2, 3$. The normal vector $d^3\sigma_\mu(x)$ is computed through the formula

$$d^3\sigma_\mu = -\epsilon_{\mu\nu\lambda\rho} \frac{\partial \Sigma^\nu}{\partial u} \frac{\partial \Sigma^\lambda}{\partial v} \frac{\partial \Sigma^\rho}{\partial w} du dv dw \quad (20)$$

where $\epsilon_{\mu\nu\lambda\rho}$ is the completely antisymmetric Levi-Civita symbol in four dimensions, with $\epsilon^{0123} = -\epsilon_{0123} = 1$. If we assume longitudinal boost-invariance, the freeze-out surface Σ_f can be characterized by a longitudinal proper time $\tau_f(\mathbf{r}_\perp)$ such that

$$\Sigma_f^\mu(\mathbf{r}_\perp, \eta) = (t_f, x_f, y_f, z_f) = \left(\tau_f(\mathbf{r}_\perp) \cosh \eta, \mathbf{r}_\perp, \tau_f(\mathbf{r}_\perp) \sinh \eta \right). \quad (21)$$

In this case

$$d^3\sigma_\mu = \left(\cosh \eta, -\frac{\partial \tau_f}{\partial x}, -\frac{\partial \tau_f}{\partial y}, -\sinh \eta \right) \tau_f(\mathbf{r}_\perp) d^2r_\perp d\eta, \quad (22)$$

and the integration measure in the Cooper-Frye formula (19) becomes (with $(\partial_x, \partial_y) = \nabla_\perp$)

$$p \cdot d^3\sigma(x) = \left(m_\perp \cosh(y-\eta) - \mathbf{p}_\perp \cdot \nabla_\perp \tau_f(\mathbf{r}_\perp) \right) \tau_f(\mathbf{r}_\perp) d^2r_\perp d\eta. \quad (23)$$

4.1.6 Thermal spectra from an exploding source

The local thermal equilibrium form (10) for the phase-space distribution is a good approximation as long as the particles rescatter intensely, i.e. as long as the relaxation time for returning to equilibrium is shorter than any macroscopic time scale which changes the parameters $T(x)$, $\mu_i(x)$ and $u^\mu(x)$. Use of Eq. (19) to compute the measured momentum spectrum requires knowledge of the phase-space distribution on the surface of last scattering, i.e. when all scattering has ceased. How can we relate the two? If the system expands very fast, its density decreases rapidly and the mean free path of the particles growth quickly. The transition from strong coupling to free-streaming thus happens in a short time interval. During this short time it is unlikely that the phase-space distribution undergoes qualitative changes, and we may approximate $f_i(x, p)$ on the last scattering surface by its thermal equilibrium form that it still had just a little earlier. This results in the famous Cooper-Frye freeze-out algorithm: determine the surface where local equilibrium *begins* to break down and use the local equilibrium distribution (10), with parameters $T(x)$, $\mu_i(x)$ and $u^\mu(x)$ determined on this surface, in Eq. (19) to compute the final momentum distribution. The result is [43, 44] (note that τ_f , T , μ_i , \mathbf{v}_\perp and γ_\perp are all functions of \mathbf{r}_\perp)

$$\begin{aligned} \frac{dN_i}{dy m_\perp dm_\perp d\varphi_p} &= \frac{g_i}{(2\pi)^3} \sum_{n=1}^{\infty} (\mp)^{n+1} \int d^2r_\perp \tau_f e^{n\mu_i/T} e^{n\gamma_\perp \mathbf{v}_\perp \cdot \mathbf{p}_\perp} \\ &\quad \times \int_{-\infty}^{\infty} d\eta \left(m_\perp \cosh(y-\eta) - \mathbf{p}_\perp \cdot \nabla_\perp \tau_f \right) e^{-n\gamma_\perp m_\perp \cosh(y-\eta)/T} \\ &= \frac{2g_i}{(2\pi)^3} \sum_{n=1}^{\infty} (\mp)^{n+1} \int d^2r_\perp \tau_f e^{n\mu_i/T} e^{n\gamma_\perp \mathbf{v}_\perp \cdot \mathbf{p}_\perp} \left(m_\perp K_1(n\beta_\perp) - \mathbf{p}_\perp \cdot \nabla_\perp \tau_f K_0(n\beta_\perp) \right), \end{aligned} \quad (24)$$

where $\beta_\perp(\mathbf{r}_\perp) \equiv m_\perp \frac{\gamma_\perp(\mathbf{r}_\perp)}{T(\mathbf{r}_\perp)}$. Due to the assumed boost-invariance, which allowed for an easy integration over η , this result is independent of rapidity y .

For central collisions ($b=0$) the fireball is azimuthally symmetric, so $\mathbf{v}_\perp = v_\perp \mathbf{e}_r$ and (in polar coordinates $\mathbf{r}_\perp = (r_\perp, \varphi_s)$) the functions τ_f , T , μ_i , v_\perp , γ_\perp are all independent of φ_s . This also implies $\nabla_\perp \tau_f = (\partial \tau_f / \partial r_\perp) \mathbf{e}_{r_\perp}$. The only angular dependences then arise from the scalar products $\mathbf{v}_\perp \cdot \mathbf{p}_\perp$ and $\mathbf{p}_\perp \cdot \nabla_\perp \tau_f$ which both involve the relative angle between \mathbf{p}_\perp and \mathbf{r}_\perp , i.e. $\cos(\varphi_s - \varphi_p)$. The azimuthal integral can thus be done analytically, producing another set of modified Bessel functions:

$$\begin{aligned} \frac{dN_i}{dy m_\perp dm_\perp} &= \frac{g_i}{\pi^2} \sum_{n=1}^{\infty} (\mp)^{n+1} \int_0^\infty r_\perp dr_\perp \tau_f e^{n\mu_i/T} \\ &\quad \times \left(m_\perp K_1(n\beta_\perp) I_0(n\alpha_\perp) - p_\perp \frac{\partial \tau_f}{\partial r_\perp} K_0(n\beta_\perp) I_1(n\alpha_\perp) \right), \end{aligned} \quad (25)$$

where $\alpha_\perp = \frac{\gamma_\perp v_\perp p_\perp}{T} = \alpha_\perp(r_\perp)$. For all hadrons except pions this can be used in the Boltzmann approximation, by keeping only the term $n=1$. The factor $\tau_f(r_\perp) e^{\mu_i(r_\perp)/T(r_\perp)} \equiv n_i(r_\perp)$ can be interpreted as the (unnormalized) radial density profile of the particles i . Introducing the *radial flow rapidity* ρ via $v_\perp = \tanh \rho$, which allows to write $\beta_\perp = \frac{m_\perp \cosh \rho}{T}$ and $\alpha_\perp = \frac{p_\perp \sinh \rho}{T}$, we then obtain the following “flow spectrum” [44, 45]:

$$\begin{aligned} \frac{dN_i}{dy m_\perp dm_\perp} &= \frac{g_i}{\pi^2} \int_0^\infty r_\perp dr_\perp n_i(r_\perp) \left[m_\perp K_1\left(\frac{m_\perp \cosh \rho(r_\perp)}{T(r_\perp)}\right) I_0\left(\frac{p_\perp \sinh \rho(r_\perp)}{T(r_\perp)}\right) \right. \\ &\quad \left. - p_\perp \frac{\partial \tau_f}{\partial r_\perp} K_0\left(\frac{m_\perp \cosh \rho(r_\perp)}{T(r_\perp)}\right) I_1\left(\frac{p_\perp \sinh \rho(r_\perp)}{T(r_\perp)}\right) \right]. \end{aligned} \quad (26)$$

This formula is useful because it allows to easily perform systematic studies of the influence of the radial profiles of temperature, density and transverse flow on the transverse momentum spectrum, in order to better understand which features of a real dynamical calculation of these profiles control the shape of the observed spectra. There are many such case studies documented in the literature (see, e.g., [45, 46]), and I will here discuss only the most important and generic characteristics.

4.1.7 How radial flow affects single-particle transverse momentum spectra

Since for all hadrons $m_{\perp}/T > 1$, the modified Bessel functions K_{ν} can be approximated by exponentials $\sim e^{-m_{\perp} \cosh \rho/T}$. The temperature on the freeze-out hypersurface is approximately constant [47, 48] since freeze-out is controlled by the mean free path which is inversely proportional to the density, which itself is a steep function of temperature [49]. Nevertheless, the flow spectra are characteristically curved, due to two effects: the influence of the I_{ν} Bessel functions at low p_{\perp} and the integration over the radial flow profile $\rho(r_{\perp})$.

Let us first see what kind of flow profiles we should consider. At $r_{\perp} = 0$ the radial flow velocity must vanish by symmetry; as you follow the freeze-out surface out to larger r_{\perp} , v_{\perp} typically rises linearly with r_{\perp} [47, 48, 39]. As shown in the right panel of Fig. 5, it eventually reaches a maximum value and drops again to zero since the dilute tail of the initial density distribution freezes out early

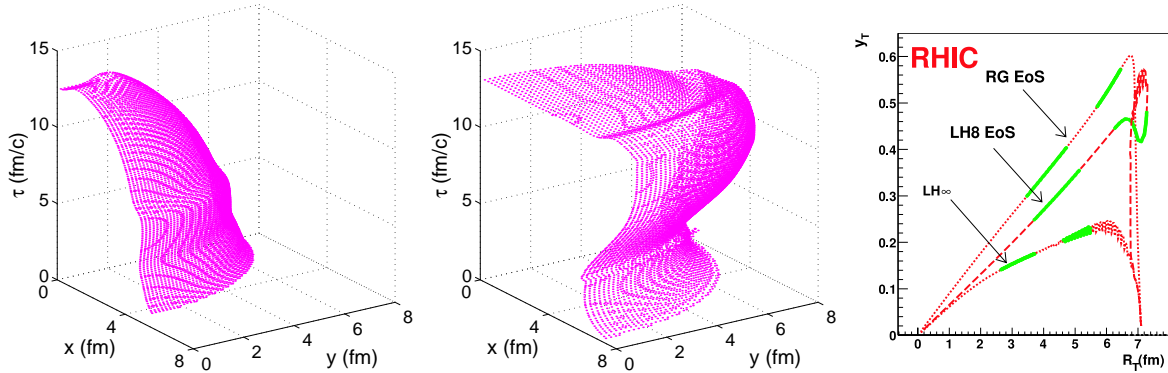


Fig. 5: Left panels: Hydrodynamical freeze-out surface $\tau_f(r_{\perp})$ for non-central Pb+Pb collisions at $b = 8$ fm (b points in x direction) with two different initial energy densities, one corresponding to SPS energies (left), the other corresponding to LHC energies (middle) [50]. Right panel: Radial flow rapidity profile $\rho(r_{\perp}) \equiv y_T(r_{\perp})$ for central Au+Au collisions at RHIC, from hydrodynamic calculations employing three different equations of state (for details see Ref. [39] from where this figure was taken).

before radial flow develops. The left two panels of Fig. 5 show typical freeze-out surfaces $\tau_f(r_{\perp})$ from hydrodynamic calculations (see later) for SPS (left) and LHC energies (middle) [50]. One sees that at SPS energies the freeze-out surface moves from the edge inward since the fireball matter cools and freezes out faster than the developing radial flow can push it out. At LHC energies things begin similarly, but then the much stronger radial flow generated by the much higher internal pressure makes the fireball grow considerably before suddenly freezing out after about 13 fm/c. The freeze-out surface for RHIC energies lies in between [51], with transverse flow almost exactly balancing freeze-out and leading to an almost constant freeze-out radius (also seen in the right panel of Fig. 5) until after about 12 fm/c it rather suddenly shrinks to zero, again indicating sudden bulk freeze-out.

So how does the radial flow affect the spectra? Looking at Eq. (reflowspec2) we see that in the absence of flow ($\rho = 0$) the second term vanishes (since $I_1(0) = 0$) and the first term simply becomes (for constant decoupling temperature)

$$\frac{dN_i}{dy m_{\perp} dm_{\perp}} \sim m_{\perp} K_1\left(\frac{m_{\perp}}{T}\right). \quad (27)$$

This depends only m_\perp (rather than on both m_\perp and $p_\perp = \sqrt{m_\perp^2 - m_i^2}$) and, except for the fact that m_\perp cannot be less than the rest mass, the spectrum is therefore identical for all hadrons! This is known as “ m_\perp -scaling”: In a static fireball all hadron spectra follow the same exponential $dN_i/(dy m_\perp dm_\perp) \sim m_\perp^{1/2} e^{-m_\perp/T}$, and the fireball temperature can be immediately extracted from their slope.

Collective flow breaks m_\perp -scaling. This is shown in Fig. 6. The breaking of m_\perp -scaling does

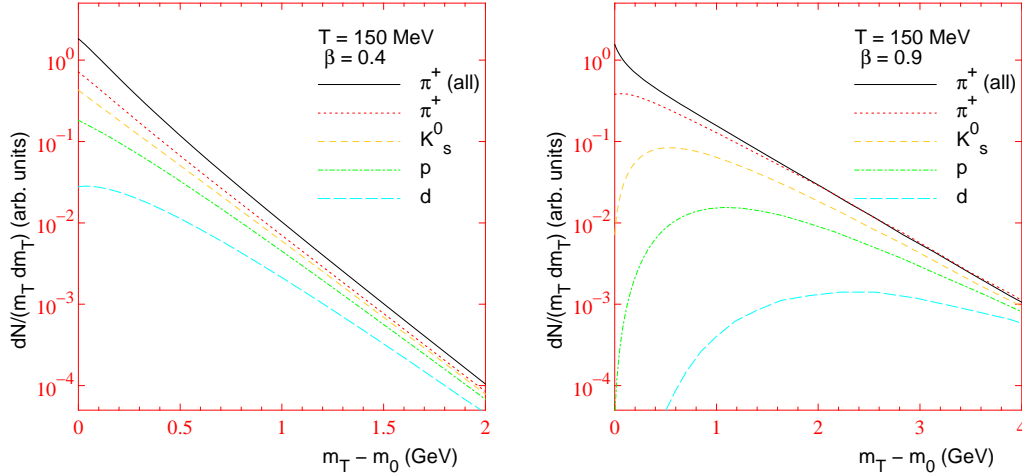


Fig. 6: Flow spectra for various hadrons as a function of $m_\perp - m_0$ where m_0 is their rest mass. The calculation assumes an infinitesimally thin shell of temperature $T = 150$ MeV expanding with $v_\perp = 0.4$ (left) and $v_\perp = 0.9$ (right). The curve labelled “ π^+ (all)” includes pions from resonance decays in addition to the thermally emitted pions.

not occur at large m_\perp where again all spectra approach exponentials with identical slope. However, the inverse slope of these spectra now reflects a blueshifted freezeout temperature: Approximating $p_\perp \approx m_\perp \gg m_i$ and combining the K_0 , K_1 and I_1 , I_0 Bessel functions gives $dN_i/(dy m_\perp dm_\perp) \sim \exp[-\frac{m_\perp}{T}(\cosh \rho - \sinh \rho)] = \exp(-m_\perp/T_{\text{slope}})$ with the inverse slope parameter $T_{\text{slope}} = T\sqrt{\frac{1+v_\perp}{1-v_\perp}}$. This is a standard relativistic blueshift factor reflecting the boost of the thermal radiation *towards* the detector with radial flow velocity v_\perp .

Transverse flow breaks m_\perp -scaling at small transverse momenta $p_\perp \lesssim m_i$ where momenta and velocities can be added non-relativistically. The exact form of the breaking of m_\perp -scaling depends on the density and velocity profiles. It is most extreme for a thin shell expanding with fixed velocity (“blast wave”), shown in Fig. 6, in which case for sufficiently large hadron mass and flow velocity the spectrum develops a “blast wave peak” at nonzero transverse momentum [52]. More realistic calculations take into account the integration over a velocity profile in which the hole at low p_\perp in the blast wave spectrum is filled in by contributions with smaller radial boost velocities from the fireball interior [45]. For a Gaussian density profile combined with a non-relativistic linear transverse velocity profile the integrated spectrum can be calculated analytically [53], and one finds again an exponential m_\perp -spectrum, but this time with inverse slope $T_{i,\text{slope}} = T_f + \frac{1}{2}m_i\langle v_\perp \rangle^2$. We summarize these two important limits:

- Non – relativistic, $p_\perp \ll m_i$: $T_{i,\text{slope}} \approx T_f + \frac{1}{2}m_i\langle v_\perp \rangle^2$ (28)

- Relativistic, $p_\perp \gg m_i$: $T_{\text{slope}} \approx T_f \sqrt{\frac{1+v_\perp}{1-v_\perp}}$ (for all m_i) (29)

The slope systematics for hadrons with different masses in the low- p_\perp region thus allow to separate thermal from collective flow motion. Note that Eq. (28) can never be applied to pions since in the region

$p_{\perp} \ll m_{\pi}$ their slope is affected by Bose statistics and by the contamination from resonance decays (see Fig. 6) neither of which is accounted for by Eq. (28).

4.1.8 Extracting the freeze-out temperature and flow from measured transverse momentum spectra

Equations (28) and (29) show that, as long as $m_i \langle v_{\perp} \rangle \gtrsim 2T_f$, the spectra are steeper at high p_{\perp} and bend over becoming flatter at low p_{\perp} . It is therefore difficult to characterize them by a single slope, especially when the detector measures different hadrons in different p_{\perp} -windows, or when two different experiments measure the same hadron in different p_{\perp} -windows. To extract the flow velocity using Eq. (28)

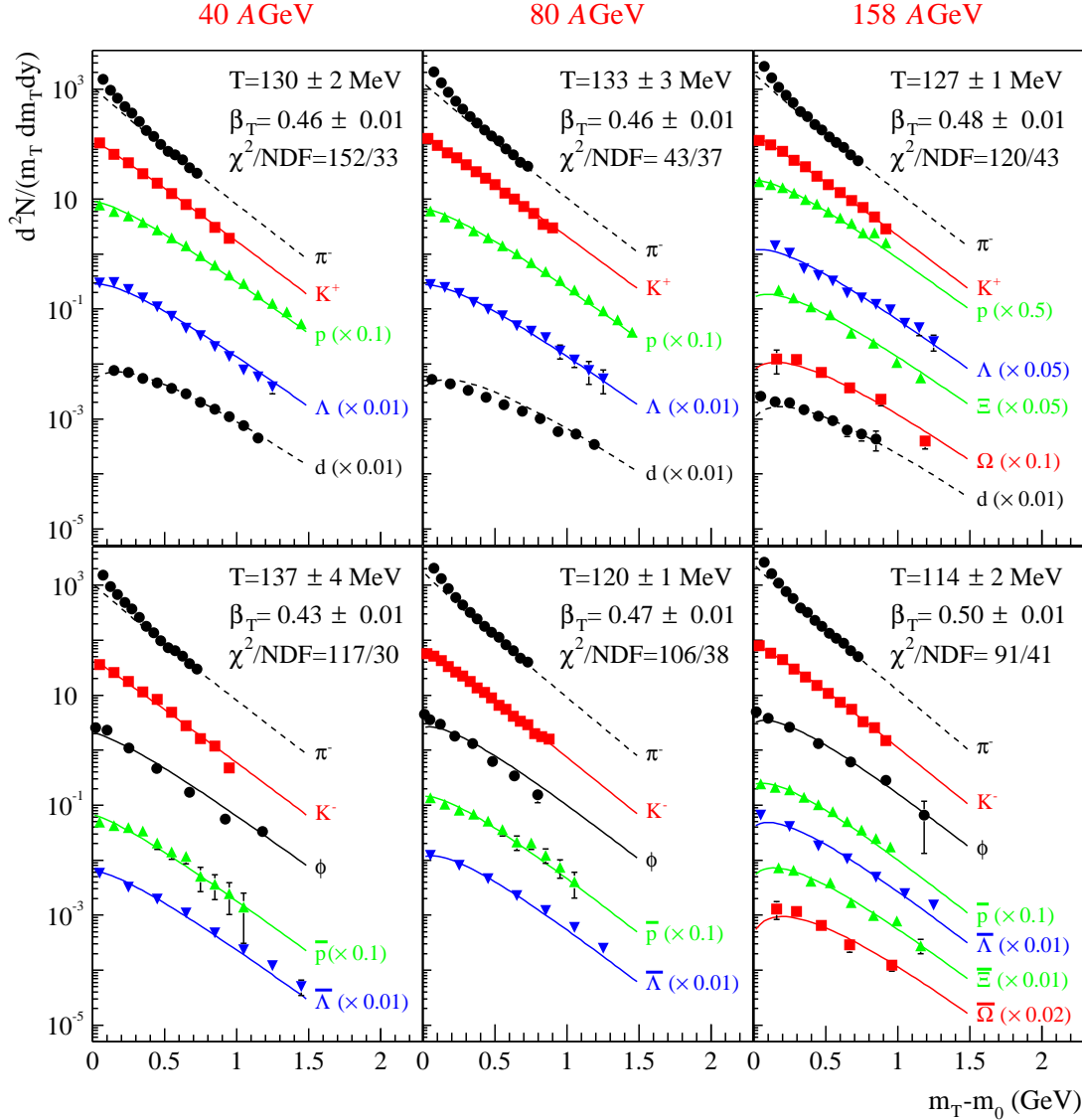


Fig. 7: Positively and negatively charged hadron spectra from central Pb+Pb collisions at 40, 80 and 160 A GeV beam energy at the SPS (left to right), measured by the NA49 Collaboration [54]. Also shown are 2-parameter fits with Eq. (30), assuming a sharp transverse flow velocity β_T (i.e. $w(\rho) = \delta(\rho - \tanh^{-1} \beta_T)$) and constant τ_f . The resulting fit values for T and β_T are given in the figures. Positive and negative hadrons were fitted independently; dashed lines indicate hadrons which were not included in the fit. The dashed pion curve does not include resonance decay contributions and Bose statistics.

requires measuring all hadrons in a common interval of nonrelativistic transverse kinetic energy satisfying $m_{\perp} - m_i \lesssim m_i$. Since such a procedure throws away information outside the common window, it is not very efficient. A much preferred method is to use the entire experimentally available information

on the spectra by performing a simultaneous fit to all hadrons over all m_\perp using Eq. (26). Assuming a constant freeze-out temperature, a common shape for the density profiles $n_i(r_\perp)$, and a specific shape for $\tau_f(r_\perp)$, we can rewrite Eq. (26) as an integral over flow rapidities [46],

$$\frac{dN_i}{dy m_\perp dm_\perp} = N_i \int_0^\infty d\rho w(\rho) \left[m_\perp K_1\left(\frac{m_\perp \cosh \rho}{T}\right) I_0\left(\frac{p_\perp \sinh \rho}{T}\right) - p_\perp \frac{\partial \tau_f}{\partial r_\perp} K_0\left(\frac{m_\perp \cosh \rho}{T}\right) I_1\left(\frac{p_\perp \sinh \rho}{T}\right) \right], \quad (30)$$

with the flow rapidity distribution

$$N_i w(\rho) = \frac{g_i}{\pi^2} r_\perp(\rho) n_i(r_\perp(\rho)) \frac{dr_\perp}{d\rho} \quad (31)$$

where $r_\perp(\rho)$ is the inverse of the velocity profile $\rho(r_\perp)$. We see that for the shape of the spectrum the density and velocity profiles $n_i(r_\perp)$ and $v_\perp(r_\perp)$ have no independent relevance – only the flow rapidity distribution $w(\rho)$ matters. If we fix a reasonable shape for $w(\rho)$ (see [46]), leaving its mean $\langle \rho \rangle$ free, we end up with a 2-parameter fit in terms of the freeze-out temperature $T = T_f$ and average transverse flow velocity $\langle v_\perp \rangle = \tanh^{-1} \langle \rho \rangle$.

Figure 7 shows such a fit to hadronic m_\perp -spectra measured by the NA49 Collaboration [54] in Pb+Pb collisions at the SPS at three different beam energies. Even disregarding the fitted lines the flow-typical hierarchy of slopes in the low- m_\perp region is obvious. The fit was done with a thin-shell model with fixed radial flow velocity. As discussed above this tends to exaggerate the bending of the spectra at low p_\perp , especially for the heavier particles Ξ , Ω and the deuteron. This tendency can be seen in Fig. 7. Otherwise the quality of the fit, its ability to describe all spectra simultaneously, and the consistency of the fit parameters extracted from positively and negatively charged hadrons is impressive.

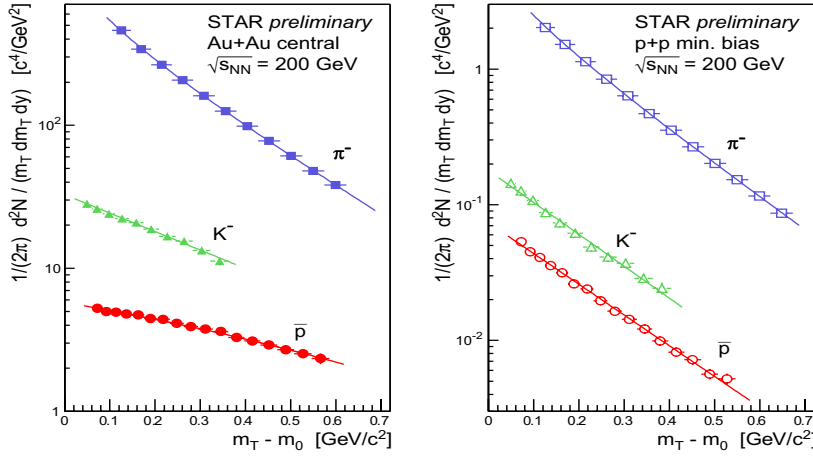


Fig. 8: Pion, kaon and antiproton spectra from 200 A GeV central Au+Au (left) and minimum bias p+p collisions (right), measured by the STAR experiment [55]. Note the similar slopes for kaons and antiprotons in p+p collisions and their dramatically different slopes at low transverse kinetic energy in central Au+Au collisions.

The flattening of the spectra at low transverse kinetic energy $m_\perp - m_0$ by transverse collective flow is even more dramatic at RHIC. Figure 8 shows a direct comparison of the negative pion, kaon and antiproton spectra in central Au+Au and minimum bias proton-proton collisions, at the same center of mass energy. Clearly, in p+p collisions the kaon and antiproton spectra have the same slope, indicating the absence of transverse collective flow. That the pion spectra are steeper than both kaons and antiprotons can be attributed to the contribution of resonance decay pions which accumulate at low transverse momenta. However, the pion spectra in Au+Au are obviously flatter in Au+Au than in p+p, and this is even more true for kaons and antiprotons, with a large difference in slope between those last two. Even without a quantitative fit this is a clear manifestation of strong radial flow.

A two-parameter flow fit on RHIC data from 200 A, GeV Au+Au collisions was performed by J. Burward-Hoy [56], see Fig. 9. Here a box-profile for the transverse density $n_i(r_\perp)$ and a linear transverse

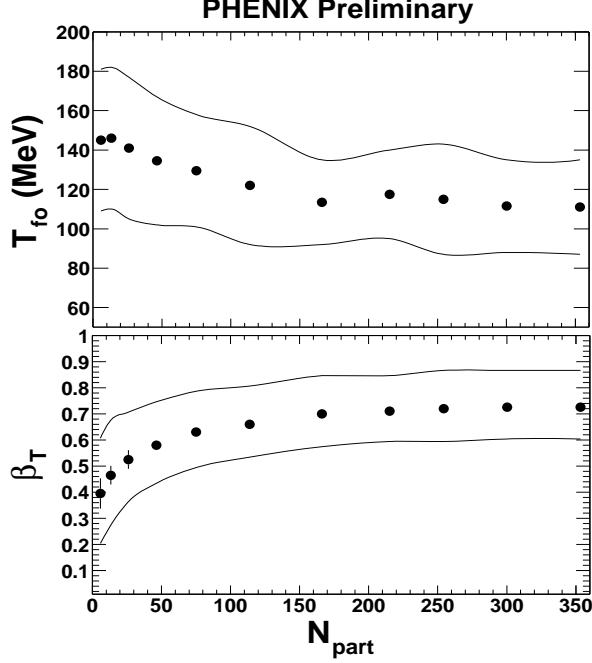


Fig. 9: Kinetic freeze-out temperature T_f and transverse flow velocity β_T at the fireball edge, extracted from a simultaneous fit of a flow spectrum parametrization to π^\pm , K^\pm , p and \bar{p} spectra from 200 A GeV Au+Au collisions over the entire range of collision centralities.[56] More peripheral collisions (small numbers N_{part} of participating nucleons) are seen to decouple earlier, at higher freeze-out temperature and with less transverse flow.

velocity profile were used where the number β_T given in Fig. 9 is the surface velocity (the average transverse velocity is $\langle v_\perp \rangle = \frac{2}{3}\beta_T$). Again in the most central collisions freeze-out temperatures of about 120 MeV and average radial flow velocities $\langle v_\perp \rangle, \simeq 0.45$ are found. One should note, however, that in this case the pions were included in the fit, without correction for resonance decay feeddown. Resonance decay contributions steepen the pion spectrum, biasing the fit towards lower temperatures and/or flow velocities. The bands in the Figure attempt to provide an estimate of the systematic uncertainty associated with details of the model assumptions on the density and velocity profile and of the p_\perp range of the pion spectrum used in the fit [56].

An interesting aspect of Fig. 9 is the centrality dependence of the fit parameters: The fits were performed over a very wide range of collision centralities, and one observes that more peripheral collisions tend to develop less radial flow and freeze out at a higher temperature. This is consistent with the expectation that the collision fireballs in peripheral collisions don't live as long and have less time to build up radial flow. However, even though their average flow is smaller, the *flow gradients* are bigger (due to the smaller size), leading to decoupling at higher particle density and temperature. In pp collisions one expects no or very little collectivity; Fig. 9 indicates that the transition to this limit in the most peripheral Au+Au collisions is very steep, and that already a small number of nucleons participating in the collision generates significant collectivity and sizeable radial flow.

Since the effects of the freeze-out temperature and flow on the spectral slope are strongly anticorrelated [20], flow fits from single-particle spectra tend to produce narrow χ^2 valleys in the T - $\langle v_\perp \rangle$ plane, oriented from the upper left to the lower right. A direct comparison of the spectra from Pb+Pb at the SPS and from Au+Au at RHIC shows that the RHIC spectra are flatter, especially for the heavier hadrons ((anti)protons, (anti)Lambdas, etc.) [46, 57]. So, when fitted with exactly the same procedure, RHIC data give χ^2 valleys which in the T - $\langle v_\perp \rangle$ plane lie to the upper right of those obtained from the SPS data [46, 57]. At the same T_f they produce a somewhat larger flow whereas with the same flow RHIC data yield somewhat higher freeze-out temperatures [46]. In either case the effect is about 15%.

This flow analysis of the single-hadron spectra leads us to our **First Lesson**: When the collision is over and the hadron momentum spectra decouple, the fireball has a “thermal freeze-out temperature” $T_f \simeq 110 - 130$ MeV and is in a state of rapid transverse collective expansion with $\langle v_\perp \rangle \simeq 0.45 - 0.55 c$ (“The Little Bang”). These parameters have a systematic uncertainty $\sim \pm 10\%$ and are strongly anti-

correlated. In the T - $\langle v_\perp \rangle$ plane the χ^2 valleys for the RHIC data are shifted systematically about 15% towards the upper right compared to the SPS data.

4.1.9 Hydrodynamic calculation of radial flow

Of course, a flow fit to the spectra is just a fit, and there is no *a priori* guarantee that the extracted fit parameters make physical sense. In order to assess whether the extracted freeze-out temperatures and radial flow velocities are physically meaningful we must check that they can be the result of reasonable models for the dynamical evolution of the fireball. Is it possible to generate that much collective transverse flow during the short lifetime of the collision zone before everything fizzles?

The natural language for studying flow phenomena is hydrodynamics. The hydrodynamic equations of motion are obtained from the local conservation laws for energy, momentum and baryon number,

$$\partial_\mu T^{\mu\nu}(x) = 0 \quad (\nu = 0, \dots, 3) \quad \text{and} \quad \partial_\mu j_B^\mu(x) = 0, \quad (32)$$

by inserting the *ideal fluid decompositions* for the energy-momentum tensor and baryon number current:

$$T^{\mu\nu}(x) = (e(x) + p(x))u^\mu(x)u^\nu(x) - p(x)g^{\mu\nu}, \quad j_B^\mu(x) = n_B(x)u^\mu(x). \quad (33)$$

These are 5 partial differential equations for 6 fields (p, e, n_B and the 3 independent components of u^μ), and the system must be closed by providing an equation of state $p(e, n_B)$ for the fluid matter. We use an equation of state which mimicks the lattice QCD results from Fig. 2 by matching a hadron resonance gas below T_{cr} to an ideal gas of massless quarks and gluons above T_{cr} . For details I refer to the literature [58, 59]. The numerical solution is considerably simplified by assuming Bjorken scaling flow [41] along the beam direction [60] (see Sec. 4.1.4). The form of these simplified equations can be found e.g. in [58, 59]. They are solved for the transverse flow and hadron spectra near midrapidity where, at sufficiently high collision energies, the assumption of longitudinal boost-invariance should yield a good approximation. To obtain the entire rapidity distribution, on the other hand, requires a solution of the full (3+1)-dimensional set of equations (see, e.g., Refs. [61, 62]) since boost-invariance breaks down near the target and projectile rapidities.

As discussed in Sec. 3.4, the applicability of fluid dynamics requires mean free paths which are short on any relevant macroscopic length scale. It can therefore not be used for the initial pre-equilibrium stage of the collision just after nuclear impact nor for the very last stage when the matter becomes so dilute that particles start to decouple. In addition to an equation of state (see Sec. 2.2), hydrodynamics thus needs *initial conditions* for the time at which it starts to be a good approximation and for the energy density, baryon number density and flow velocity profiles at that time, and a *freeze-out algorithm* which tells us where to stop the hydrodynamic evolution and how to translate the hydrodynamic output (energy and baryon densities and flow at freeze-out) into hadron spectra. For the freeze-out algorithm we use the Cooper-Frye formula discussed in Sec. 4.1.5 with a constant freeze-out temperature. The initial time, the initial entropy (or energy) and baryon density in the fireball, and the freeze-out temperature (or equivalently the decoupling energy density) are treated as parameters to be adjusted to experimental observables. The shape of the initial density profiles is calculated from the overlap geometry of the two nuclei (for details see [63]). For the initial flow we assume a Bjorken scaling profile along the beam direction (see Sec. 4.1.4) and zero initial transverse flow.

We thus need to fix four parameters, $\tau_{\text{eq}}, s_{\text{eq}}, n_{B,\text{eq}}$ and e_{dec} . The ratio of the net baryon density $n_{B,\text{eq}}$ to the entropy density s_{eq} is fixed by the measured proton/pion ratio. By entropy conservation, the final total charged multiplicity dN_{ch}/dy fixes the initial product $(s \cdot \tau)_{\text{eq}}$ [50, 41, 60]. The value of τ_{eq} controls how much transverse flow can be generated until freeze-out. It can thus be determined by trying to fit the final pion and proton spectra simultaneously whose different slopes at low p_\perp are sensitive to the radial flow at freeze-out. The associated freeze-out temperature, also implicit in these spectra, then fixes the decoupling energy density e_{dec} .

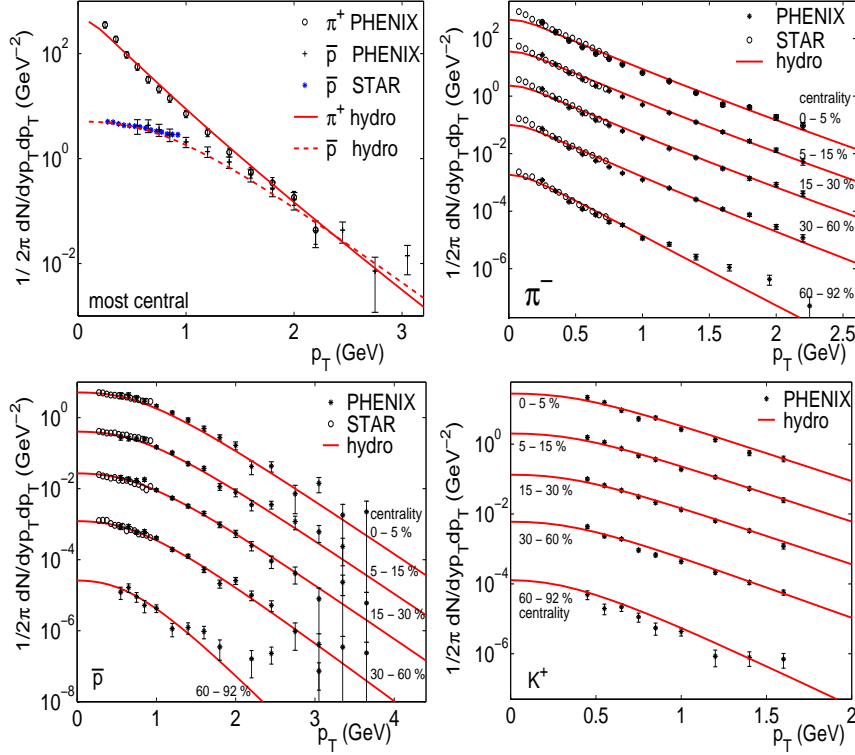


Fig. 10: Identified pion, antiproton and kaon spectra for $\sqrt{s_{NN}} = 130$ GeV from the PHENIX [65, 69] and STAR [66, 67] collaborations in comparison with results from a hydrodynamic calculation [64]. The top left panel shows pion and (anti)-proton spectra from central collisions. Shown in the other panels are spectra of five different centralities: from most central (top) to the most peripheral (bottom). The spectra are successively scaled by a factor 0.1 for clarity.

The top left panel of Fig. 10 shows the hydrodynamic fit [64] to the transverse momentum spectra of positive pions and antiprotons, as measured by the PHENIX and STAR collaborations in central ($b = 0$) Au+Au collisions at $\sqrt{s} = 130$ A GeV [65, 66, 67]. The fit yields an initial central entropy density $s_{eq} = 95 \text{ fm}^{-3}$ at an equilibration time $\tau_{eq} = 0.6$ fm. This corresponds to an initial temperature of $T_{eq} = 340$ MeV and an initial energy density $e = 25 \text{ GeV/fm}^3$ in the fireball center. (Note that these parameters satisfy the “uncertainty relation” $\tau_{eq} \cdot T_{eq} \approx 1$.) Freeze-out was implemented on a hypersurface of constant energy density with $e_{dec} = 0.075 \text{ GeV/fm}^3$. Table 1 summarizes the initial conditions applied in hydrodynamic studies at SPS and RHIC energies (see the recent review [58] for references).

$\sqrt{s_{NN}}$ (GeV)	SPS	RHIC 1	RHIC 2
$s_{eq} (\text{fm}^{-3})$	43	95	110
$T_{eq} (\text{MeV})$	257	340	360
$\tau_{eq} (\text{fm}/c)$	0.8	0.6	0.6

Table 1. Initial conditions for SPS and RHIC energies used to fit the particle spectra from central Pb+Pb or Au+Au collisions. s_{eq} and T_{eq} refer to the maximum values at τ_{eq} in the fireball center.

The fit in the top left panel of Fig. 10 was performed with a chemical equilibrium equation of state. Use of such an equation of state implicitly assumes that even below the hadronization temperature T_{cr} chemical equilibrium among the different hadron species can be maintained all the way down to kinetic freeze-out. With such an equation of state the decoupling energy $e_{dec} = 0.075 \text{ GeV/fm}^3$ translates into a kinetic freeze-out temperature of $T_{dec} \approx 130$ MeV. The data, on the other hand, show [68] that the hadron abundances freeze out at $T_{chem} \approx T_{cr}$, i.e. already when hadrons first coalesce from the expanding quark-gluon soup the inelastic processes which could transform different hadron species into each other are too

slow to keep up with the expansion. The measured \bar{p}/π ratio thus does not agree with the one computed from the chemical equilibrium equation of state at the kinetic freeze-out temperature $T_{\text{dec}} = 130$ MeV, and the latter must be rescaled by hand if one wants to reproduce not only the shape, but also the correct normalization of the measured spectra in Fig. 10.

A better procedure would be to use a chemical non-equilibrium equation of state for the hadronic phase [70, 71, 72] in which for temperatures T below T_{chem} the chemical potentials for each hadronic species are readjusted in such a way that their total abundances (after decay of unstable resonances) are kept constant at the observed values. This approach has recently been applied [73] to newer RHIC data at $\sqrt{s} = 200$ A GeV.

Once the parameters have been fixed in central collisions, spectra at other centralities and for different hadron species can be predicted without introducing additional parameters. The remaining three panels of Fig. 10 show the transverse momentum spectra of pions, kaons and antiprotons in five different centrality bins as observed by the PHENIX [65, 69] and STAR [66, 67] collaborations. For all centrality classes, except the most peripheral one, the hydrodynamic predictions (solid lines) agree pretty well with the data. The kaon spectra are reproduced almost perfectly, but for pions the model consistently underpredicts the data at low p_{\perp} . This has now been understood to be largely an artifact of having employed in these calculations a chemical equilibrium equation of state all the way down to kinetic freeze-out. More recent calculations [73] with a chemical non-equilibrium equation of state show that, as the system cools below the chemical freeze-out point $T_{\text{chem}} \approx T_{\text{cr}}$, a significant positive pion chemical potential builds up, emphasizing the concave curvature of the spectrum from Bose effects and increasing the feeddown corrections from heavier resonances at low p_{\perp} .

Significant discrepancies are also seen at large impact parameters and large transverse momenta $p_{\perp} \gtrsim 2.5$ GeV/c. This is not surprising since high- p_{\perp} particles require more rescatterings to thermalize and escape from the fireball before doing so. This is in particular true in more peripheral collisions where the reaction zone is smaller.

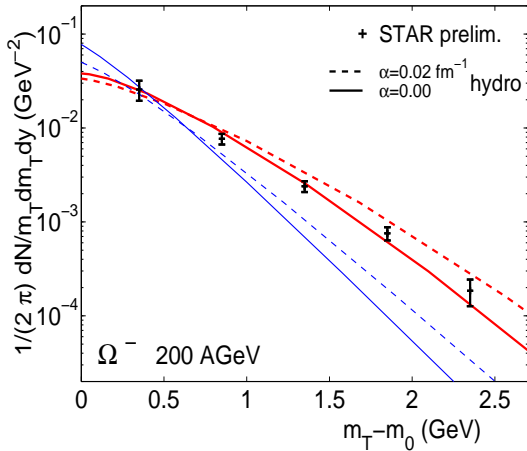


Fig. 11: Transverse mass spectrum of Ω hyperons from central 200 A GeV Au+Au collisions at RHIC [74]. The curves are hydrodynamic calculations [73] with different initial and freeze-out conditions: Solid lines correspond to the default of no initial transverse flow at τ_{eq} , dashed lines assume a small but non-zero radial flow, $v_{\perp} = \tanh(\alpha r_{\perp})$ with $\alpha = 0.02$ fm $^{-1}$, already at τ_{eq} . The lower (thin) set of curves assumes Ω -decoupling at $T_{\text{cr}} = 164$ MeV, the upper (thick) set of curves decouples the Ω together with the pions and protons at $e_{\text{dec}} = 0.075$ GeV/fm 3 . (In the chemical non-equilibrium hadronic equation of state employed here this value of e_{dec} corresponds to a freeze-out temperature $T_{\text{dec}} \approx 100$ MeV – see Ref. [73] for details.)

Figure 11 compares preliminary spectra of Ω hyperons [74] with hydrodynamic predictions [73, 75]. For this comparison the original calculations for 130 A GeV Au+Au collisions [75] were repeated with RHIC2 initial conditions and a chemical non-equilibrium equation of state in the hadronic phase [73]. Following a suggestion that Ω hyperons, being heavy and not having any known strong coupling resonances with pions, should not be able to participate in any increase of the radial flow during the hadronic phase and thus decouple early [76], Fig. 11 shows two solid lines, the steeper one corresponding to decoupling at $e_{\text{dec}} = 0.45$ GeV/fm 3 , i.e. directly after hadronization at T_{cr} , whereas the flatter one assumes decoupling together with pions and other hadrons at $e_{\text{dec}} = 0.075$ GeV/fm 3 . The data clearly favor the flatter curve, suggesting intense rescattering of the Ω 's in the hadronic phase. The microscopic mechanism for this rescattering is still unclear. However, without hadronic rescattering the hydrodynamic

model, in spite of its perfect local thermalization during the early expansion stages, is unable to generate enough transverse flow to flatten the Ω spectra as much as required by the data. Partonic hydrodynamic flow alone can not explain the Ω spectrum. Similar comments apply to the Ω and $\bar{\Omega}$ spectra from Pb+Pb collisions at the SPS shown in Fig. 7.

We close this subsection by concluding that the freeze-out parameters extracted from flow fits to the measured spectra are *dynamically consistent*, i.e. they can be reproduced in hydrodynamic calculations of the fireball evolution using realistic initial conditions. The successful hydrodynamic calculations require fast thermalization at $\tau_{\text{eq}} \lesssim 1 \text{ fm}/c$ and high initial energy density, $e_{\text{eq}} \gtrsim 20 \text{ GeV}/\text{fm}^3$. This conclusion will be solidified by the study of elliptic flow in the next subsection. The hydrodynamically generated strong transverse flow naturally explains the much flatter proton than pion spectra at low p_{\perp} (see Fig. 10). Together with the approximate baryon/antibaryon symmetry at RHIC ($\bar{p}/p \approx 0.7$ in Au+Au collisions) this provides a simple understanding for the initially puzzling observation that in Au+Au collisions at RHIC for $p_{\perp} \gtrsim 2 \text{ GeV}/c$ *antiprotons are as abundant as negative pions* (upper left panel in Fig. 10)! This is completely unexpected from standard string and jet fragmentation phenomenology in pp and e^+e^- collisions where the \bar{p}/π^- ratio never exceeds 10-15%, but a simple (albeit dramatic) consequence of the collective transverse flow in heavy-ion collisions.

4.2 Elliptic flow

4.2.1 Anisotropic flow in non-central collisions

For central collisions ($b=0$) between equal spherical nuclei, radial flow (left panel of Fig. 12) is the only possible type of transverse flow allowed by symmetry. In non-central ($b \neq 0$) collisions between

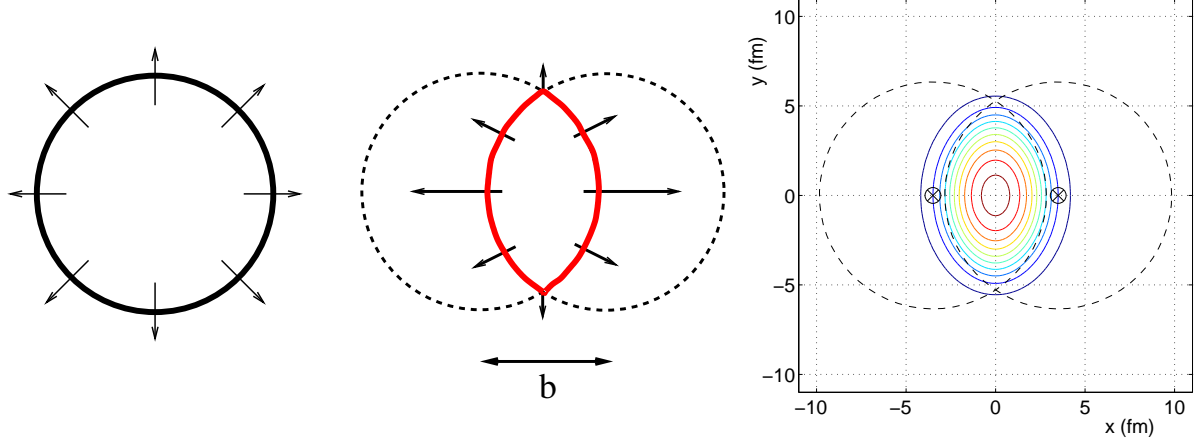


Fig. 12: Left and center panels: Schematic picture of radial and elliptic flow. Right panel: Initial energy density contours in the transverse plane for a Au+Au collision at impact parameter $b = 7 \text{ fm}$. The dashed circles indicate transverse projections of the colliding nuclei.

spherical nuclei (right panels of Fig. 12), or in $b=0$ collisions between suitably aligned deformed nuclei (such as ^{238}U), this azimuthal symmetry is broken and anisotropic transverse flow patterns can develop. The overlap region of the two colliding nuclei is then spatially deformed in the transverse plane, i.e. the *spatial eccentricity* of the reaction zone

$$\varepsilon_x(b) = \frac{\langle y^2 - x^2 \rangle}{\langle y^2 + x^2 \rangle} \quad (34)$$

(where the average is taken with the energy density distribution) is initially non-zero and positive. Rescattering processes among the produced particles transfer this spatial deformation onto momentum space, i.e. the initially locally isotropic transverse momentum distribution of the produced matter begins to become anisotropic. The driving force for this momentum anisotropy is the spatial eccentricity; the

momentum anisotropy can only grow as long as $\varepsilon_x > 0$. As a function of time ε_x decreases, either spontaneously due to free-streaming radial expansion (if no rescattering happens) or somewhat more quickly due to the development of elliptic flow (if rescattering occurs) which makes the system expand faster into the reaction plane than perpendicular to it (see middle panel in Fig. 12). Once the spatial eccentricity has disappeared, the momentum anisotropy saturates [77]. Since this happens quite early in the collision (as we will see shortly), the finally observed momentum anisotropy opens a window onto the early stage of the fireball expansion.

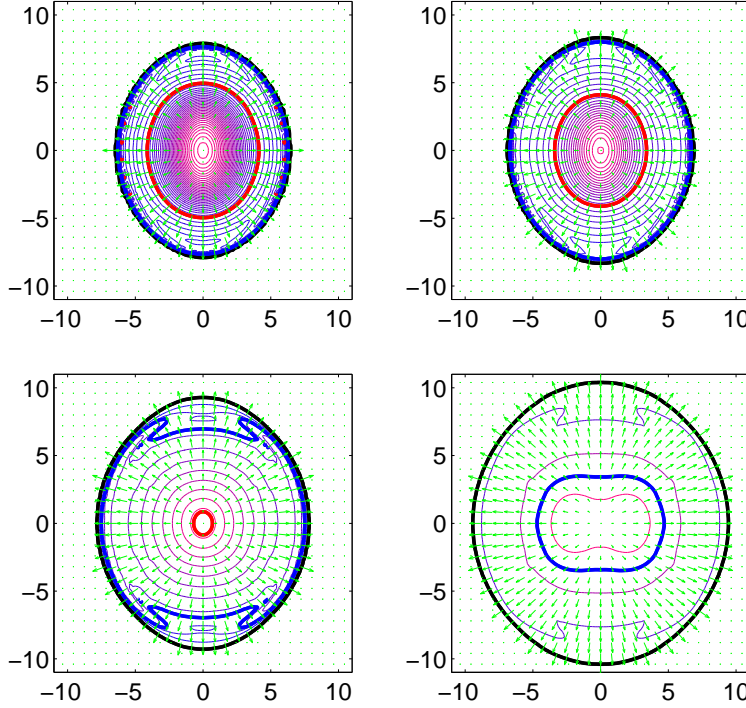


Fig. 13: Snapshots of the energy density contours (lines) and velocity profiles (small arrows) taken at $\tau - \tau_{\text{eq}} = 3.2, 4.0, 5.6$ and 8.0 fm/c after initialization, for Pb+Pb collisions at $b = 7$ fm for an initial central temperature $T_{\text{eq}} = 500$ MeV (from Ref. [59]). The outer thick (black) line indicates the freeze-out surface at e_{dec} , the next thick (blue) line separates the hadron resonance gas from the enclosed mixed phase, and the innermost thick (red) line separates the mixed phase from the quark-gluon plasma in the center. The quark-gluon plasma phase disappears shortly after the third snapshot at $\tau - \tau_{\text{eq}} = 5.6$ fm/c (lower left panel). The horizontal and vertical axes are x and y in fm, respectively (as in Fig. 12).

The mechanism for the creation of elliptic flow is most easily understood in the hydrodynamic limit: After thermalization there is high pressure in the interior of the reaction zone which falls off to zero outside. Obviously the pressure gradient is steeper in the short direction, leading to stronger hydrodynamic acceleration into the reaction plane. This is seen in Fig. 13 where I show hydrodynamically computed energy density contours and flow vector fields for non-central Pb+Pb collisions for 4 different times after the onset of hydrodynamic expansion. One sees that the reaction zone expands faster into the reaction plane and that the spatial eccentricity is almost gone after about 8 fm/c.

Figure 14 shows the time evolution of the spatial eccentricity ε_x and of the momentum anisotropy

$$\varepsilon_p(\tau) = \frac{\int dx dy (T^{xx} - T^{yy})}{\int dx dy (T^{xx} + T^{yy})}. \quad (35)$$

Note that with these sign conventions, the spatial eccentricity is positive for out-of-plane elongation (as is the case initially) whereas the momentum anisotropy is positive if the preferred flow direction is *into* the reaction plane. The calculations were done for Au+Au collisions at impact parameter $b = 7$ fm, for

RHIC initial conditions with a realistic equation of state (EOS Q, solid lines) and for a much higher initial energy density (initial temperature at the fireball center = 2 GeV) with a massless ideal gas equation of state (EOS I, dashed lines), relevant for future experiments at the LHC [78].

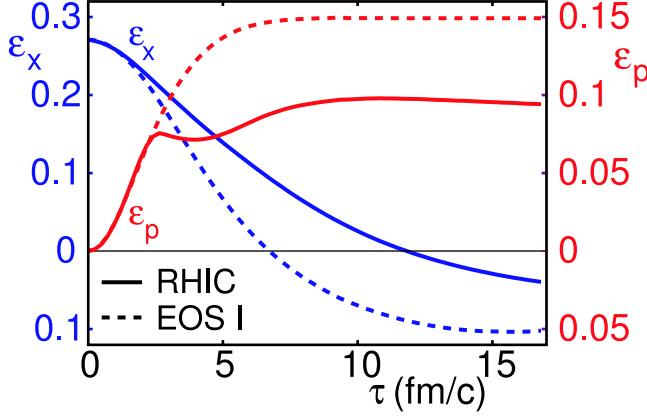


Fig. 14: Time evolution of the spatial eccentricity ε_x and the momentum anisotropy ε_p for Au+Au collisions with $b = 7$ fm at RHIC and at much higher collision energies (from Ref. [78]).

The initial spatial asymmetry at this impact parameter is $\varepsilon_x(\tau_{\text{equ}}) = 0.27$, and clearly $\varepsilon_p(\tau_{\text{equ}}) = 0$ since the fluid is initially at rest in the transverse plane. The spatial eccentricity is seen to disappear before the fireball matter freezes out, in particular for the case with the very high initial temperature (dashed lines) where the source is seen to switch orientation after about 6 fm/c and becomes in-plane-elongated at late times [51]. One also sees that the momentum anisotropy ε_p saturates at about the same time when the spatial eccentricity ε_x vanishes; all of the momentum anisotropy is built up during the first 5 fm/c.

At RHIC the saturation happens even earlier because part of the matter begins to hadronize even before the spatial eccentricity has fully disappeared. Near the phase transition (in particular if as in our case it is modelled as a first order transition) the equation of state becomes very soft, and this inhibits the generation of transverse flow. This also affects the generation of transverse flow *anisotropies* as seen from the solid curves in Figure 14: The rapid initial rise of ε_p suddenly stops as a significant fraction of the fireball matter enters the mixed phase. It then even decreases somewhat as the system expands radially without further acceleration, thereby becoming more isotropic in both coordinate and momentum space. Only after the phase transition is complete and pressure gradients reappear, the system reacts to the remaining spatial eccentricity by a slight further increase of the momentum anisotropy. The softness of the equation of state near the phase transition thus focusses the generation of anisotropic flow to even earlier times, when the system is still entirely partonic and has not even begun to hadronize. At RHIC energies this means that almost all of the finally observed elliptic flow is created during the first 3-4 fm/c of the collision and reflects the hard QGP equation of state of an ideal gas of massless particles ($c_s^2 = \frac{1}{3}$) [59]. Microscopic kinetic studies of the evolution of elliptic flow lead to similar estimates for this time scale [77, 79, 80, 81].

4.2.2 The elliptic flow coefficient v_2

The momentum anisotropy ε_p manifests itself as an azimuthal anisotropy of the measured hadron spectra. One quantifies this anisotropy in terms of the azimuthal Fourier coefficients of the transverse momentum spectrum:

$$\frac{dN_i}{dy p_\perp dp_\perp d\varphi_p}(b) = \frac{1}{2\pi} \frac{dN_i}{dy p_\perp dp_\perp}(b) \left(1 + 2v_2^i(p_\perp, b) \cos(2\varphi_p) + \dots \right). \quad (36)$$

These coefficients depend on the impact parameter b , the transverse momentum p_\perp and the particle species i (through their rest mass m_i). We have suppressed the dependence on rapidity y since the calculation assumes longitudinal boost-invariance and thus makes meaningful statements only near $y = 0$. At midrapidity v_2 is (for collisions between equal nuclei) the lowest nonvanishing Fourier coefficient.

Reflection symmetry with respect to the reaction plane forbids the appearance of sine terms in the expansion. Equation (36) implies that the elliptic flow coefficient can be calculated as

$$v_2^i(p_\perp, b) = \langle \cos(2\varphi_p) \rangle_{p_\perp, b}^i \quad (37)$$

were the average is performed with the transverse momentum spectrum of particle species i at fixed impact parameter and p_\perp . If the average is performed with the p_\perp -integrated spectrum one obtains the “ p_\perp -integrated elliptic flow” $v_2^i(b)$.

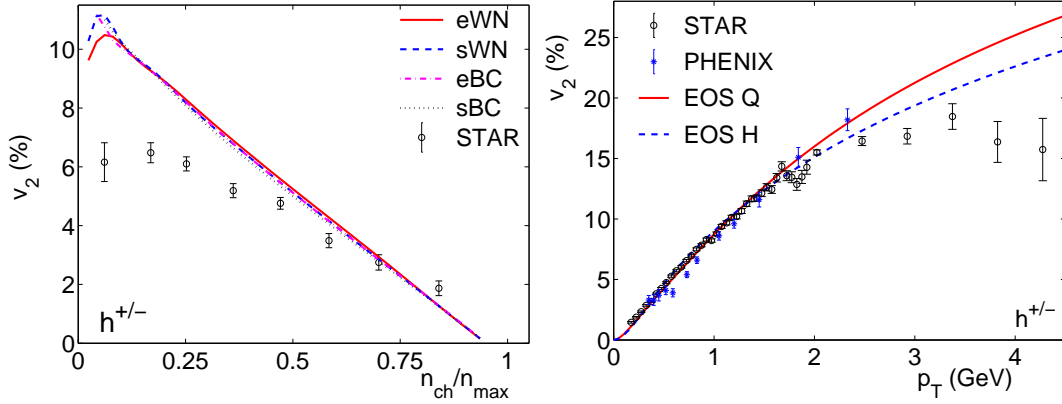


Fig. 15: Elliptic flow of all charged hadrons in 130 A GeV Au+Au collisions at RHIC. Left: p_\perp -integrated elliptic flow vs. collision centrality (measured by the normalized total charged particle multiplicity n_{ch}). Right: differential elliptic flow $v_2(p_\perp)$ for minimum bias collisions (i.e. integrated over all impact parameters). The curves are hydrodynamic calculations for various parametrizations of the initial transverse density profile (for details see [63]). Data are from the STAR [82] and PHENIX [83] Collaborations.

Figure 15 shows a comparison of elliptic flow data for charged hadrons from Au+Au collisions at RHIC with hydrodynamic calculations. The hydrodynamic results are genuine *predictions* since all model parameters have been fixed in central ($b = 0$) collisions where v_2 vanishes. The impact parameter dependence of $v_2(p_\perp)$ then follows from the overlap geometry and its implications for the initial transverse density profile and its spatial eccentricity [63], without additional parameters. The data follow the hydrodynamic predictions up to impact parameters $b \gtrsim 7$ fm ($n_{ch}/n_{max} \lesssim 0.5$ in Fig. 15a) and up to transverse momenta $p_\perp \lesssim 2$ GeV/c (Fig. 15b). For $p_\perp \gtrsim 2$ GeV/c (note that this concerns less than 0.5% of all produced hadrons!) the measured elliptic flow saturates and falls behind the hydrodynamically predicted continuous rise with p_\perp . This indicates a gradual breakdown of local thermal equilibrium for high- p_\perp particles – not a big surprise. Similarly, the elliptic flow in peripheral collisions is also smaller than predicted – again presumably a consequence of incomplete local thermalization in very peripheral collisions where the nuclear overlap zone becomes quite small.

Hydrodynamics predicts a clear mass-ordering of elliptic flow [75]. As the collective radial motion boosts particles to higher average velocities, heavier particles gain more momentum than lighter ones, leading to the previously discussed flattening of their spectra at low transverse kinetic energies. When plotted against p_\perp this effect is further enhanced by a kinematic factor arising from the transformation from m_\perp to p_\perp (see Fig. 10). This flattening reduces the momentum anisotropy coefficient v_2 at low p_\perp [75], and the heavier the particle the more the rise of $v_2(p_\perp)$ is shifted towards larger p_\perp .

This effect, which is a consequence of both the thermal shape of the single-particle spectra at low p_\perp and the superimposed collective radial flow, has been nicely confirmed by the experiments: Figure 16 shows that the data [84, 85] follow the predicted mass ordering out to transverse momenta of about 1.5 GeV/c. For K_s^0 and $\Lambda + \bar{\Lambda}$ very accurate data have recently become available from 200 A GeV Au+Au collisions [86], again in quantitative agreement with hydrodynamic calculations up to $p_\perp \simeq 1.5$ GeV/c for

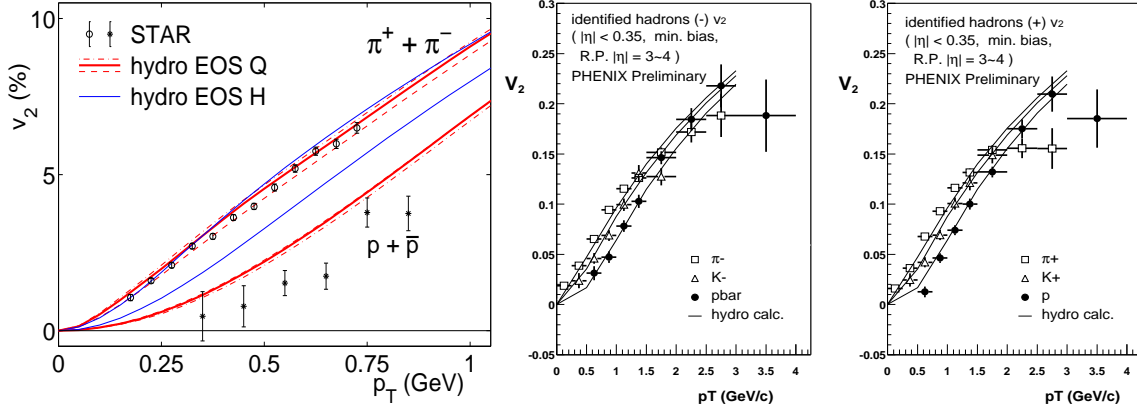


Fig. 16: Differential elliptic flow for identified pions, kaons and (anti)protons from Au+Au collisions at $\sqrt{s_{NN}} = 130$ GeV [84] (left) and at $\sqrt{s_{NN}} = 130$ GeV [85] (right), together with hydrodynamic calculations [64].

kaons and up to $p_{\perp} \simeq 2.5$ GeV/c for $\Lambda + \bar{\Lambda}$. The inversion of the mass-ordering in the data at large p_{\perp} is caused by the mesons whose $v_2(p_{\perp})$ breaks away from the hydrodynamic rise and begins to saturate at $p_{\perp} \gtrsim 1.5$ GeV/c. In contrast, baryons appear to behave hydrodynamically to $p_{\perp} \simeq 2.5$ GeV/c, breaking away from the flow prediction and saturating at significantly larger p_{\perp} than the mesons. This is consistent with the idea that the hadronic elliptic flow really reflects a partonic elliptic flow already established before hadronization, that the latter exhibits a hydrodynamic rise at low p_{\perp} followed by saturation above $p_{\perp} \simeq 750 - 800$ MeV/c, and that these features are transferred to the observed hadrons by quark coalescence, manifesting themselves there at twice resp. three times larger p_{\perp} -values [87].

The comparison of the v_2 data with the hydrodynamic model makes the implicit assumption that all of the measured v_2 is collective, i.e. that non-flow contributions to the angular average $v_2 = \langle \cos(2\varphi_p) \rangle$ can be eliminated. Various experimental cuts [82] ensure that the influence of non-collective 2-particle correlation effects (jet correlations [89], resonance decays, HBT effects) on v_2 are minimized. An alternative method to extract v_2 from higher-order cumulants of the azimuthal particle distribution [90, 91] has recently shown [92] that, in the interesting range $p_{\perp} \lesssim 2$ GeV/c where the emitted hadrons behave hydrodynamically, non-flow corrections do not exceed 15% of the value extracted from the prescription $v_2 = \langle \cos(2\varphi_p) \rangle$. (This may be different at much higher p_{\perp} where v_2 from 2-particle angular correlations seems to approach a p_{\perp} -independent constant value [93] but statistics is not good enough for a 4-particle cumulant analysis which could exclude that at high p_{\perp} an increasing fraction of this v_2 stems from angular 2-particle jet correlations.) Further support of the collective nature of the measured v_2 comes from the observation that the event plane angles reconstructed from v_2 at forward and backward rapidities are, within the statistical error, perfectly correlated. We can therefore assume that at least 85% of the measured v_2 values shown in Figs. 15–17 are due to collective flow.

4.2.3 Rapid thermalization and early pressure – the creation of the Quark-Gluon Plasma

I already mentioned that momentum anisotropies, in particular elliptic flow, can only build as long as the source is spatially deformed. Even if the created particles don't rescatter but simply fly off ballistically with their isotropically distributed initial momenta, the spatial eccentricity decreases as a function of time as [59]

$$\frac{\varepsilon_x(\tau_0 + \Delta\tau)}{\varepsilon_x(\tau_0)} = \left[1 + \frac{(c\Delta\tau)^2}{\langle r^2 \rangle_{\tau_0}} \right]^{-1}, \quad (38)$$

where τ_0 is the time when the particles were created and $\langle r^2 \rangle_{\tau_0}$ is the azimuthally averaged initial transverse radius squared of the reaction zone. So if thermalization is delayed by a time $\Delta\tau$, any elliptic

flow would have to build on a reduced spatial deformation and would come out smaller.

It is also known from microscopic kinetic studies [80, 81] that, for a given collision geometry, i.e. a given initial spatial eccentricity ε_x , the magnitude of the generated elliptic flow is a monotonic function of the mean free path (or the product of density and scattering cross section) in the fireball. This is shown in Fig. 17. Without reinteractions (i.e. for infinite mean free path) no momentum anisotropies develop at

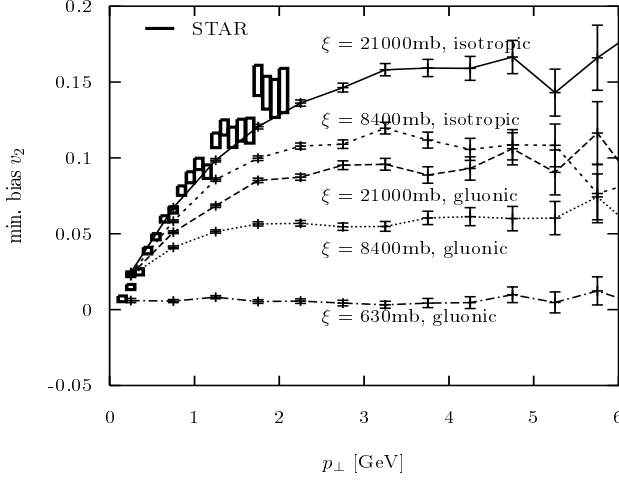


Fig. 17: Impact parameter averaged elliptic flow as a function of transverse momentum. The experimental data points from STAR[82] are compared with parton cascade calculations [81] with varying transport opacities ξ (from [81]).

all [80]; the maximal value for v_2 is reached in the hydrodynamic limit of zero mean free path [88].

This hydrodynamic upper limit for the charged particle elliptic flow was shown to be insensitive to shape details of the initial transverse density distribution [63] and, as long as the shape and normalization of the single particle spectra from central collisions were held fixed by proper retuning of the initial conditions, any sensitivity to details of the QGP equation of state remained below 25% [75]. (Note that this statement refers to the v_2 of all charged particles which are strongly dominated by pions and kaons; Fig. 16a shows that the elliptic flow of heavier particles such as protons, which are more sensitive to radial flow, shows indeed significant dependence on the equation of state, and that the data disfavor, for example, a pure hadron resonance gas over an equation of state with a deconfining phase transition and a hard QGP equation of state above T_{cr} .)

The observation that for $b \lesssim 8$ fm and $p_\perp \lesssim 1.5 - 2$ GeV/c the measured v_2 exhausts at least 85% of the hydrodynamically predicted value thus puts severe constraints on the dynamical evolution and on our global picture of the collision event. It requires early thermalization (such that the spatial eccentricity does not decay before elliptic flow starts to build) and almost complete local equilibrium throughout the crucial first 5 fm/c of the expansion when the momentum anisotropies are generated. The hydrodynamic model calculations for RHIC were done with a thermalization time $\tau_{eq} = 0.6$ fm/c; increasing τ_{eq} beyond 1 fm/c begins to not only seriously degrade the description of the angle-averaged single-particle spectra, but also cuts down v_2 below the experimentally measured level. To obtain the full measured amount of elliptic flow requires almost complete thermalization in less than 1 fm/c.

The sensitivity of v_2 to any kind of deviation from local thermal equilibrium seems to be particularly strong [94, 95]. (Of course, we are talking here about the momentum distribution for particles with average momenta $p_\perp \sim 3T$; no claim for thermalization can be made for particles with much larger than average p_\perp because they are too rare to affect bulk properties such as the pressure and the hydrodynamic expansion.) Turning this observation around and remembering that most of the momentum anisotropy is generated at energy densities well above the critical value for hadronization, the good agreement of the data with ideal fluid dynamics points to a very small viscosity of the quark-gluon plasma. (Note my use of the word *quark-gluon plasma* for the matter in the early expansion stage! What other name could I use for a thermalized system of strongly interacting matter at energy densities $> 10 e_{cr}$?) The QGP does not behave as a weakly interacting quark-gluon gas, as suggested by naive perturbation theory, nor does it

behave like viscous honey, as suggested by the value of the shear viscosity extracted from state-of-the-art resummed thermal field theory at leading order in the strong coupling constant [36]. The fact that the QGP behaves like an ideal fluid implies *strong non-perturbative interactions* in the quark-gluon plasma phase.

So here is our **Second Lesson**: The strong measured elliptic flow at RHIC requires rapid thermalization at $\tau_{\text{eq}} \lesssim 1 \text{ fm}/c$. At this time the average energy density in the thermalized fireball is $e \gtrsim 10 - 15 e_{\text{cr}}$, so thermalization leads into a quark-gluon plasma state. In Au+Au collisions at RHIC this QGP lives for about 5–7 fm/c before hadronizing.

So what about the SPS? Have we made quark-gluon plasma there, too [10]? The energy densities $e \gtrsim 3.5 \text{ GeV}/\text{fm}^3$ were sufficient and, on the 30% accuracy level, hydrodynamics did a good job for the angle-averaged single particle spectra from S+S and Pb+Pb collisions at the SPS, too [20, 96]. However, the measured elliptic flow at the SPS is only about 50% of the value measured at RHIC [97, 98] whereas hydrodynamics predicts it to be even slightly larger than at RHIC [59].¹ So thermalization seems to be less efficient at the SPS than at RHIC. This may not be unreasonable, given the significantly lower (by about a factor 3 [59]) initial density and the rapid conversion of the matter to a less strongly coupled hadron resonance gas before the momentum anisotropy has been able to reach saturation. It would be good to test this with central U+U collisions at the lower end of the collision energy range of RHIC [59]. Such collisions provide similar spatial eccentricities ε_x as semiperipheral Au+Au collisions, but for a fireball which covers a much larger transverse area. This should improve thermalization also at lower energies, making hydrodynamics a better approximation, and help to test our understanding of the dynamical origin of elliptic flow. – I should also mention that at RHIC hydrodynamics fails to reproduce the rapidity-dependence of elliptic flow, predicting a wide rapidity plateau for v_2 [72] whereas the measured elliptic flow rapidly decreases as one moves away from midrapidity [99]. The origin of this discrepancy is not yet clear, but I suspect that it again indicates a breakdown of local equilibrium away from midrapidity [100], for reasons which are related to the analogous breakdown at midrapidity at lower collision energies [101].

5 TWO-PARTICLE BOSE-EINSTEIN CORRELATIONS AND HBT INTERFEROMETRY

Single-particle momentum spectra, including their anisotropies, provide no direct information on the space-time structure of the source. It is therefore in principle possible to describe these spectra with models that have the same momentum structure but completely different freeze-out distributions in space and time. Two-particle correlations, on the other hand, depend on the average separation of the particles at decoupling and therefore provide valuable spatial and temporal information. This is most easily seen for correlations generated by final state Coulomb interactions between charged hadrons which influence their distribution of *relative* momenta depending on how close they were at time of emission. The measured relative momentum distribution of particle pairs thus allows to constrain their average space-time distance at decoupling. Conceptually more involved, but theoretically easier to analyze are two-particle momentum correlations between pairs of identical particles (“Bose-Einstein correlations” in the case of identical bosons) caused by quantum statistical (wave function symmetrization) effects. Again, these affect the relative momentum distribution at low relative momenta, and the relative momentum range of these quantum statistical correlations yields information about the average space-time separation of the emission points of the two particles, and thereby also about the overall size and emission duration of the source. There exist a number recent reviews of these methods to which I refer the reader for more details [102, 103, 104, 105].

For pairs of identical bosons (e.g. pions), this technique is known as Hanbury Brown-Twiss (HBT) interferometry [106]. The basic principle, as applied in particle and nuclear physics, is illustrated in

¹At the SPS most of the elliptic flow is generated in the hadronic phase, and the softening effects of the phase transition on the development of flow are not as important as at RHIC [59].

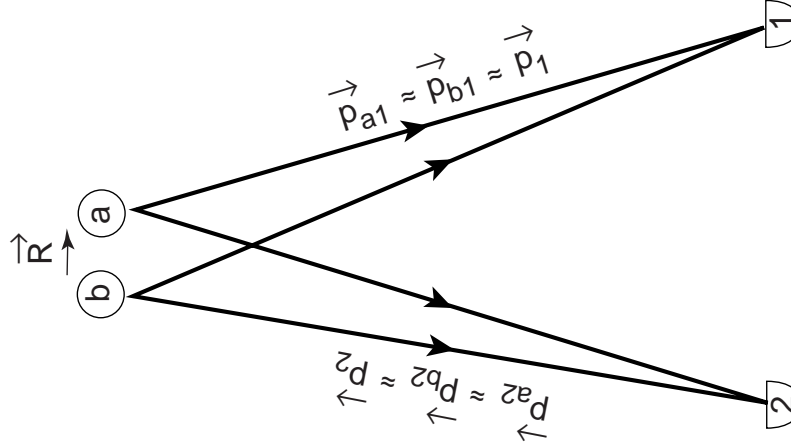


Fig. 18: The principle of two-particle interferometry: a pair of indistinguishable particles is emitted from points a and b and detected by detectors 1 and 2 which measure their momenta \mathbf{p}_1 and \mathbf{p}_2 . The total pair yield is obtained by integrating over all possible positions (a, b) in the source. The measurement is performed as a function of the average momentum $\mathbf{K} = (\mathbf{p}_1 + \mathbf{p}_2)/2$ of the pair and its relative momentum $\mathbf{q} = \mathbf{p}_1 - \mathbf{p}_2$. The \mathbf{q} -dependence yields information about the average separation $\langle R^2 \rangle^{1/2}$ of the emitters a and b which contribute pairs of given pair momentum \mathbf{K} .

Figure 18. I will now shortly outline its theoretical treatment, referring to the literature [102, 103, 104, 105] for more details.

5.1 Single-particle spectra and two-particle correlations

The covariant single- and two-particle distributions are defined by

$$P_1(\mathbf{p}) = E \frac{dN}{d^3p} = E \langle \hat{a}_{\mathbf{p}}^+ \hat{a}_{\mathbf{p}} \rangle, \quad (39)$$

$$P_2(\mathbf{p}_1, \mathbf{p}_2) = E_1 E_2 \frac{dN}{d^3p_1 d^3p_2} = E_1 E_2 \langle \hat{a}_{\mathbf{p}_1}^+ \hat{a}_{\mathbf{p}_2}^+ \hat{a}_{\mathbf{p}_2} \hat{a}_{\mathbf{p}_1} \rangle, \quad (40)$$

where $\hat{a}_{\mathbf{p}}^+$ ($\hat{a}_{\mathbf{p}}$) creates (destroys) a particle with momentum \mathbf{p} . The angular brackets denote an ensemble average $\langle \hat{O} \rangle = \text{tr}(\hat{\rho} \hat{O})$ where $\hat{\rho}$ is the density operator associated with the ensemble. (When talking about an ensemble we may think of either a single large, thermalized source, or a large number of similar, but not necessarily thermalized collision events.) The single-particle spectrum is normalized to the average number of particles, $\langle N \rangle$, per collision,

$$\int \frac{d^3p}{E} P_1(\mathbf{p}) = \langle N \rangle, \quad (41)$$

while the two-particle distribution is normalized to the number of particles in pairs, $\langle N(N-1) \rangle$, per event:

$$\int \frac{d^3p_1}{E_1} \frac{d^3p_2}{E_2} P_2(\mathbf{p}_1, \mathbf{p}_2) = \langle N(N-1) \rangle. \quad (42)$$

The two-particle correlation function is defined as

$$C(\mathbf{p}_1, \mathbf{p}_2) = \frac{P_2(\mathbf{p}_1, \mathbf{p}_2)}{P_1(\mathbf{p}_1)P_1(\mathbf{p}_2)}. \quad (43)$$

If the two particles are emitted independently and final state interactions are neglected one can prove a generalized Wick theorem [107, 108]

$$C(\mathbf{p}_1, \mathbf{p}_2) = 1 \pm \frac{|\langle \hat{a}_{\mathbf{p}_1}^+ \hat{a}_{\mathbf{p}_2} \rangle|^2}{\langle \hat{a}_{\mathbf{p}_1}^+ \hat{a}_{\mathbf{p}_1} \rangle \langle \hat{a}_{\mathbf{p}_2}^+ \hat{a}_{\mathbf{p}_2} \rangle}. \quad (44)$$

This assumption is often called “chaoticity assumption”, having in mind a completely chaotic (uncorrelated) emitter, in contrast to processes where the phases of the wave functions of the two emitted particles are to some extent correlated with each other. The degree of “chaoticity” or “phase correlation” in the source can be studied by comparing three-particle correlations with two-particle ones [109]. This was recently done by the STAR Collaboration [110] who established that in central Au+Au collisions at $\sqrt{s_{\text{NN}}} = 130$ GeV the pion emitting source is indeed completely chaotic.

From now on I will assume that the emitted particles are bosons, e.g. pions, and use the + sign in Eq. (44). We next discuss the numerator of the Bose-Einstein correlation term, $|\langle \hat{a}_{\mathbf{p}_1}^+ \hat{a}_{\mathbf{p}_2} \rangle|^2$.

5.2 Source Wigner function and spectra

As reviewed in Refs. [103, 107, 108], the pion emitting source can be described in terms of classical currents $J(x)$ which act as classical sources of freely propagating pions. These currents represent a parametrization of the last collision from which the free outgoing pion emerges. Using this language in one form or another [103, 107, 108], one can express the “exchange amplitude” $\langle \hat{a}_{\mathbf{p}_1}^+ \hat{a}_{\mathbf{p}_2} \rangle$ as the Fourier transform of the single-particle Wigner density $S(x, K)$ which is the quantum mechanical analogue of the classical phase-space density at pion freeze-out, describing the probability of emitting a pion with momentum K from space-time point x :

$$\langle \hat{a}_{\mathbf{p}_1}^+ \hat{a}_{\mathbf{p}_2} \rangle = \int d^4x S(x, K) e^{iq \cdot x}. \quad (45)$$

$S(x, K)$ is also called “emission function”. $K = \frac{1}{2}(E_1 + E_2, \mathbf{p}_1 + \mathbf{p}_2)$ is the average momentum of the pair while $q = (E_1 - E_2, \mathbf{p}_1 - \mathbf{p}_2)$ is the relative momentum between the two pions. Since the pion momenta $\mathbf{p}_1, \mathbf{p}_2$ are on-shell, $p_i^0 = E_i = (m^2 + \mathbf{p}_i^2)^{1/2}$, the 4-momenta q and K are in general off-shell. They satisfy the orthogonality relation (“on-shell constraint”)

$$q \cdot K = 0 \implies q^0 = \beta \cdot \mathbf{q} \quad \text{with} \quad \beta = \frac{\mathbf{K}}{K^0} \approx \frac{\mathbf{K}}{E_K}. \quad (46)$$

β is the velocity of the pair; the last, so-called “on-shell” approximation holds for small relative momenta \mathbf{q} which is where the correlation term is non-zero:

$$K^0 = E_K \left(1 + \frac{\mathbf{q}^2}{8E_K^2} + \mathcal{O}\left(\frac{\mathbf{q}^4}{E_K^4}\right) \right) \approx E_K. \quad (47)$$

Since the relevant range of q is given by the inverse size of the source (more properly: the inverse size of the regions of homogeneity in the source – see below), the validity of this approximation is ensured in practice as long as the Compton wavelength of the particles is small compared to this “source size”. For the case of pion, kaon, or proton interferometry for heavy-ion collisions this is true automatically due to the rest mass of the particles: even for pions at rest, the Compton wavelength of 1.4 fm is comfortably smaller than any typical nuclear source size. This is of enormous practical importance because it allows you essentially to replace the source Wigner density by a classical phase-space distribution function for on-shell particles. This provides a necessary theoretical foundation for the calculation of HBT correlations from classical hydrodynamic or kinetic (e.g. cascade) simulations of the collision.

With the definition (45) we can express the single-particle spectra (39) and correlation function (44) through the emission function $S(x, K)$:

$$E_p \frac{dN}{d^3p} = \int d^4x S(x, p), \quad (48)$$

$$\begin{aligned} C(\mathbf{q}, \mathbf{K}) &= 1 + \frac{(P_1(\mathbf{K}))^2}{P_1(\mathbf{K} + \frac{1}{2}\mathbf{q})P_1(\mathbf{K} - \frac{1}{2}\mathbf{q})} \left| \frac{\int d^4x e^{iq \cdot x} S(x, K)}{\int d^4x S(x, K)} \right|^2 \\ &\approx 1 + \left| \frac{\int d^4x e^{iq \cdot x} S(x, K)}{\int d^4x S(x, K)} \right|^2 \equiv 1 + \left| \langle e^{iq \cdot x} \rangle \right|^2. \end{aligned} \quad (49)$$

The last line uses the “smoothness approximation” $P_1(\mathbf{K} + \frac{1}{2}\mathbf{q})P_1(\mathbf{K} - \frac{1}{2}\mathbf{q}) \approx |P_1(\mathbf{K})|^2$ which can be justified for sufficiently large sources; it is not really necessary because the single-particle spectra are measured and the ratio $|P_1(\mathbf{K})|^2 / P_1(\mathbf{K} + \frac{1}{2}\mathbf{q})P_1(\mathbf{K} - \frac{1}{2}\mathbf{q})$ can thus be divided out from the correlator $C(\mathbf{q}, \mathbf{K}) - 1$ before analyzing it theoretically, but we use it here for simplicity.

The last equality in Eq. (49) introduces the notation $\langle f(x) \rangle$ for the average of a space-time observable $f(x)$ with the emission function $S(x, K)$. Note that, due to the K -dependence of the emission function, this average depends on the pair momentum K .

The fundamental relations (48) and (49) show that *both the single-particle spectrum and the two-particle correlation function can be expressed as simple integrals over the emission function*. Whereas the single-particle momentum spectrum (48) integrates over the spatial structure of the emission function and thus provides no spatial information about the source, Eq. (49) shows that the \mathbf{q} -dependence of the correlation function $C(\mathbf{q}, \mathbf{K})$ provides access to the space-time structure of the source. However, it depends only on the modulus square of the spatial Fourier transform of the source, so the phase information is missing, and furthermore, due to the “on-shell constraint” (46), not all four components of q can be varied independently. The Fourier transform in Eq. (49) thus mixes space and time in a particular way, and the emission function $S(x, K)$ cannot be fully reconstructed from the measured correlation function $C(\mathbf{q}, \mathbf{K})$ without taking recourse to model assumptions about the source. Still, as I will now show, the correlator $C(\mathbf{q}, \mathbf{K})$ provides very important constraints for any dynamical model for the heavy-ion collision.

5.3 HBT radii and source sizes

The most interesting feature of the two-particle correlation function is its half-width as a function of q . Actually, since the relative momentum $\mathbf{q} = \mathbf{p}_1 - \mathbf{p}_2$ has three Cartesian components, the fall-off of the correlator for increasing q is not described by a single half-width, but rather by a (symmetric) 3×3 tensor. Through the Fourier transform in Eq. (49), these half-widths of the correlator (at a given pair momentum K) can be related to the widths of the emission function $S(x, K)$ in space and time (at the same K). This relation becomes exact if particle emission is not complicated by processes involving multiple time scales. Multiple time scales, with corresponding dynamically induced multiple length scales, are an issue in pion emission from heavy-ion collisions: a large fraction of the observed pions is not emitted from the source directly, but appears later from the decay of unstable resonances which were originally emitted directly from the source but then travelled a certain distance without interactions before decaying. Resonance decay effects on the HBT correlation function have been extensively discussed in the literature (see e.g. [111, 112]). The results can be shortly summarized: Most resonances are so short-lived that they don’t travel far before decaying, leading to a pion emission function of almost the same size and shape as for directly emitted pions. Some resonances are very long-lived and decay far outside the original source; the corresponding temporal and spatial tails in the emission function affect the correlator at such small values of q that they can not be experimentally resolved. They effectively reduce the visible Bose-Einstein correlation strength and can be absorbed by reducing the second term in Eq. (49) by a \mathbf{K} -dependent “intercept parameter” $\lambda(\mathbf{K})$: $C(\mathbf{q}, \mathbf{K}) = 1 + \lambda(\mathbf{K})|\langle e^{iq \cdot x} \rangle_{\text{dir}}|^2(\mathbf{K})$ where $\langle \dots \rangle_{\text{dir}}$ denotes the average with the emission function for (almost) directly emitted pions. The only resonance that can neither be classified as short-lived nor as long-lived in this sense is the ω meson with its lifetime of about 20 fm/c. I will assume here that its abundance is small enough to be negligible (this depends on the freeze-out temperature), but this is mostly for didactical purposes and needs to be reassessed in the actual comparison between theory and data.

With these assumptions the “direct” emission function can be fully characterized by its (K -dependent) “widths”

$$S_{\mu\nu}(\mathbf{K}) = [\langle x_\mu x_\nu \rangle_{\text{dir}} - \langle x_\mu \rangle_{\text{dir}} \langle x_\nu \rangle_{\text{dir}}](\mathbf{K}) \equiv \langle \tilde{x}_\mu \tilde{x}_\nu \rangle_{\text{dir}} \quad (50)$$

which describe the widths of the effective emission region inside the source (“homogeneity region”)

which effectively contributes to the emission of particles with momentum \mathbf{K} . Note that for an expanding source these effective emission regions do not coincide with the entire source: As illustrated in Fig. 19, pions whose momentum \mathbf{K} is large and points in the positive x direction will predominantly originate from the elliptic region near the right edge of the figure, since this region anyway moves collectively in the $+x$ direction. On the other hand, the elliptic region near the top of the figure moves in the $+y$ direction and thus mostly contributes pions with (large) positive y -momentum K_y . Eq. (49) shows that the correlation function $C(\mathbf{q}, \mathbf{K})$ of pairs with pair momentum \mathbf{K} probes only these effective emission regions for particles with fixed \mathbf{K} , not the entire source. Only for static fireball, where each volume element radiates the same momentum spectrum, does the HBT correlation function measure the entire source. (The notation x_{side} and x_{out} used in Fig. 18 will be explained below.)

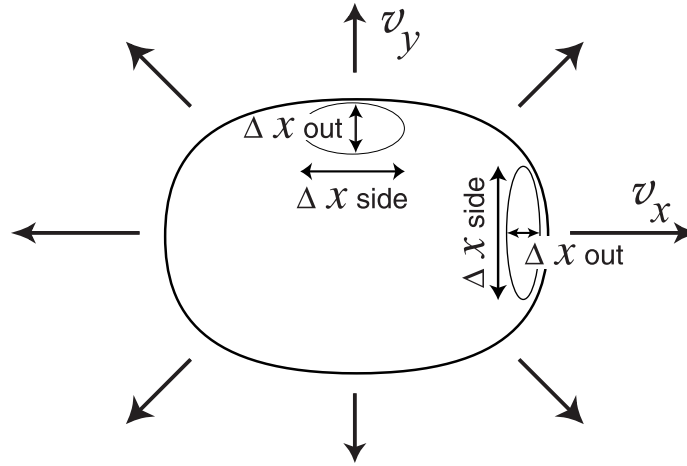


Fig. 19: Illustration of the concept of homogeneity regions in an expanding source (see text).

If, as assumed, the emission function $S(x, K)$ can be fully characterized by its “spatial correlation tensor” $S_{\mu\nu}(\mathbf{K})$ (50) which describes the size and shape of the effective emission regions for particles of momentum \mathbf{K} , we can make the following Gaussian ansatz for $S(x, K)$:

$$S_{\text{dir}}(x, K) \sim e^{-\frac{1}{2}\tilde{x}^\mu(\mathbf{K})(S^{-1})_{\mu\nu}(\mathbf{K})\tilde{x}^\nu(\mathbf{K})}. \quad (51)$$

The normalization is fixed by the single-particle spectrum [103] but drops out from the correlation function. Note the dependence only on the distance $\tilde{x}_\mu(\mathbf{K}) = x_\mu - \langle x_\mu \rangle(\mathbf{K})$ to the point of maximum emissivity at momentum \mathbf{K} – the latter itself can not be measured, i.e. the absolute position of the regions of homogeneity is experimentally inaccessible. Reconstructing the entire source as a sum of effective emission regions for fixed \mathbf{K} is therefore always a model-dependent theoretical enterprise.

The Fourier transform of the above Gaussian parametrization is easily evaluated. Eliminating q^0 with the on-shell constraint (46) and introducing the intercept parameter $\lambda(\mathbf{K})$ as described above to account for the unresolvable tail in the emission function from long-lived resonances gives for the correlation function the Gaussian form

$$C(\mathbf{q}, \mathbf{K}) = 1 + \lambda(\mathbf{K}) \exp \left[- \sum_{i,j=x,y,z} q_i q_j R_{ij}^2(\mathbf{K}) \right], \quad (52)$$

with

$$R_{ij} = S_{ij} - \beta_i S_{it} - \beta_j S_{jt} + \beta_i \beta_j S_{tt}, \quad i, j = x, y, z. \quad (53)$$

The $R_{ij}(\mathbf{K})$ are called ‘‘HBT radius parameters’’; note that the off-diagonal terms with $i \neq j$ need not be positive. The last equation shows explicitly the mixing between spatial and temporal source information in the experimentally measured HBT radius parameters, caused by the on-shell constraint (46).

Note that this mixing involves the components of the pair velocity β ; it can be minimized by rotating the Cartesian coordinate system (x, y, z) such that \mathbf{K} and β point in $+x'$ direction [113]. In relativistic heavy-ion collisions it is, however, advantageous to keep the z -axis aligned with the beam direction, and therefore one rotates only the transverse (x, y) axes such that the transverse pair momentum \mathbf{K}_\perp points in x' direction. This eliminates the y' components of \mathbf{K}_\perp and β . Traditionally [113], the rotated x' axis is called the ‘‘outward’’ direction (denoted as x_{out} or x_o), the y' axis is called the ‘‘sideward’’ direction (x_{side} or x_s), while the beam direction z is called ‘‘longitudinal’’ (denoted by x_{long} or x_l). In this frame $\beta = (\beta_\perp, 0, \beta_L)$ and $\mathbf{K} = (K_\perp, 0, K_L)$. Note, however, that in non-central heavy-ion collisions the direction of the impact parameter \mathbf{b} defines a distinguished direction in the transverse plane, and that therefore even in the out-side-long system the HBT radius parameters $R_{ij}(\mathbf{K})$ still depend on both magnitude and direction of \mathbf{K}_\perp .

5.4 Central ($b=0$) heavy-ion collisions

5.4.1 Formalism

In central collisions between spherical nuclei, the entire source is azimuthally symmetric around the beam axis. After fixing the transverse coordinate system such that the ‘‘out’’-axis points in the emission direction \mathbf{K}_\perp of the pair, the HBT radii R_{ij} can only depend on the magnitude, but not the direction of \mathbf{K}_\perp . Furthermore, the source is clearly symmetric under reflections with respect to the plane defined by the beam direction and \mathbf{K}_\perp , so all components of the spatial correlation tensor $S_{\mu\nu} = \langle \tilde{x}_\mu \tilde{x}_\nu \rangle$ which are linear in \tilde{x}_{side} must vanish. As a result, only *six* nonvanishing components of $S_{\mu\nu}(K_\perp, Y)$ survive. (I here introduce the pair rapidity $Y = \tanh^{-1} \beta_L$ instead of the longitudinal pair momentum K_L .) On the other hand, the same reflection symmetry also eliminates terms from the exponent in Eq. (52) that are linear in $q_s = q_{\text{side}}$ such that only *four* HBT radius parameters are experimentally accessible:

$$C(\mathbf{q}, \mathbf{K}) = 1 + \lambda(\mathbf{K}) \exp \left[-q_s^2 R_s^2 - q_o^2 R_o^2 - q_l^2 R_l^2 - 2q_o q_l R_{ol}^2 \right]. \quad (54)$$

The HBT radii are again functions of two variables only, $R_{ij}(K_\perp, Y)$. Still, there are two more functions $S_{\mu\nu}(K_\perp, Y)$ needed to fully characterize the source than can be measured, due to the on-shell constraint.

In symmetric $A + A$ collisions at midrapidity $Y = 0$, things simplify further: the cross-term R_{ol}^2 vanishes [114], leaving only three functions $R_s(K_\perp)$, $R_o(K_\perp)$, and $R_l(K_\perp)$ to be determined. They are related to the source widths $S_{\mu\nu} = \langle \tilde{x}_\mu \tilde{x}_\nu \rangle$ as follows:

$$R_s^2 = \langle \tilde{x}_s^2 \rangle, \quad (55)$$

$$R_o^2 = \langle \tilde{x}_o^2 \rangle - 2\beta_\perp \langle \tilde{x}_o \tilde{t} \rangle + \beta_\perp^2 \langle \tilde{t}^2 \rangle, \quad (56)$$

$$R_l^2 = \langle \tilde{z}^2 \rangle, \quad (57)$$

where I used that $\beta_L = 0$ at $Y = 0$. I will concentrate on this simple limit since RHIC HBT data have so far only been obtained near $Y = 0$.

The HBT radii (55-57) depend on K_\perp both *explicitly* (through the β_\perp factors in (56)) and *implicitly* (since $\langle \dots \rangle$ denotes an average with the K -dependent emission function). If \mathbf{K}_\perp is the only vector in the problem, there is no distinction between the outward and sideward directions in the limit $K_\perp \rightarrow 0$, so R_o and R_s must be equal to each other in that limit:

$$\lim_{K_\perp \rightarrow 0} (R_o^2 - R_s^2) = \lim_{K_\perp \rightarrow 0} (\langle \tilde{x}_o^2 \rangle - \langle \tilde{x}_s^2 \rangle) = 0. \quad (58)$$

This theorem is not valid for non-central collisions, where the impact parameter \mathbf{b} introduces a preferred direction, and it may also break down for ‘‘opaque’’ (surface emitting) sources where, at least in principle, the outward normal vector can play a similar role [115, 116].

The geometric contributions $\langle \hat{x}_s^2 \rangle$, $\langle \hat{x}_o^2 \rangle$, and $\langle \hat{z}^2 \rangle$ are controlled by an interplay between thermal motion and collective expansion: stronger expansion, resulting in larger flow velocity gradients, tends to reduce these variances whereas higher freeze-out temperatures, resulting in broader momentum spectra, tend to increase the size of the homogeneity regions. This size increase due to thermal smearing is easily understood by considering the limit $T \rightarrow 0$: in this limit particles have no thermal motion, and particles of momentum \mathbf{K} can therefore only come from individual points in the source whose collective flow velocity agrees exactly with the pair velocity β . The corresponding homogeneity regions are pointlike, i.e. have zero size. Thermal particle motion can smear out the collective flow velocity gradients such that particles of given \mathbf{K} can now come from a larger homogeneity region. As $T \rightarrow \infty$, the homogeneity regions approach the size of the entire fireball, irrespective of its dynamical state.

Making these features explicit requires a parametrization of the emission function, for example the extensively studied model function [102, 103, 114, 117]

$$S(x, K) = \frac{M_\perp \cosh(\eta - Y)}{8\pi^4 \Delta\tau} \exp \left[-\frac{K \cdot u(x)}{T(x)} - \frac{(\tau - \tau_0)^2}{2(\Delta\tau)^2} - \frac{r^2}{2R^2} - \frac{(\eta - \eta_0)^2}{2(\Delta\eta)^2} \right]. \quad (59)$$

Here the transverse radius $r^2 = x^2 + y^2$, the spacetime rapidity $\eta = \frac{1}{2} \ln[(t+z)/(t-z)]$, and the longitudinal proper time $\tau = \sqrt{t^2 - z^2}$ parametrize the spacetime coordinates x^μ , with measure $d^4x = \tau d\tau d\eta r dr d\varphi$. $Y = \frac{1}{2} \ln[(E_K + K_L)/(E_K - K_L)]$ and $M_\perp = \sqrt{m^2 + K_\perp^2}$ parametrize the longitudinal and transverse components of the pair momentum \mathbf{K} . $\sqrt{2}R$ is the transverse geometric (Gaussian) radius of the source, τ_0 its average freeze-out proper time, $\Delta\tau$ the mean proper time duration of particle emission, and $\Delta\eta$ parametrizes the finite longitudinal extension of the source. $T(x)$ is the freeze-out temperature; if you don't like the idea of invoking thermal equilibrium during the decoupling stage, you can think of T as a parameter that describes the random distribution of the particle momenta at each space-time point around their average value. The latter is parametrized by a collective flow velocity $u^\mu(x)$ in the form

$$u^\mu(x) = (\cosh \eta \cosh \eta_t(r), \sinh \eta_t(r) \mathbf{e}_r, \sinh \eta \cosh \eta_t(r)), \quad (60)$$

with a boost-invariant longitudinal flow rapidity $\eta_l = \eta$ ($v_l = z/t$) and a linear transverse flow rapidity profile

$$\eta_t(r) = \eta_f \left(\frac{r}{R} \right). \quad (61)$$

η_f scales the strength of the transverse flow. The exponent of the Boltzmann factor in (59) can then be written as

$$K \cdot u(x) = M_\perp \cosh(Y - \eta) \cosh \eta_t(r) - \mathbf{K}_\perp \cdot \mathbf{e}_r \sinh \eta_t(r). \quad (62)$$

For vanishing transverse flow ($\eta_f = 0$) the source depends only on M_\perp and remains azimuthally symmetric for all K_\perp . In this case the sideward and longitudinal HBT radii (55) and (57) exhibit perfect M_\perp -scaling, i.e. when plotted as functions of M_\perp they coincide for pion and kaon pairs [103]. [In fact, R_s does not depend on M_\perp at all in this limit.] For the outward radius M_\perp -scaling is broken by the β_\perp -dependent terms in Eq. (56). For non-zero transverse flow, R_s does depend on M_\perp , at a level that directly reflects the strength of the transverse flow (see below). In this case the M_\perp -scaling of R_s and R_l is broken by the K_\perp -dependent second term in the thermal exponent (62), albeit only weakly [103].

Using saddle-point integration, the HBT radii (55-57) for this source can be approximately evaluated analytically [114]. For pairs with $Y = 0$ one finds the simple pocket formulae

$$R_s^2 = R_*^2, \quad (63)$$

$$R_o^2 = R_*^2 + \beta_\perp^2 (\Delta t_*)^2, \quad (64)$$

$$R_l^2 = L_*^2, \quad (65)$$

with

$$\frac{1}{R_*^2} = \frac{1}{R^2} + \frac{1}{R_{\text{flow}}^2}, \quad (66)$$

$$(\Delta t_*)^2 = (\Delta \tau)^2 + 2 \left(\sqrt{\tau_0^2 + L_*^2} - \tau_0 \right)^2, \quad (67)$$

$$\frac{1}{L_*^2} = \frac{1}{(\tau_0 \Delta \eta)^2} + \frac{1}{L_{\text{flow}}^2}. \quad (68)$$

Here R_{flow} and L_{flow} are the transverse and longitudinal “dynamical lengths of homogeneity” generated by the expansion velocity gradients:

$$R_{\text{flow}}(M_\perp) = \frac{R}{\eta_f} \sqrt{\frac{T}{M_\perp}} = \frac{1}{\partial \eta_t(r)/\partial r} \sqrt{\frac{T}{M_\perp}}, \quad (69)$$

$$L_{\text{flow}}(M_\perp) = \tau_0 \sqrt{\frac{T}{M_\perp}} = \frac{1}{\partial \cdot u_l} \sqrt{\frac{T}{M_\perp}}, \quad (70)$$

where u_l is the longitudinal 4-velocity. These expressions show explicitly the competition between flow gradients and thermal smearing (reflected in the factor $\sqrt{T/M_\perp}$) which I mentioned above. They also show the competition between the overall geometric size of the source and the “dynamical homogeneity lengths”, with the smaller of the two controlling the HBT radii. The second term in the expression (67) for the emission duration reflects the fact that the emission duration is measured in terms of the *coordinate* time in the fixed center-of-mass reference frame, whereas freeze-out occurs at constant *proper* time τ_0 which, over the longitudinal range L_* probed by the longitudinal HBT radius, explores a finite range of coordinate times even if the proper time spread $\Delta \tau$ is set to zero. For freeze-out along a hyperbola of fixed proper time, it is therefore impossible to get a vanishing emission duration Δt_* .

For a longitudinally boost-invariant source ($\Delta \eta \rightarrow \infty$) and weak transverse expansion the source function integral in Eq. (57) can actually be done exactly [118], and one finds instead of (65,70)

$$R_l^2 = \tau_0^2 \frac{T}{M_\perp} \frac{K_2(M_\perp/T)}{K_1(M_\perp/T)}. \quad (71)$$

For small $M_\perp \simeq T$, this differs by up to a factor of 2 from Eq. (70).

5.4.2 HBT radii from Au+Au collisions at RHIC — the “HBT Puzzle”

Let us now study the HBT radii predicted by the hydrodynamic model introduced in Section 4.1.9, which was very successful in reproducing the single particle momentum spectra, and compare them with data from RHIC.

The hydrodynamic emission function, which implements sudden decoupling on a sharp freeze-out surface Σ as described in Section 4.1.5, takes the form [119, 120]

$$S_i(x, K) = \frac{g_i}{(2\pi)^3} \int_\Sigma \frac{K \cdot d^3 \sigma(x') \delta^4(x - x')}{\exp\{[K \cdot u(x') - \mu_i(x')]/T_{\text{dec}}(x')\} \pm 1}. \quad (72)$$

Phenomenological fits to spectra and HBT data often use a generalization of this form which replaces the δ -function by allowing for a spread of emission times (“fuzzy freeze-out”) [114, 117, 121].

For a longitudinally boost invariant source the freeze-out hypersurface can be parametrized in terms of the freeze-out eigentime as a function of the transverse coordinates, $\tau_f(x, y)$. The normal vector $d^3 \sigma_\mu$ on such a surface is given by

$$d^3 \sigma = \left(\cosh \eta, \nabla_\perp \tau_f(x, y), \sinh \eta \right) \tau_f(x, y) dx dy d\eta. \quad (73)$$

With the four momentum $K^\mu = (M_\perp \cosh Y, \mathbf{K}_\perp, M_\perp \sinh Y)$, where Y and M_\perp are the rapidity and transverse mass associated with K , Eq. (72) becomes

$$S_i(x, K) = \frac{g_i}{(2\pi)^3} \int_{-\infty}^{\infty} d\eta dx dy [M_\perp \cosh(Y - \eta) - \mathbf{K}_\perp \cdot \nabla_\perp \tau_f(x, y)] \times f(K \cdot u(x), x) \delta(\tau - \tau_f(x, y)) \quad (74)$$

with the flow-boasted local equilibrium distribution $f(K \cdot u(x), x)$ from (10).

With this expression we can now study the emissivity of the source as a function of mass and momentum of the particles. For the purpose of presentation we integrate the emission function over two of the four space-time coordinates and discuss the contours of equal emission density in the remaining two coordinates. We begin with calculations describing central Au+Au collisions at $\sqrt{s_{NN}} = 130$ GeV and focus on directly emitted pions, neglecting pions from unstable resonance decays. Resonance decay pions are known to produce non-Gaussian tails in the spatial emission distribution, increasing its width, but these tails are not efficiently picked up by a Gaussian fit to the width of the measured two-particle momentum correlation function [112, 122]. A comparison of the experimental HBT size parameters extracted from such fits with the spatial widths of the emission function is thus best performed by plotting the latter without resonance decay contributions.

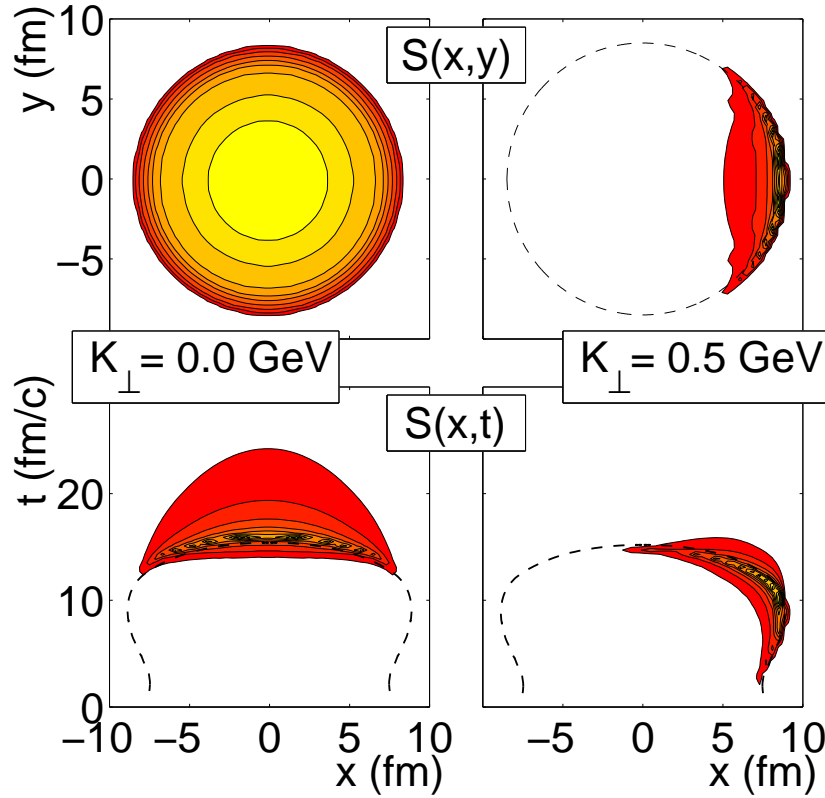


Fig. 20: Pion source function $S(x, K)$ for central Au+Au collisions at $\sqrt{s_{NN}} = 130$ GeV. The upper row shows the source after integrating out the longitudinal and temporal coordinate, in the lower row the source is integrated over the longitudinal and one transverse coordinate (y). In the left column we investigate the case $\mathbf{K} = 0$, in the right column the pions have rapidity $Y = 0$ and transverse momentum $K_\perp = 0.5$ GeV in x direction [88].

Figure 20 shows equal density contours at 10, 20, ..., 90% of the maximum in a transverse cut integrated over time and η (top row) and as a function of radius and time integrated over η and the second transverse coordinate (bottom row). The dashed circle in the top row indicates the largest freeze-out radius reached during the expansion, the dashed line in the bottom row gives the freeze-out surface $\tau_f(x, y=0) = t_f(x, y=z=0)$. Pions with vanishing transverse momentum (left column) are seen to come

from a broad region symmetric around the center and are emitted rather late. Pions with $K_{\perp} = 0.5$ GeV pointing in x -direction, on the other hand, are emitted on average somewhat earlier and only from a rather thin, crescent shaped sliver along the surface of the fireball at its point of largest transverse extension. The reason for this apparent “opacity” (surface dominated emission) of high- p_{\perp} particles is that they profit most from the radial collective flow which is largest near the fireball surface. Low- p_{\perp} pions don’t need the collective flow boost and are preferably emitted from smaller radii (where the flow velocity is smaller) when the freeze-out surface eventually reaches these points during the final stage of the decoupling process.

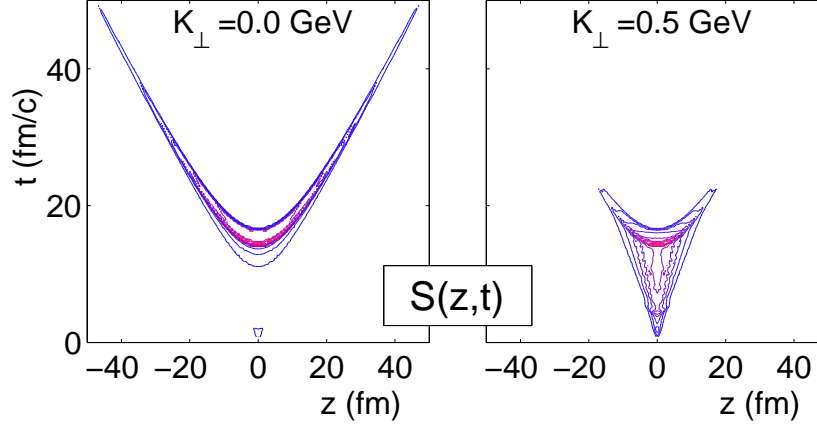


Fig. 21: Longitudinal cuts through the pion emission function $S(x, K)$, integrated over transverse coordinates, for $Y = 0$ pions with two different values of K_{\perp} as indicated [58].

Fig. 21 displays the time structure of the emission process along the beam direction. Especially for low transverse momenta one clearly sees a very long emission duration, as measured in the laboratory (center-of-momentum frame). The reason is that, according to the assumed longitudinal boost invariance, freeze-out happens at constant proper time $\tau = t^2 - z^2$ and extends over a significant range in longitudinal position z . This range is controlled by the competition between the longitudinal expansion velocity gradient (which makes emission of $Y = 0$ pions from points at large z values unlikely) and the thermal velocity smearing. If freeze-out happens late (large τ), the longitudinal velocity gradient $\sim 1/\tau$ is small and pions with zero longitudinal momentum are emitted with significant probability even from large values of $|z|$, i.e. very late in coordinate time t . Note that this is also visible in the lower left panel of Fig. 20 where significant particle emission still happens at times where the matter at $z = 0$ has already fully decoupled. We will see shortly that this poses a problem when compared with the data. The long tails at large values of $|z|$ and t can only be avoided by reducing τ_f (thereby increasing the longitudinal velocity gradient and reducing the z -range which contributes $Y = 0$ pions) and/or by additionally breaking longitudinal boost-invariance by reducing the particle density or postulating earlier freeze-out at larger space-time rapidities $|\eta|$ [72].

From earlier hydrodynamic calculations [123] it was expected that a fireball evolving through the quark-hadron phase transition would emit pions over a long time period, resulting in a large contribution $\beta_{\perp}^2 \langle t^2 \rangle$ to the outward HBT radius and a large ratio R_o/R_s . This should be a clear signal of the time-delay induced by the phase transition. It was therefore a big surprise when the first RHIC HBT data [124, 125] yielded $R_o/R_s \approx 1$ in the entire accessible K_{\perp} region (up to 0.7 GeV/c). In the meantime this finding has been shown to hold true out to $K_{\perp} \gtrsim 1.2$ GeV/c [126].

Figure 22 shows a comparison of the experimental data with results from hydrodynamic calculations [64]. Clearly, a purely hydrodynamic description with default initial conditions (solid lines in Fig. 22) fails to describe the measured HBT radii. The longitudinal and outward radii R_l and R_o are too large, R_s is too small, and the K_{\perp} -dependence of both R_o and R_s are too weak in the model. Since for longitudinally boost-invariant sources R_l is entirely controlled by the longitudinal velocity gradient

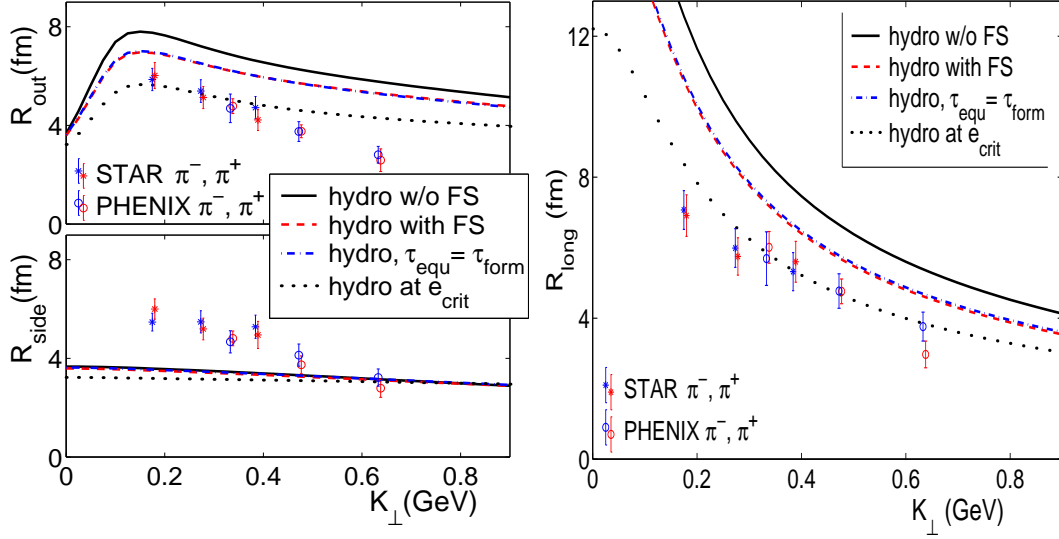


Fig. 22: HBT radii from hydrodynamic calculations [64] (solid lines) together with data from STAR [124] and PHENIX [125]. The dotted lines give hydrodynamic radii calculated directly after hadronization whereas the other two lines refer to different assumptions about the initial conditions (see text).

at freeze-out which decreases as $1/\tau_f$, making R_l smaller within the hydrodynamic approach requires letting the fireball decouple earlier [64] or breaking the boost invariance [72]. As noted above, a smaller R_l would also reduce the emission duration, i.e. $\langle t^2 \rangle$, and thus help to bring down R_o , especially if freeze-out at nonzero rapidities $|\eta| > 0$ happens earlier than at midrapidity.

The fireball can be forced to freeze out earlier by changing the freeze-out condition (e.g. by imposing freeze-out directly at hadronization, see dotted line in Fig. 22). This generates, however, serious conflicts with the single-particle spectra (see Sec. 4.1.9). Alternatively, one can allow transverse flow to build up sooner, either by seeding it with a non-zero value already at τ_{eq} (short dashed line labelled “hydro with FS” [64, 73]) or by letting the hydrodynamic stage begin even earlier (e.g. at $\tau_{form} = 0.2$ fm/c, long-dashed line). The last two options produce similar results, but do not fully resolve the problems with the magnitudes of R_l and R_o .

The situation may improve by taking also the breaking of longitudinal boost-invariance into account [72], but a fully consistent hydrodynamic description has not yet been found. In particular, the sideward radius R_s is still too small and the K_\perp -dependences of both R_s and R_o are still too weak [64, 72]. It is hard to see how to increase R_s without also increasing R_o and R_l which are already too large. Hybrid calculations [127] in which the hydrodynamic Cooper-Frye freeze-out is replaced by transition to a hadronic cascade at T_{cr} , followed by self-consistent kinetic freeze-out, tend to increase R_s by making freeze-out more “fuzzy”, but at the expense of also increasing R_o and R_l in a disproportionate manner, mainly due to an increase in the emission duration. This makes the problems with the R_o/R_s ratio even worse.

In the past, a strong K_\perp -dependence of R_s has been associated with strong transverse flow [103, 102]. It is therefore surprising that even the hydrodynamic model with its strong radial flow cannot reproduce the strong K_\perp -dependence of R_s measured at RHIC. Also, according to Eqs. (55,56) the difference between R_o^2 and R_s^2 can be reduced, especially at large K_\perp [121], if the positive contribution from the emission duration $\langle t^2 \rangle$ is compensated by “source opacity”, i.e. by a strongly surface-dominated emission process [115, 116, 128]. In this case the geometric contribution $\langle \tilde{x}_o^2 \rangle$ to R_o^2 is much smaller than $R_s^2 = \langle \tilde{x}_s^2 \rangle$. Again, the source produced by the hydrodynamic model (see top right panel in Fig. 20) is about as “opaque” as one can imagine [51], and it will be difficult to further increase the difference $\langle \tilde{x}_s^2 - x_o^2 \rangle$ [128].

This leaves almost only one way out of the “HBT puzzle”, namely the space-time correlation term

$-2\beta_{\perp} \langle \tilde{x}_o \tilde{t} \rangle$ in expression (56) for R_o^2 . It correlates the freeze-out position along the outward direction with the freeze-out time. The hydrodynamic model has the generic feature that, in the region where most particles are emitted (see Fig. 20), these two quantities are negatively correlated, because the freeze-out surface moves from the outside towards the center rather than the other way around. Hence the term $-2\beta_{\perp} \langle \tilde{x}_o \tilde{t} \rangle$ is positive and tends to make R_o^2 larger than R_s^2 . The small measured ratio $R_o/R_s \lesssim 1$ may instead call for strong *positive* x_o-t correlations, implying that particles emitted from *larger* x_o values decouple *later*. Hydrodynamics can not produce such a positive x_o-t correlation (at least not at RHIC energies). On the other hand, there are indications that microscopic models, such as the AMPT [122] and MPC [129] models, may produce them, for reasons which are not yet completely understood.

One should also not forget that Fig. 22 really compares two different things: The data are extracted from the width of the 2-particle correlator in momentum space while in theory one calculates the same quantities from the source width parameters in coordinate space. The two produce identical results only for Gaussian sources. The hydrodynamic source function shown in Figs. 20 and 21 are not very good Gaussians and show a lot of additional structure. We have checked, however, by explicit computation of the momentum-space correlation function using Eq. (49) that the non-Gaussian effects are small.² The largest non-Gaussian effects are seen in the longitudinal radius R_l [112], but although the corresponding corrections go in the right direction by making the R_l extracted from the momentum-space correlator smaller, the effect is only a fraction of 1 fm and not large enough to bridge the discrepancy with the data.

It was recently suggested [94, 130] that neglecting dissipative effects might be at the origin of the discrepancy between the purely hydrodynamic calculations and the data. A calculation of first-order dissipative corrections to the spectra and HBT radii at freeze-out [94], with a “reasonable” value for the viscosity, yielded a significant decrease of R_l along with a corresponding strong reduction of the emission duration contribution to R_o , both as desired by the data. There was no effect on the x_o-t correlations, however, and only a weak effect on R_s which went in the wrong direction, making it even flatter as a function of K_{\perp} . The rather steep K_{\perp} -dependence of the data for both R_s and R_o and the larger than predicted size of R_s at low K_{\perp} are therefore not explained by this mechanism [94, 129]. Furthermore, the elliptic flow v_2 has been shown to be very sensitive to viscosity [94, 95], and the viscosity values needed to produce the desired reduction in R_l turned out [94] to reduce v_2 almost by a factor 2, incompatible with the data. The “RHIC HBT puzzle” thus still awaits its resolution.

5.5 Non-central ($b \neq 0$) collisions — azimuthally sensitive HBT interferometry (asHBT)

In non-central collisions the azimuthal symmetry of the source is broken by the impact parameter vector \mathbf{b} which, together with the beam direction, defines the reaction plane. Pairs emitted at different azimuthal angles $\Phi = \angle(\mathbf{b}, \mathbf{K}_{\perp})$ relative to the reaction plane therefore originate in general from effective emission regions (homogeneity regions) of different sizes and shapes.

As a result, the components of the spatial correlation tensor $S_{\mu\nu} = \langle \tilde{x}_{\mu} \tilde{x}_{\nu} \rangle$ now depend not only on the magnitude of the transverse pair momentum K_{\perp} , but also on its angle Φ relative to the reaction plane. Furthermore, the source is no longer reflection symmetric with respect to the plane defined by the beam axis and \mathbf{K}_{\perp} (i.e. symmetric under $x_s \rightarrow -x_s$), so R_{os} and R_{ls} no longer vanish. This means that for non-central heavy-ion collisions we have to measure 6 (not 4) HBT radii, and they are functions not only of Y and K_{\perp} , but also of the emission angle Φ relative to the reaction plane. A complete HBT analysis of non-central heavy-ion collisions thus requires the event-wise determination of the reaction plane (through a Fourier analysis of the single particle spectrum as, for example, used for extracting the elliptic flow) and the investigation of the dependence of the HBT radii on the angle Φ relative to that plane.

²They would have been larger if we had included resonance decay pions in the emission function, as found by Lin *et al.* [122], which was our main reason for not doing so.

5.5.1 asHBT formalism

Experimentally it is still useful to characterize the source in terms of HBT radii R_o and R_s parallel and perpendicular to the transverse emission direction defined by the pair momentum \mathbf{K}_\perp . The emitting source $S(x, K)$, however, is most conveniently written down in transverse coordinates x, y aligned with the reaction plane, since it typically (at least for collisions between spherical nuclei) is symmetric under reflection with respect to that plane, $y \rightarrow -y$ combined with $\Phi \rightarrow -\Phi$. The analogue relations to Eqs. (55-57), which express the HBT radii through the components $S_{\mu\nu} = \langle \tilde{x}_\mu \tilde{x}_\nu \rangle$, therefore involve an explicit rotation by the angle Φ between the (x, y) axes characterizing the source $S_{\mu\nu}$ and the (x_o, x_s) axes defined by the emission direction \mathbf{K}_\perp [131, 132, 133]:

$$\begin{aligned}
R_s^2 &= \frac{1}{2}(S_{xx} + S_{yy}) - \frac{1}{2}(S_{xx} - S_{yy}) \cos(2\Phi) - S_{xy} \sin(2\Phi) \\
R_o^2 &= \frac{1}{2}(S_{xx} + S_{yy}) + \frac{1}{2}(S_{xx} - S_{yy}) \cos(2\Phi) + S_{xy} \sin(2\Phi) \\
&\quad - 2\beta_\perp (S_{tx} \cos \Phi + S_{ty} \sin \Phi) + \beta_\perp^2 S_{tt}, \\
R_{os}^2 &= S_{xy} \cos(2\Phi) - \frac{1}{2}(S_{xx} - S_{yy}) \sin(2\Phi) + \beta_\perp (S_{tx} \sin \Phi - S_{ty} \cos \Phi), \\
R_l^2 &= S_{zz} - 2\beta_L S_{tz} + \beta_L^2 S_{tt}, \\
R_{ol}^2 &= (S_{xz} - \beta_L S_{tx}) \cos \Phi + (S_{yz} - \beta_L S_{ty}) \sin \Phi - \beta_\perp S_{tz} + \beta_L \beta_\perp S_{tt}, \\
R_{sl}^2 &= (S_{yz} - \beta_L S_{ty}) \cos \Phi - (S_{xz} - \beta_L S_{tx}) \sin \Phi.
\end{aligned} \tag{75}$$

These equations exhibit the *explicit* Φ -dependence resulting from the rotation between the (x, y) and (x_o, x_s) axes, but not the *implicit* one reflecting the Φ dependence of the spatial correlation tensor $S_{\mu\nu}(Y, K_\perp, \Phi)$. The total emission angle dependence of the HBT radii results from the combination of both.

The implicit Φ -dependence of the spatial correlation tensor is restricted by symmetries of the source [133]. It is a relativistic effect associated with an azimuthal spatial source deformation superimposed by strong transverse collective flow [131, 134] which vanishes with the 4th power of the transverse flow velocity v_\perp/c for weak or no collective expansion [132, 134].

A full analysis of the symmetry constraints on $S_{\mu\nu}(Y, K_\perp, \Phi)$ for symmetric collisions between spherical nuclei and for pairs detected in a symmetric rapidity window around $Y = 0$ was performed in Ref. [133]. One finds the following *most general* form for the azimuthal oscillations of the HBT radii:

$$\begin{aligned}
R_s^2 &= R_{s,0}^2 + 2 \sum_{n=2,4,6,\dots} R_{s,n}^2 \cos(n\Phi), \\
R_{os}^2 &= 2 \sum_{n=2,4,6,\dots} R_{os,n}^2 \sin(n\Phi), \\
R_o^2 &= R_{o,0}^2 + 2 \sum_{n=2,4,6,\dots} R_{o,n}^2 \cos(n\Phi), \\
R_{ol}^2 &= 2 \sum_{n=1,3,5,\dots} R_{ol,n}^2 \cos(n\Phi), \\
R_l^2 &= R_{l,0}^2 + 2 \sum_{n=2,4,6,\dots} R_{l,n}^2 \cos(n\Phi), \\
R_{sl}^2 &= 2 \sum_{n=1,3,5,\dots} R_{sl,n}^2 \sin(n\Phi).
\end{aligned} \tag{76}$$

We see that only even *or* odd sine *or* cosine terms occur, but no mixtures of such terms. Statistical errors in the resolution of the reaction plane angle as well as finite angular bin sizes in Φ tend to reduce the actually measured oscillation amplitudes; fortunately, these dilution effects can be fully corrected by a model-independent correction algorithm [133, 135]. A Gaussian fit to the thus corrected correlation function, binned in Y , K_\perp and emission angle Φ , then yields the “true” HBT radius parameters

$R_{ij}^2(Y, K_\perp, \Phi)$ from which the n^{th} order azimuthal oscillation amplitudes are extracted via

$$R_{ij,n}^2(Y, K_\perp) = \frac{1}{n_{\text{bin}}} \sum_{j=1}^{n_{\text{bin}}} R_{ij}^2(Y, K_\perp, \Phi_j) \text{osc}(n\Phi_j). \quad (77)$$

Here n_{bin} indicates the number of (equally spaced) Φ bins in the data and $\text{osc}(n\Phi_j)$ stands for $\sin(n\Phi_j)$ or $\cos(n\Phi_j)$ as appropriate, see Eqs. (76). (Note that Nyquist's theorem limits the number of harmonics that can be extracted to $n \leq n_{\text{bin}}$.)

We would like to relate the azimuthal oscillation amplitudes of the 6 HBT radius parameters to the geometric and dynamical anisotropies of the source, as reflected in the azimuthal oscillations of the 10 independent components of the spatial correlation tensor. Their allowed oscillation patterns at midrapidity $Y = 0$ are given by [133]

$$\begin{aligned} A(\Phi) &\equiv \frac{1}{2} \langle \tilde{x}^2 + \tilde{y}^2 \rangle = A_0 + 2 \sum_{n \geq 2, \text{even}} A_n \cos(n\Phi), \\ B(\Phi) &\equiv \frac{1}{2} \langle \tilde{x}^2 - \tilde{y}^2 \rangle = B_0 + 2 \sum_{n \geq 2, \text{even}} B_n \cos(n\Phi), \\ C(\Phi) &\equiv \langle \tilde{x} \tilde{y} \rangle = 2 \sum_{n \geq 2, \text{even}} C_n \sin(n\Phi), \\ D(\Phi) &\equiv \langle \tilde{t}^2 \rangle = D_0 + 2 \sum_{n \geq 2, \text{even}} D_n \cos(n\Phi), \\ E(\Phi) &\equiv \langle \tilde{t} \tilde{x} \rangle = 2 \sum_{n \geq 1, \text{odd}} E_n \cos(n\Phi), \\ F(\Phi) &\equiv \langle \tilde{t} \tilde{y} \rangle = 2 \sum_{n \geq 1, \text{odd}} F_n \sin(n\Phi), \\ G(\Phi) &\equiv \langle \tilde{t} \tilde{z} \rangle = 2 \sum_{n \geq 1, \text{odd}} G_n \cos(n\Phi), \\ H(\Phi) &\equiv \langle \tilde{x} \tilde{z} \rangle = H_0 + 2 \sum_{n \geq 2, \text{even}} H_n \cos(n\Phi), \\ I(\Phi) &\equiv \langle \tilde{y} \tilde{z} \rangle = 2 \sum_{n \geq 2, \text{even}} I_n \cos(n\Phi), \\ J(\Phi) &\equiv \langle \tilde{z}^2 \rangle = J_0 + 2 \sum_{n \geq 2, \text{even}} J_n \cos(n\Phi). \end{aligned} \quad (78)$$

The missing terms in the sums over n have amplitudes which are odd functions of Y and vanish at midrapidity. They do, however, contribute to the HBT radii if the data are averaged over a finite, symmetric rapidity window around $Y = 0$ [133]. Their contributions can be eliminated by varying the width ΔY of this rapidity window and extrapolating quadratically to $\Delta Y \rightarrow 0$. Note that $C_0 = E_0 = F_0 = G_0 = I_0 = 0$ by symmetry, i.e. the corresponding components of $S_{\mu\nu}$ oscillate around zero.

The oscillation amplitudes of the HBT radii relate to the oscillation amplitudes of the source parameters as follows [133, 136]: For the odd harmonics $n = 1, 3, 5, \dots$ we have

$$\begin{aligned} R_{ol,n}^2 &= \frac{1}{2} \langle H_{n-1} + H_{n+1} - I_{n-1} + I_{n+1} - \beta_L (E_{n-1} + E_{n+1} - F_{n-1} + F_{n+1}) \rangle \\ &\quad - \langle \beta_\perp G_n - \beta_L D_n \rangle, \\ R_{sl,n}^2 &= \frac{1}{2} \langle -H_{n-1} + H_{n+1} + I_{n-1} + I_{n+1} - \beta_L (-E_{n-1} + E_{n+1} + F_{n-1} + F_{n+1}) \rangle, \end{aligned} \quad (79)$$

whereas the even harmonics $n = 0, 2, 4, \dots$ satisfy

$$\begin{aligned} R_{s,n}^2 &= \langle A_n \rangle + \frac{1}{2} \langle -B_{n-2} - B_{n+2} + C_{n-2} - C_{n+2} \rangle, \\ R_{o,n}^2 &= \langle A_n \rangle + \frac{1}{2} \langle B_{n-2} + B_{n+2} - C_{n-2} + C_{n+2} \rangle \\ &\quad - \beta_\perp \langle E_{n-1} + E_{n+1} - F_{n-1} + F_{n+1} \rangle + \beta_\perp^2 \langle D_n \rangle, \\ R_{os,n}^2 &= \frac{1}{2} \langle -B_{n-2} + B_{n+2} + C_{n-2} + C_{n+2} + \beta_\perp (E_{n-1} - E_{n+1} - F_{n-1} - F_{n+1}) \rangle, \\ R_{l,n}^2 &= \langle J_n \rangle - 2 \langle \beta_L G_n \rangle + \langle \beta_L^2 D_n \rangle. \end{aligned} \quad (80)$$

In these relations it is understood that all negative harmonic coefficients $n < 0$ as well as C_0, E_0, F_0, G_0 and I_0 are zero. The angular brackets $\langle \dots \rangle$ indicate an average over a finite, symmetric rapidity window around $Y = 0$. The terms involving the longitudinal pair velocity β_L vanish quadratically as the width ΔY of that window shrinks to zero.

Even after extrapolating to $Y=0$ in this way, we have still many more source parameters than measurable HBT amplitudes. One counts easily that up to $n=2$ there are 9 measurable Fourier coefficients which (at $Y=0$) depend on 19 source amplitudes. From there on, increasing n by 2 yields 6 additional measured amplitudes which depend on 10 additional source amplitudes. This lack of analysis power is an intrinsic weakness of the HBT microscope and due to the fundamental restrictions arising from the mass-shell constraint $q^0 = \beta \cdot q$. The reconstruction of the source thus must necessarily rely on additional assumptions.

One such assumption which may not be too unreasonable is that the emission duration $D = \langle \tilde{t}^2 \rangle$ is approximately independent of emission angle and that the source is sufficiently smooth that higher order harmonics $n \geq 3$ of $S_{\mu\nu}$ can be neglected. Such source properties would result in the “Wiedemann sum rule” [131]

$$R_{o,2}^2 - R_{s,2}^2 + 2R_{os,2}^2 = 0 \quad (81)$$

which can be experimentally tested. If verified for all K_\perp it would provide strong support for the underlying assumptions on the source. In this case we can measure 3 azimuthally averaged HBT radii and 5 independent oscillation amplitudes with $n \leq 2$, depending on 14 source parameters of which 5 can be eliminated by going to $K_\perp = \beta_\perp = 0$ (see [133] for explicit expressions). This makes the geometry of the effective source for particles with $K_\perp = 0$ “almost solvable”³, as confirmed by hydrodynamical calculations [51] which show that at $K_\perp = 0$ the effective emission region closely tracks the overall geometry of the source even if it is strongly and anisotropically expanding.

The source geometry can be completely reconstructed from HBT data if transverse flow is so weak that all implicit Φ -dependence (i.e. all higher harmonics $n \geq 1$) of $S_{\mu\nu}$ can be neglected. In this case one obtains at $Y=0$ the “geometric relations” [132]

$$\begin{aligned} R_{s,0}^2 &= A_0 = \frac{1}{2} \langle \tilde{x}^2 + \tilde{y}^2 \rangle_0, \\ R_{o,0}^2 - R_{s,0}^2 &= \beta_\perp^2 D_0 = \beta_\perp^2 \langle \tilde{t}^2 \rangle_0, \\ R_{l,0}^2 &= J_0 = \langle \tilde{z}^2 \rangle_0, \\ R_{ol,1}^2 &= -R_{sl,1}^2 = \frac{1}{2} H_0 = \frac{1}{2} \langle \tilde{x} \tilde{z} \rangle_0, \\ R_{o,2}^2 &= -R_{s,2}^2 = -R_{os,2}^2 = \frac{1}{2} B_0 = \frac{1}{4} \langle \tilde{x}^2 - \tilde{y}^2 \rangle_0. \end{aligned} \quad (82)$$

A_0 describes the average transverse size and B_0 (which generates a second-order harmonic in the transverse HBT radii) the transverse deformation of the source. H_0 generates a first-order harmonic in the ol and sl cross terms and describes a longitudinal tilt of the source away from the beam direction [132]. Such a tilt was found in Au+Au collisions at the AGS [138]. Its sign yielded important information on the kinetic pion production mechanism [132, 138].

5.5.2 Azimuthal oscillations of HBT radii in hydrodynamics and RHIC data

We can use the hydrodynamic model introduced in Section 4.1.9 to describe the momentum spectra and explore what it would predict for the azimuthal oscillations of the HBT radii in non-central Au+Au collisions at RHIC [51]. The most interesting question, perhaps, is whether we can reconstruct the orientation and magnitude of the *spatial* deformation of the source at freeze-out from the HBT analysis, thereby complementing our knowledge of the orientation and magnitude of the *momentum* anisotropy from the elliptic flow analysis.

³Note that the limit $K_\perp \rightarrow 0$ eliminates all influence from the temporal structure of the source; the emission duration and correlations between position and time at freeze-out must be extracted from correlation data at non-zero K_\perp where, however, the explicit β_\perp -dependence associated with factors t in the variances $\langle \tilde{x}_\mu \tilde{x}_\nu \rangle$ interferes with the implicit K_\perp -dependence in the spatial variances which result from collective expansion flow [103]. Models for disentangling these different contributions to the K_\perp -dependence have been extensively studied for azimuthally symmetric sources [103], but must be generalized for azimuthally deformed sources [137].

To see how different orientations of the spatial deformation (in-plane elongated vs. out-of-plane elongated) manifest themselves in the azimuthal oscillations of the HBT radii, one can explicitly construct sources of either orientation and perform an HBT analysis on them. Since the elliptic flow makes the fireball expand faster into the reaction plane than perpendicular to it, we can generate an in-plane elongated source (IPES) at freeze-out from the initial out-of-plane oriented overlap region simply by making sure that the elliptic flow has enough time to act before the system decouples. By increasing the initial energy density or temperature, we can make the total time until decoupling arbitrarily large. Let us therefore study hydrodynamic sources evolving from different sets of initial conditions [51].

The first set (labelled “RHIC1”) corresponds to optimized values for central Au+Au collisions at $\sqrt{s_{\text{NN}}} = 130$ GeV which were used earlier in Section 4.1.9 (see Table 1). The second set of initial conditions (labelled “IPES”) uses a much higher initial temperature $T_{\text{eq}} = 2$ GeV (at $b = 0$), and the hydrodynamic evolution is started at $\tau_{\text{eq}} = 0.1$ fm/c and stopped when a freeze-out temperature $T_{\text{dec}} = 100$ MeV has been reached. Such a high initial temperature can probably not even be achieved at the LHC, and the strong transverse flow generated in this case probably causes the system to decouple already much closer to the hadronization temperature $T_{\text{cr}} = 164$ MeV. But if we force the system to start at such a high temperature and freeze out so low, we give it enough time to convert the initial out-of-plane deformation into a final in-plane deformation (which is the phenomenon we want to study). The following analysis refers to semi-peripheral Au+Au collisions with impact parameter $b = 7$ fm.

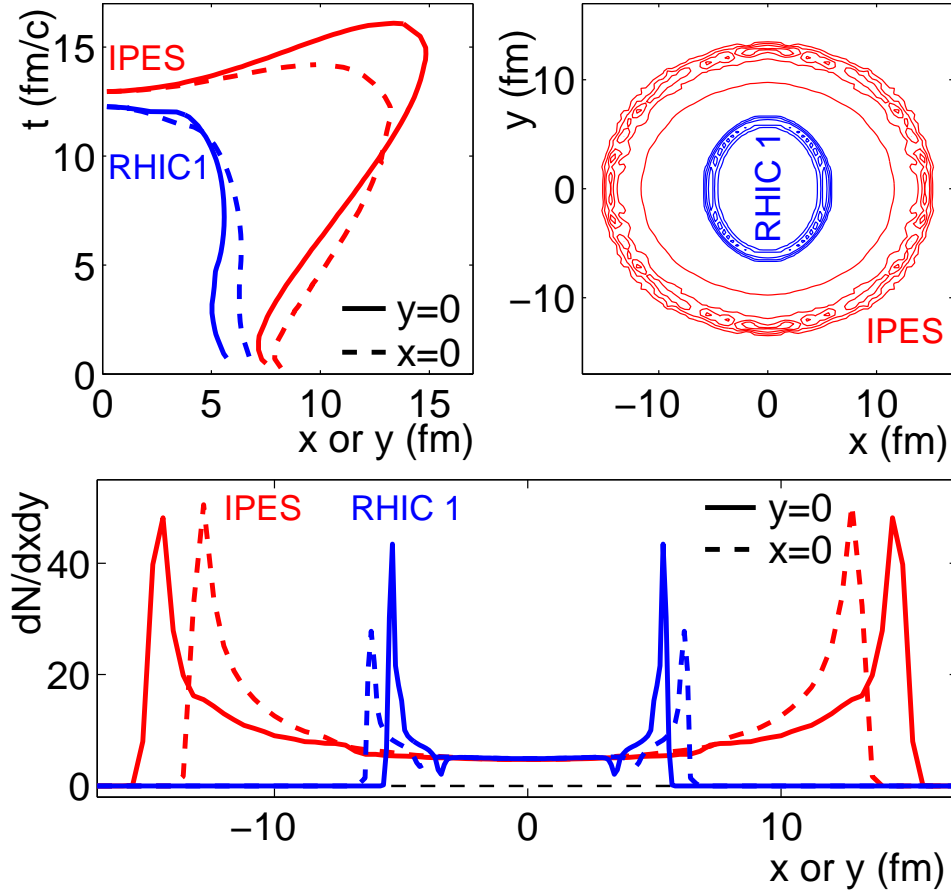


Fig. 23: (a) Cuts through the freeze-out surface $t_f(\mathbf{r})$ at $z = 0$ along and perpendicular to the reaction plane. (b) Contour plots in the transverse plane of the time-, z -, and momentum-integrated emission function d^2N/d^2r for RHIC1 and IPES initial conditions (see text). (c) Cuts through diagram (b) along and perpendicular to the reaction plane, for RHIC1 and IPES initial conditions. In all cases $b = 7$ fm.

Figure 23a shows the freeze-out surface $t_{\text{dec}}(\mathbf{r})$ in cuts along ($y = 0$) and perpendicular to the

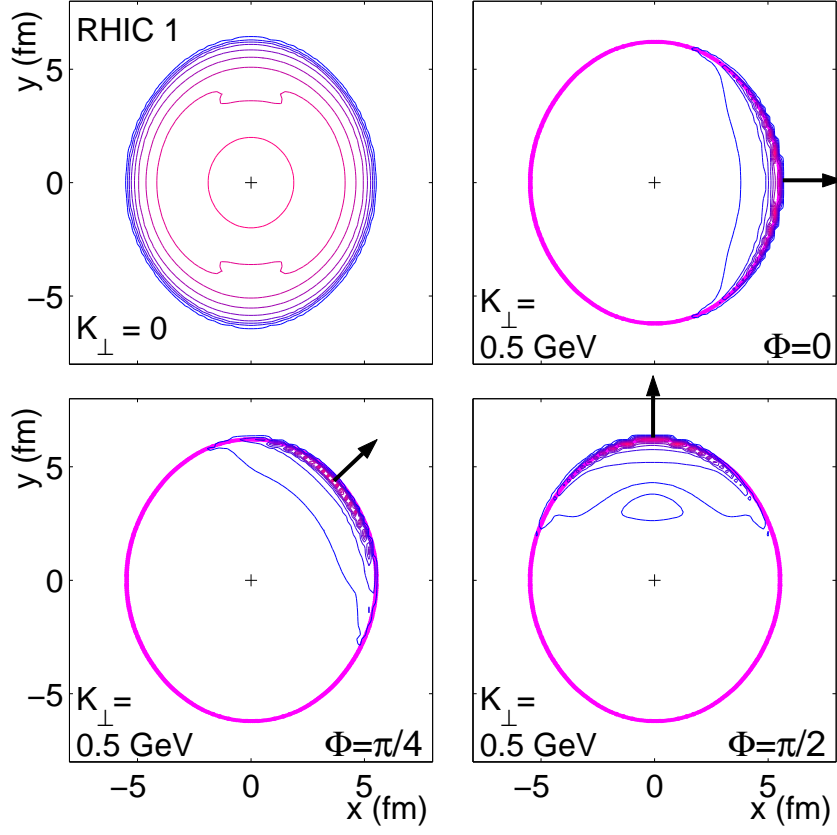


Fig. 24: Contours of constant emission density in the transverse plane for RHIC1 initial conditions (see text). The thick line indicates the largest transverse extension of the freeze-out hypersurface (see Figs. 23a,b). The four panels show emission regions for midrapidity pions ($Y = 0$) with $K_{\perp} = 0$ and, for three emission angles indicated by arrows, with $K_{\perp} = 0.5$ GeV.

reaction plane ($x = 0$). Initially the source is extended out-of-plane (larger in y than in x direction), but it then expands more rapidly into the x -direction, becoming in-plane elongated at later times. For RHIC1 initial conditions this only happens after most of the matter has already decoupled; as a consequence the time-integrated source, shown in Fig. 23b, is still longer in y than in x direction in the RHIC1 case. For IPES initial conditions the deformation changes sign before most particles decouple, and the time-integrated source appears in-plane-extended (see again Fig. 23b). Also, it is much larger due to the much higher initial energy density and longer lifetime.

Figure 23c shows cuts along and perpendicular to the reaction plane through the density contour plots $d^2N/d^2r = \int (d^3K/E_K) dz dt S(x, K)$ of Fig. 23b. Pion emission is seen to be strongly surface peaked, in particular at RHIC1 where the freeze-out radius is almost constant for a long time. This “opacity” is weaker both at lower collision energies (where the freeze-out surface shrinks to zero continuously [50]) and at higher energies, due to larger temporal variations of the freeze-out radius.

Figures 24 and 25 show the spatial distributions of pions emitted with fixed momentum. Shown are density contours of $\int dz dt S(x, K)$ in the transverse plane (x, y) for pions with rapidity $Y = 0$ and fixed K_{\perp} , for three emission angles $\Phi = 0, 45^\circ$ and 90° relative to the reaction plane. (In Fig. 25 we replaced $\Phi = 45^\circ$ for clarity by the equivalent angle $\Phi = 225^\circ$.) Particles with vanishing transverse momentum K_{\perp} are seen to be emitted from almost the entire interior of the “bathtub” shown in Figs. 23b,c; for RHIC1 (IPES) initial conditions this region is elongated out-of-plane (in-plane). For slow pions the source thus looks transparent. Pions with sufficiently large transverse momenta are emitted from relatively thin regions close to the rim of the “bathtub” where the flow velocity is largest and points into the direction of the emitted pions. For fast pions the source thus looks opaque, more so at RHIC than at

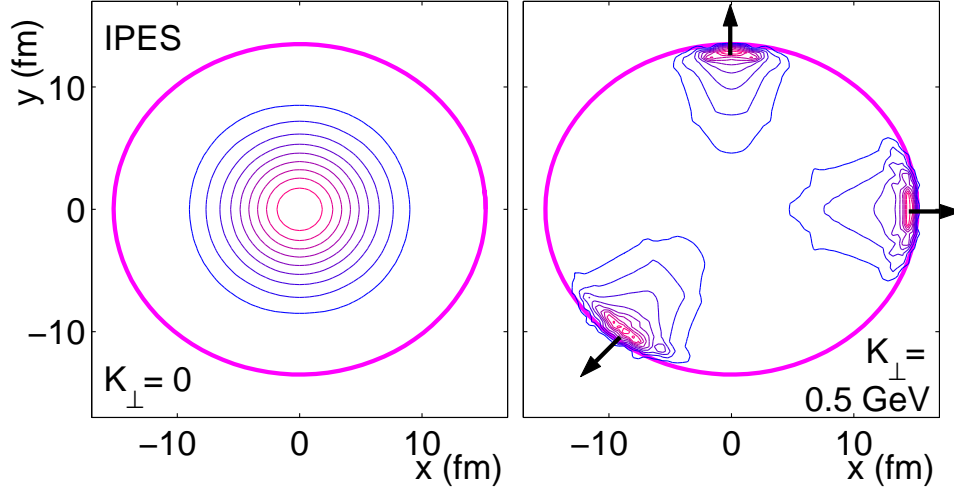


Fig. 25: Same as Fig. 24, but for IPES initial conditions.

higher energies. Their emission regions rotate with the emission angle, constrained by the shape of the “bathtub”.

The HBT radii, calculated from the widths of the K -dependent emission regions according to Eqs. (75), are shown in Fig. 26, as functions of the azimuthal emission angle Φ . (Since $Y=0$, all terms $\sim \beta_L$ vanish.) Note that R_o^2 and R_{os}^2 receive purely geometric and mixed space-time correlation contributions; the latter are proportional to the pair velocity β_\perp . Since we want to use pion interferometry to obtain information on the geometric deformation of the source at freeze-out, these should be analyzed separately. In the right panel of Fig. 26 we therefore show the geometric contributions separately as thin circled lines. For a detailed discussion of all the curves in Fig. 26 I refer the reader to Ref. [51]; here I will only discuss the most important point.

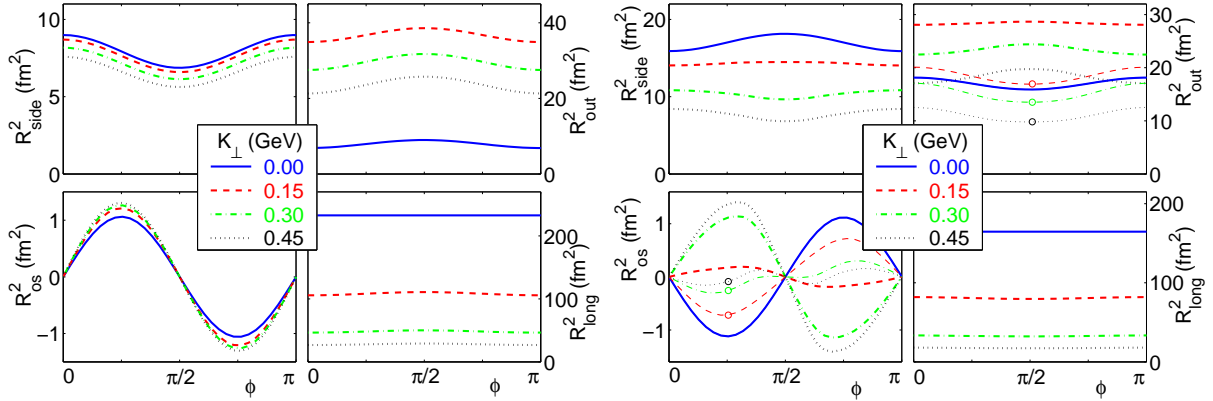


Fig. 26: Left: Azimuthal oscillations of the HBT radii at $Y=0$ for $b=7$ fm Au+Au collisions at $\sqrt{s_{NN}}=130$ GeV (RHIC1), for four values of the transverse momentum K_\perp as indicated. Right: The same for IPES initial conditions. For R_o^2 and R_{os}^2 the geometric contributions are shown separately as thin circled lines.

Let us first look at the geometric contributions. From Figs. 24 and 25 we already know that pions with $K_\perp=0$ are emitted from almost the entire fireball and thus probe the different sign of the spatial deformation of the *total* (momentum-integrated) RHIC1 and IPES sources shown in Fig. 23. This is reflected by the opposite sign of the oscillation amplitudes of R_s^2 and of the geometric contribution to R_o^2 at $K_\perp=0$ in the left and right panels of Fig. 26. At higher K_\perp -values the oscillations for R_s^2 in the right panel Fig. 26 change sign, but those of the geometric contribution to R_o^2 do not. This reflects an

intricate interplay between geometric and flow effects [51]. However, the opposite signs of the oscillation amplitudes near $K_\perp = 0$ of R_s^2 , R_o^2 , and R_{os}^2 for the RHIC1 and IPES sources are clear and unique indicators of the opposite directions of the spatial deformation for these two sources and can thus be used to diagnose the latter. In particular, the ratio of the second harmonic oscillation amplitude $R_{s,2}^2$ of the sideward radius to its Φ -averaged value $R_{s,0}^2$ is seen to be almost independent of K_\perp [51, 137]. This ratio can therefore be used to extract the spatial deformation of the *entire* source even at non-zero (albeit not too large) K_\perp , even though the homogeneity regions at non-zero K_\perp do not probe the entire source [137, 139].

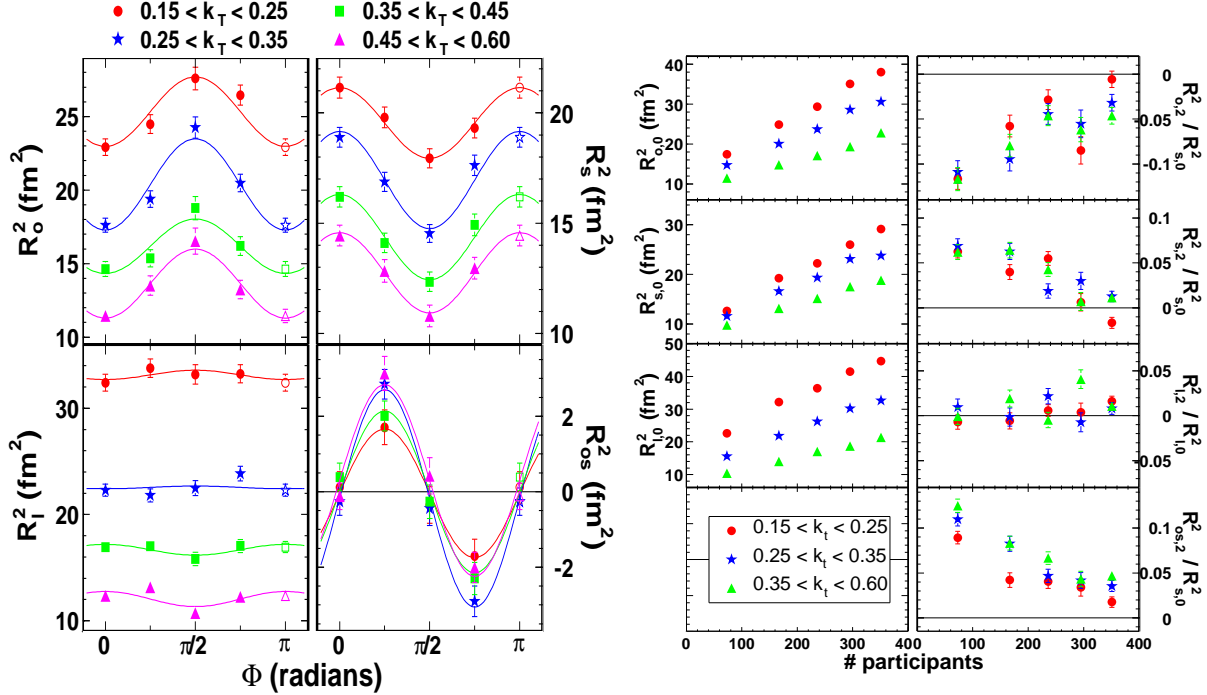


Fig. 27: Left: Azimuthal oscillations of the HBT radii near $Y = 0$ from Au+Au collisions at $\sqrt{s_{NN}} = 200$ GeV, for 20%-30% centrality events and four bins of the transverse momentum K_\perp (GeV/c) [139]. The lines show fits with Eqs. (76). Right: Zeroth order (left column) and normalized second order (right column) harmonic coefficients of the HBT radii, for three K_\perp bins (stars, circles, and triangles), as a function of collision centrality, from the same STAR experiment [139]. Larger participant numbers correspond to more central collisions.

Recently, the STAR Collaboration published the first azimuthally sensitive HBT analysis of Au+Au collisions at RHIC [139]. As you can see in Fig. 27, the quality and level of detail of the data is impressive. The analysis is fully 3-dimensional in the relative momentum \mathbf{q} and sufficiently finely binned in K_\perp , Φ , and collision centrality to obtain a reasonably complete HBT snapshot of the final state of the collision fireball created at RHIC. (Of course, theorists will always keep asking for more detail, but even that is coming.) It is clear that with these asHBT data a new dimension has opened, with unprecedented constraining power on theories!

Comparing the left panels in Figs. 26 and 27 one sees very strong similarity. The absolute scales on the vertical axes don't match, but this just reflects the “RHIC HBT puzzle” from the previous subsection, namely that the hydrodynamic model does not reproduce the angle-averaged HBT radii and overpredicts R_l and R_o while underpredicting R_s . The signs of the oscillation amplitudes match, however, clearly indicating that the measured source is still somewhat out-of-plane elongated at freeze-out, as predicted by the hydrodynamic model (see Figs. 23 and 24). The centrality systematics shown in the right panel of Fig. 27 shows that the HBT radii grow as the collisions become more central (left column – no surprise there), but that the growth rate decreases, together with the radii themselves, as the pair momentum K_\perp increases. This is qualitatively consistent with strong longitudinal and radial flow, as discussed in the

previous section, even though the measured K_{\perp} -dependence of $R_{s,0}^2$ and $R_{o,0}^2$ is stronger than predicted. The experimental data show that the strong K_{\perp} -dependence of $R_{s,0}^2$ in particular is not only a feature of central collisions, but seems to persist towards peripheral collisions.

The rightmost column of Fig. 27 shows that the oscillation amplitudes are largest in peripheral collisions and decrease to zero in central collisions. Again this is no surprise since the oscillations reflect the geometric deformation of the source and peripheral collisions produce, at least initially, the most deformed fireballs. Note the very weak K_{\perp} -dependence of the *relative* oscillation amplitudes which is, at least qualitatively, consistent with hydrodynamic predictions. A more quantitative analysis of the source

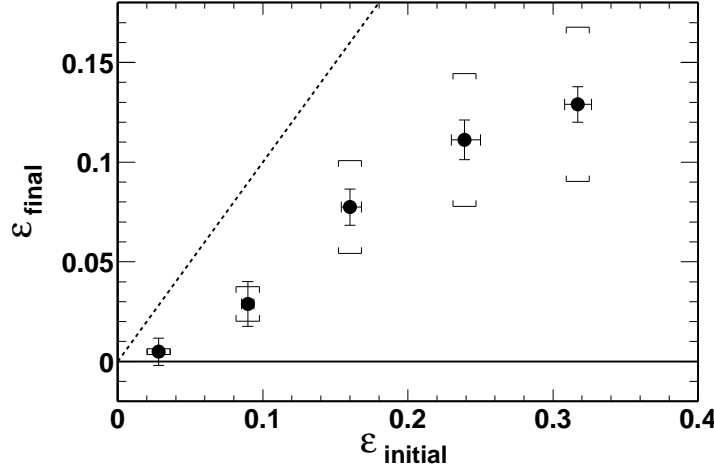


Fig. 28: Final source eccentricity at freeze-out, ϵ_{final} , extracted from the normalized second order harmonic coefficient of the sideward HBT radius, $R_{s,2}^2/R_{s,0}^2$ [137] (see text), as a function of the initial eccentricity, $\epsilon_{\text{initial}}$, from a Glauber model. Smaller eccentricities correspond to more central collisions. The dotted line indicates $\epsilon_{\text{initial}} = \epsilon_{\text{final}}$. The data are from Au+Au collisions at $\sqrt{s_{\text{NN}}} = 200$ GeV measured by STAR [139].

deformation as a function of centrality is presented in Fig. 28 from the same publication [139], where the final spatial eccentricity ϵ_{final} at decoupling, extracted from the normalized oscillation amplitude $R_{s,2}^2/R_{s,0}^2$ with the help of a blast-wave model parametrization of the source [137], is contrasted with the initial spatial deformation $\epsilon_{\text{initial}}$ of the original nuclear overlap zone, calculated from the Glauber model. At all impact parameters, the final deformation is smaller than the initial one, showing the consequences of elliptic flow. Relatively speaking, the reduction of the eccentricity is stronger in almost central than in peripheral collisions, but at no centrality does the freeze-out configuration exhibit a negative value for ϵ_{final} , which would indicate an in-plane-elongated source. For mid-peripheral ($b \sim 7$ fm) collisions (second point from the right), the extracted value $\epsilon_{\text{final}} = 0.11 \pm 0.035$ agrees (within the relatively large systematic error of about 30%) with the eccentricity of the hydrodynamic source shown in Figs. 23,24 which has $\epsilon_x \simeq 0.14$. This provides further support for the hydrodynamic model, since it indicates an intrinsic dynamical consistency between the evolution of the eccentricity from its initial to its final value and the hydrodynamic expansion time scales and flow profiles. A stronger and more confident statement requires, of course, the resolution of the “HBT puzzle”, i.e. a quantitative theoretical understanding of the angle-averaged HBT radii which is so far missing.

5.6 What has HBT interferometry of heavy-ion collisions taught us?

Let me quickly summarize this long chapter by stating the following as our **Third Lesson**: Two-particle momentum correlations, in particular Bose-Einstein correlations between pairs of identical bosons, are a powerful tool to constrain the *space-time structure and evolution* of the heavy-ion fireball, thereby yielding complementary information to its *momentum-space structure* extracted from the single-particle

spectra. Emission-angle dependent HBT interferometry for non-central collisions (or central collisions between deformed nuclei) allows to extract the shape and orientation of the deformed source at freeze-out. By comparing it with the initial spatial deformation of the nuclear overlap region when the nuclei first hit each other, we get an idea how the system evolved and can constrain the time between impact and decoupling. Azimuthally sensitive HBT interferometry (asHBT) is a newly developing field, but first results indicate consistency of the extracted final deformation with hydrodynamic evolution models. On the other hand, the absolute magnitudes of the emission-angle averaged HBT radii and their dependence on the transverse momentum K_\perp of the emitted pairs is still poorly understood: Almost all dynamical models overpredict R_l and R_o , underpredict R_s and are unable to reproduce the measured strong K_\perp -dependence of the transverse radii R_s and R_o . This “**RHIC HBT Puzzle**” indicates that our understanding of the kinetics of the freeze-out process is still insufficient and constitutes, in my opinion, the most important open problem in our present global picture of heavy-ion collision dynamics.

6 STATISTICAL HADRONIZATION AND PRIMORDIAL HADROSYNTHESIS

In this section we’ll discuss what kind of information can be extracted from the measured hadron abundances (i.e. from the *normalization* of the hadron spectra, in contrast to their *shape* which we discussed in the previous section). Up to this point we did not discuss the normalization of any of the spectra, nor did we care about it. All we needed for local thermal equilibrium and the build-up of thermal pressure and collective flow was rapid momentum equilibration, and this can in principle be achieved entirely by elastic collisions (including resonant elastic collisions in the hadronic phase such as $\pi + N \rightarrow \Delta \rightarrow \pi + N$) which do not change any of the particle abundances. Whether or not the microscopic interactions alter the chemical composition or leave it unchanged is, for this part of the discussion, entirely irrelevant.

This analysis of the spectral shapes has already taught us that hadrons are not formed right away but appear with some delay via the hadronization of a dense, thermalized, collectively expanding quark-gluon system. Let us now consider this hadronization process and ask how it affects the hadron abundances, i.e. the *chemical composition* of the hadronic system emerging from this process.

6.1 Statistical hadronization and the Maximum Entropy Principle

The microscopic description of the process in which thousand of quarks and gluons combine to form thousands of final state hadrons is clearly an impractical problem. But it is also not needed. A microscopic approach is asked for if we want to understand the (relatively rare) processes by which, say, a high- p_\perp hadron of a given flavor is created. Such particles probe the microscopic dynamics of high- p_\perp parton production, which is controlled by QCD, and although they may rescatter in the dense fireball medium they never completely lose their memory of the primary production process. We can exploit this and use them as “deep probes” for the fireball matter, but extracting the information on their production and subsequent medium modification then clearly requires a detailed microscopic treatment, including the hadronization of such hard partons. This is completely different for soft partons and hadrons: in their case the rescattering by the medium wipes out all memories about their initial production process, and there is no way their final momenta could ever be traced back to their initial momenta. This is in particular true for the hadronization process which is probably the most non-perturbative process imaginable: there are literally innumerable different microscopic channels which might lead to the production of, say, a negative pion with a soft momentum of order 300 MeV/c in the laboratory.

The proper approach to such a non-perturbative, multi-channel multi-particle problem is (as already recognized by Fermi, Landau and Hagedorn more than half a century ago) a statistical one. From a microscopic point of view, there is really very little information we can extract from the yields and momentum spectra of soft single hadrons. Due to the strong interactions among the quarks and gluons as they are forming hadrons, anything that is not explicitly forbidden by the conservation laws for energy, momentum, baryon number, electric charge, and net strangeness will in fact happen. (Net strangeness can

only be changed by weak interactions, on a time scale which is much too long compared to a heavy-ion collision.)

Note that such a statistical approach has, of course, its limitations: when we start to investigate correlations between pairs, triplets, quadruplets etc. of particles, at some level they will begin to realize that they all belong to a single heavy-ion collision event and are *not* produced entirely independently, but correlated in a non-statistical way. (For example, the momenta of all 2479 particles emerging from the collision have to add up to the total momentum of the initially colliding nuclei, and this is likely to generate non-statistical momentum correlations among considerably smaller subclusters of particles.) The statistical approach is certainly best justified for single-particle observables, such as hadron spectra and abundances.

These words are translated into equations via the Maximum Entropy Principle [140]: Let us consider the entropy \mathcal{S} of a small fluid cell of size ΔV in its own rest system,

$$\mathcal{S} = - \sum_k \int_{\Delta V} \int \frac{d^3x d^3p}{(2\pi)^3} \left[f_i \ln f_i + \vartheta_i (1 - \vartheta_i f_i) \ln (1 - \vartheta_i f_i) \right], \quad (83)$$

where the sum over i includes all particle species in the cell and $\vartheta_i = +1(-1)$ for fermions (bosons). We assume that soft hadronization happens through many different channels which are constrained only by the local (in ΔV) conservation laws for energy, baryon number and strangeness ($\int d\omega = \int_{\Delta V} \int \frac{d^3x d^3p}{(2\pi)^3}$):

$$\langle E \rangle = \int d\omega \sum_i E_i f_i, \quad \langle B \rangle = \int d\omega \sum_i B_i f_i, \quad \langle S \rangle = \int d\omega \sum_i S_i f_i = 0. \quad (84)$$

Here B_i and S_i are the baryon number and strangeness carried by each particle of species i , and we used that the net strangeness of the two colliding nuclei is zero and that strong interactions keep it that way *locally*. Maximizing \mathcal{S} with these constraints gives for the most likely distribution for particle species i [141]

$$f_i(E_i, \Delta V) = \frac{1}{e^{\beta(\Delta V)[E_i - \mu_i(\Delta V)] + \vartheta_i}} \quad \text{with} \quad \mu_i(\Delta V) = B_i \mu_B(\Delta V) + S_i \mu_S(\Delta V), \quad (85)$$

where β , μ_B and μ_S are Lagrange multipliers related to the values of the constraints (84) in ΔV . If the hadronization process does not change the number of $s\bar{s}$ pairs (for example, because strange valence quarks are too heavy), we should implement an additional constraint on the total number of strange quarks and antiquarks which fixes that number to the value before hadronization begins. In this case the expression for μ_i in (85) generalizes to $\mu_i = B_i \mu_B + S_i \mu_S + |s_i| \tilde{\mu}_s$ where $|s_i|$ is the total number of strange quarks and antiquarks in hadron i and $\tilde{\mu}_s$ is a further Lagrange multiplier related to this additional constraint. The associated *fugacity* $\gamma_s = e^{\beta \tilde{\mu}_s}$ is known as the “*strangeness saturation factor*” [142]. An under- resp. oversaturation of the strange particle phase space relative to its chemical equilibrium value corresponds to $\gamma_s < 1$ resp. $\gamma_s > 1$.

Equation (85) is a local thermal and chemical equilibrium distribution function. If the system could be kept at constant volume, any type of strong interaction among the hadrons would leave this distribution unchanged since such microscopic processes again conserve energy, baryon number and strangeness. However, the apparent “equilibrium” expressed by Eq. (85) is *not achieved kinetically* (i.e. as a result of hadronic rescattering) but *statistically* (by interference of many different hadron production channels). It does not require a thermalized prehadronic state (although *very* strong deviations from equilibrium, e.g. at high p_\perp , in the prehadronic state may survive the hadronization process and invalidate the Maximum Entropy Principle).

It is very important to realize that the same local equilibrium distribution (85) can be the result of two conceptually entirely different types of processes: we can either take system of hadrons with an arbitrary (except for the constraint on total energy, baryon number and strangeness) initial phase-space

distribution and let it evolve for a sufficiently long time to obtain Eq. (85) as a result of the action of elastic and inelastic processes among the hadrons. This is *kinetic equilibration*. Or we produce the system of hadrons of given energy, baryon number and strangeness from some non-hadronic state by a statistical process which fills hadronic phase-space in the statistically most probable configuration. This is *statistical equilibrium*. Both processes share the property that they lead to a state of Maximum Entropy. However, statistical hadronization can produce a Maximum Entropy distribution through non-hadronic processes which occur much faster than any inelastic scattering among hadrons at the given energy and baryon number density.

If you try to create, via statistical hadronization, a “pre-established equilibrium” distribution (85) of hadrons at energy density $e > e_{\text{cr}}$ ($T > T_{\text{cr}}$), lattice QCD tells us that such a “superheated” hadronic equilibrium configuration is unstable against deconfinement. If you leave this system to itself, the hadrons will dissolve again into quarks and gluons. Statistical hadronization thus can only proceed once the energy density has dropped to $e_{\text{had}} = e_{\text{cr}} \simeq 1 \text{ GeV/fm}^3$. Therefore the hadrons, when first formed from the hadronizing quark-gluon state, will have apparent chemical equilibrium abundances corresponding to a temperature $T_{\text{had}} = T_{\text{cr}}$.⁴ Before discussing what happens to this “chemical temperature” after hadronization has been completed, let us first have look at the data.

6.2 Hadrosynthesis at SPS and RHIC and pre-established hadronic chemical equilibrium

In Figure 29 I show the particle multiplicity ratios for stable (with respect to strong interactions) hadron emitted in Pb+Pb collisions at the SPS (left) and in Au+Au collisions at RHIC (right). In both cases the data have been fit to an “apparent chemical equilibrium distribution” (85); the resulting fit parameters are given in the Figure. The left panel presents the quality of the fit in a form introduced by Becattini

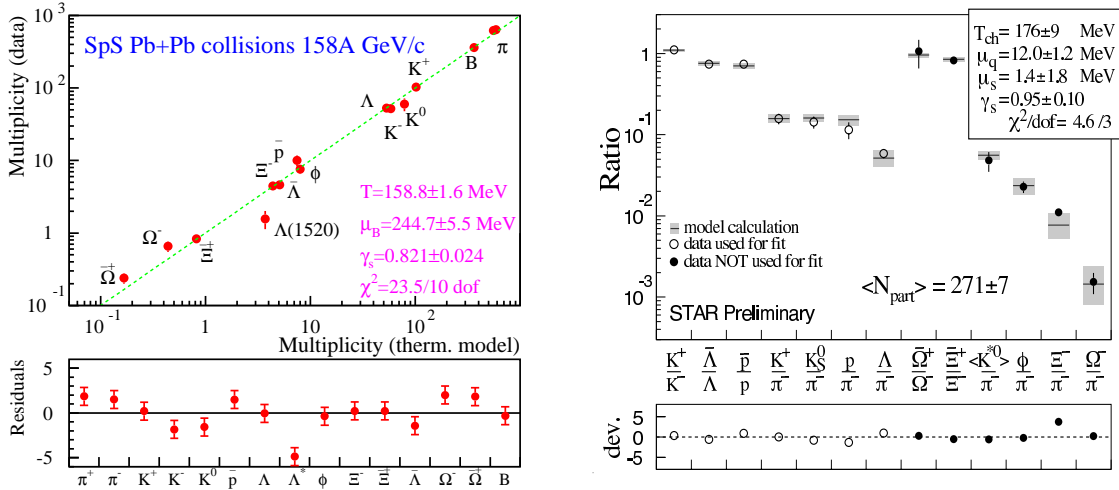


Fig. 29: Chemical equilibrium fits to the hadron abundances from Pb+Pb collisions at $\sqrt{s_{\text{NN}}} = 17 \text{ GeV}$ [54, 145] (left) and from Au+Au collisions at $\sqrt{s_{\text{NN}}} = 17 \text{ GeV}$ [68, 146]. The baryon chemical potential μ_B used on the left and the quark chemical potential μ_q used on the right are related by $\mu_B = 3\mu_q$. The strangeness chemical potential μ_s is not an independent fit parameter, but follows from overall strangeness neutrality. The strangeness saturation factor γ_s [142] is approximately 1 in both cases.

[144] where the measured multiplicities on the vertical axis are plotted against the multiplicities from the thermal model after optimization of the thermal parameters. If Eq. (85) gave a perfect description of the data, all points would lie exactly on the diagonal. For clarity the differences between data and

⁴I am not stating the same for the slope of their momentum distribution because the hadronizing quark-gluon matter already undergoes transverse flow which blueshifts the momentum spectrum. The abundances and the “chemical temperature” extracted from them are not affected by flow [143].

optimized thermal model are plotted (in terms of standard deviations) on a linear scale at the bottom. In the right panel the data are compared with bands of predicted ranges whose width is controlled by the statistical and systematic error of the thermal fit parameters [147]. Note that in the fit of the RHIC data only a fraction of the data was used for the fit while the rest (including ratios involving the rare doubly and triply strange Ξ and Ω hyperons) were successfully predicted by this fit.

These fits tell us several things. First, not surprisingly, the baryon chemical potential at RHIC is a lot smaller than at the SPS, due to increased transparency of the target nucleus for the incoming projectile baryons. Second, the value for the strangeness saturation factor γ_s is almost equal to 1 in both cases; I will return to this observation in the following subsection. Third, and most importantly, the “chemical decoupling temperature” T_{chem} is in both cases much higher than the kinetic freeze-out temperature T_{dec} extracted from the shape of the momentum spectra. At the SPS $T_{\text{chem}} \approx 160$ MeV and at RHIC $T_{\text{chem}} \approx 175$ MeV. Interpreting T_{chem} in the Maximum Entropy spirit as a Lagrange multiplier which tells us at which energy density statistical hadronization happened we see that the data correspond to energy densities which are very, very close to the critical energy density for deconfinement predicted by lattice QCD. According to lattice QCD, hadrons in thermodynamic equilibrium cannot exist at temperatures higher than about 175 MeV if $\mu_B = 0$, and this limit goes down if $\mu_B \neq 0$. So these chemical decoupling temperatures are about as high as they could possibly be for a system of hadrons!

Furthermore, we know from the spectra and elliptic flow that the fireball is collectively expanding and therefore undergoes rapid cooling. So we face the following conundrum: hadron formation is impossible at energy densities e corresponding to $T > T_{\text{chem}}$, but once the hadrons are formed at e_{cr} the system does not remain at this energy density but keeps diluting very rapidly. So if the hadrons first appeared with arbitrary abundances they would have had no time at all to adjust their abundances to chemical equilibrium values at $T_{\text{chem}} \approx T_{\text{cr}}$ by inelastic rescattering! The possibility that the measured chemical freeze-out temperature $T_{\text{chem}} \simeq 160 - 170$ MeV reflects a kinetically established chemical equilibrium is therefore logically excluded. The apparent chemical equilibrium at $T_{\text{chem}} \approx T_{\text{cr}}$ seen in the hadron abundances must thus be a “pre-established equilibrium” in the sense of statistical hadronization according to the Maximum Entropy Principle [15, 148].

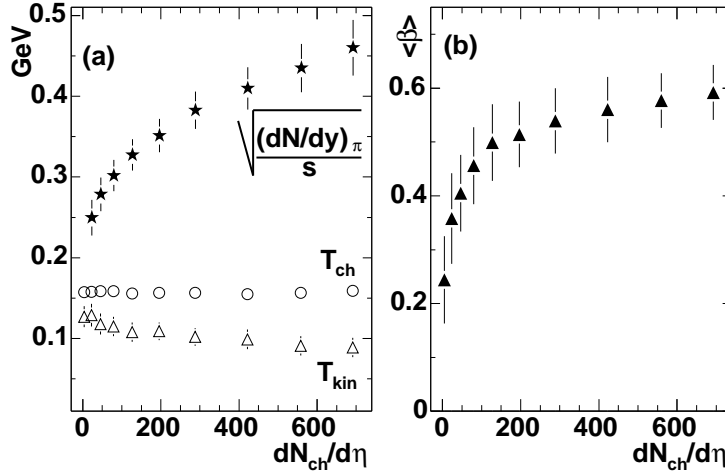


Fig. 30: (a) Pion multiplicity dN_π/dy per unit overlap area S (stars), chemical decoupling temperature T_{ch} (circles), thermal (kinetic) decoupling temperature T_{kin} (open triangles), and (b) the average transverse flow velocity $\langle \beta_T \rangle$ at kinetic decoupling as a function of collision centrality (measured by the total charged multiplicity pseudorapidity density $dN_{\text{ch}}/d\eta$ at midrapidity) from 200 A GeV Au+Au collisions at RHIC [150].

In addition to being *logically* excluded, there is also strong *empirical* evidence against a kinetic interpretation of the observed chemical decoupling temperature: First, it takes the same universal value of about 170 MeV in high energy e^+e^- [144], pp and $\bar{p}p$ [15], and nucleus-nucleus collisions [149].

Second, in Au+Au collisions at RHIC, T_{chem} is found to be independent of collision centrality (open circles in the left panel of Fig. 30), in contrast to the observed significant centrality dependence of the thermal decoupling temperature and average radial flow velocity extracted from the momentum spectra (triangles in Fig. 30 – see Fig. 9 for comparison and the discussion in Section 4.1.8). As discussed earlier, any kinetic decoupling process is a competition between local thermalization and global expansion rates. The latter depends on the size and lifetime of the collision fireball, as reflected by the clear dependence of the radial flow velocity on the impact parameter of the collision system in the right panel of Fig. 30. The larger fireballs formed in central collisions live longer, develop more radial flow and cool down to lower kinetic freeze-out temperatures than the smaller fireballs from more peripheral collisions. The chemical decoupling temperature T_{chem} , on the other hand, shows no dependence on the collision centrality (size of the fireball) at all; it can therefore not be controlled by a similar competition between scattering and expansion as seen in the kinetic decoupling temperature. **T_{chem} and T_{kin} rest conceptually on different footings.** T_{chem} is not a kinetic decoupling temperature, but a Lagrange multiplier in the Maximum Entropy framework whose value indicates the critical energy density at which hadrons are formed.

So if, as we concluded from the momentum spectra, after hadronization the system continues to expand and cool to lower temperatures, why doesn't the chemical decoupling temperature T_{chem} follow suit? The answer must be that, after being formed, the hadrons are unable to change their abundance ratios any further by inelastic rescattering. If this were not the correct interpretation, it would be very difficult to see how about a dozen different hadron species with abundances varying over 3 orders of magnitude could conspire to look like chemical equilibrium at $T \approx T_{\text{cr}}$. This would be an unlikely accident indeed. In Sec. 6.4 we will see theoretical arguments why chemical decoupling has to happen more or less directly at T_{cr} .

6.3 Strangeness enhancement

The fact that the chemical decoupling temperature has an uncanny resemblance with the predicted phase transition temperature is, in fact, only half the story. A similar picture of statistical hadronization at the critical energy density e_{cr} arises even from an analysis of e^+e^- , pp and $p\bar{p}$ collisions [15]. What is really dramatically different in heavy-ion collisions is the level of strangeness saturation reflected in the apparent chemical equilibrium state: The left panel of Fig. 31 shows that the overall fraction of strange particles is about twice as high in heavy-ion collisions as in elementary particle collisions! In other words, strangeness is suppressed relative to its chemical equilibrium saturation value in elementary particle collisions, but this strangeness suppression has disappeared in $A+A$ collisions. According to the preceding discussion this extra strangeness cannot have been produced by final state hadronic rescattering; it thus reflects the properties of the prehadronic state. This points to a new, fast strangeness production mechanism, either before or during hadronization. Rapid strangeness production from thermal gluons was predicted as one of the key characteristics of a QGP [16].

A large fraction of the strangeness suppression seen in elementary particle collisions can actually be understood within the statistical approach. Strong interactions conserve net strangeness *exactly*, i.e. $S = 0$ without any fluctuations. This means that in principle strangeness conservation should not be treated in the grand canonical ensemble as in Eqs. (84) and (85), where it is conserved only on average, but in the canonical ensemble where S is fixed exactly. In the infinite volume limit this makes no difference, but for the small “fireball” volumes created in elementary particle collisions it is a major correction. Strange hadrons get suppressed in this way since, together with the strange hadron, always a second hadron with balancing strangeness has to be created inside the same small volume at the same time, and this requires more energy. However, even if this canonical effect were the complete explanation of the suppression in e^+e^- and pp collisions (which seems quantitatively unlikely [152]), the disappearance of the effect in heavy-ion collisions would still be most interesting: The absence of canonical strangeness suppression in nuclear collisions tells us that creation of a strange hadron at a given position

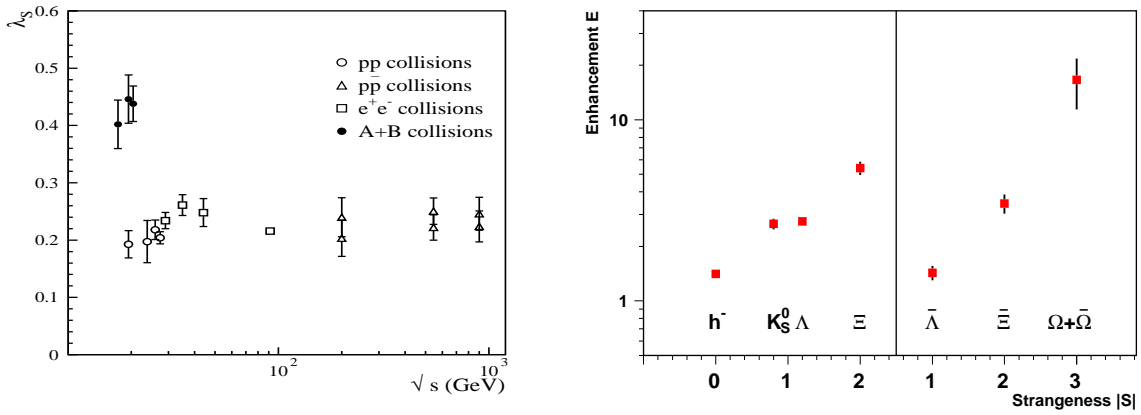


Fig. 31: Left: The strangeness suppression factor of produced strange vs. nonstrange quarks, $\lambda_s = 2 \langle \bar{s}s \rangle / \langle \bar{u}u + \bar{d}d \rangle|_{\text{produced}}$, in elementary particle and heavy-ion collisions as a function of \sqrt{s} [145]. The two points each for $p\bar{p}$ collisions reflect the inclusion (exclusion) of the initial valence quarks. Right: Enhancement factor for the midrapidity yields per participating nucleon in 158 A GeV/c Pb+Pb relative to p+Pb collisions for various strange and non-strange hadron species [151].

in the fireball does not require the production of a particle with balancing strangeness nearby (as in pp), but strangeness can be balanced by production of an anti-strange hadron on the other side of the nuclear fireball! Now we know that all microscopic QCD processes which create $s\bar{s}$ pairs are local processes, i.e. the pairs are created at the same point. If the final strange hadron abundances don't know about this anymore, but behave as if the strange and antistrange hadrons were created independently and statistically distributed over the entire nuclear fireball, the necessary implication is that they have lost their memory of the locality of the primary QCD process from which they came and have been able to communicate over macroscopic fireball distances. I cannot imagine how this is possible without a significant amount of strangeness diffusion *before* hadronization.

A very striking way of plotting the “strangeness unsuppression” is shown in the right panel of Fig. 31 [151]: relative to p +Pb collisions, the number of produced strange hadrons per participating nucleon is the more strongly enhanced the more strange (anti)quarks for its formation are required. For Ω and $\bar{\Omega}$ this enhancement factor is about 15! The tendency shown in Fig. 31 is completely counterintuitive for hadronic rescattering mechanisms, where multistrange (anti)baryons are suppressed by higher thresholds than kaons and Λ 's; but it is perfectly consistent with a statistical hadronization picture [153] where multi-strange particles profit more from the global strangeness enhancement than singly strange hadrons.

6.4 Chemical kinetics after hadronization

The kinetic freeze-out temperatures of about 120 MeV extracted from the hadron momentum spectra tell us that after hadronization at $T_{\text{cr}} \approx 170$ MeV the hadrons continue to rescatter for quite a while. This rescattering can be simulated in a hadronic cascade such as URQMD [154], using everything that is known about hadron masses and cross sections from the Particle Data Tables. These tables tell us that hadron cross sections are strongly dominated by resonances at well-defined collision energies, for example $\pi + N \rightarrow \Delta \rightarrow \pi + N$, $\pi + \pi \rightarrow \rho \rightarrow \pi + \pi$, $\pi + K \rightarrow K^* \rightarrow \pi + K$, etc. These resonances have large cross sections, hence these types of collisions happen frequently and are able to keep up with the collective expansion of the fireball by continually re-equilibrating the hadron momentum distributions to the falling temperature. However, almost all of these resonances have the tendency to decay again into exactly the same hadrons from which they were created (up to charge exchange). The cross sections for strangeness exchange processes are considerably smaller, and even smaller are inelastic hadronic processes which create or annihilate strange quark-antiquark pairs. The resonant collisions thus do not

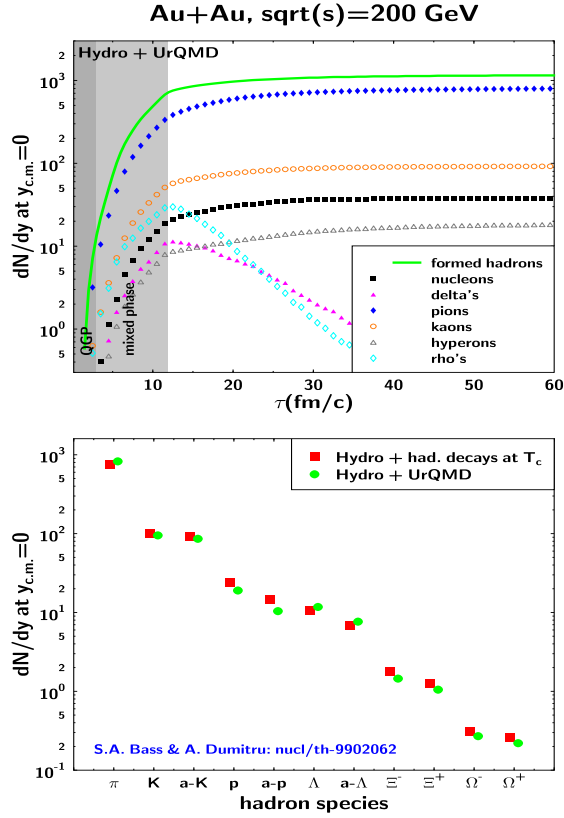


Fig. 32: Time-dependence of the chemical composition of an expanding hadronic fireball which was initialized at T_{cr} with chemical equilibrium abundances [154]. Unstable hadrons are seen to decay as stable hadrons approach their asymptotic abundances (top). In the bottom panel, the squares indicate the initial chemical equilibrium yields for stable hadrons, after taking into account feeddown from unstable resonance decays, whereas the circles indicate the final stable hadron yields including hadronic rescattering.

modify the total measured yields of pions, kaons, and nucleons. For example the total pion number

$$N_{\pi}^{\text{total}} = N_{\pi} + 2N_{\rho} + N_{\Delta} + N_{K^*} + \dots \quad (86)$$

is frozen in at T_{cr} , and similarly for other stable hadrons. This is seen in the bottom part of Fig. 32 which shows that, if URQMD is initialized with thermodynamic equilibrium abundances and a hydrodynamical generated transverse flow profile similar to the discussion in Sec. 4, the stable particle yields hardly change if they are calculated directly at T_{cr} by simply letting all unstable resonances decay, but switching off all collisions, or if they are calculated at the end of the entire hadronic cascade.

Looking a bit more carefully at the bottom part of Fig. 32 we see that URQMD tends to lose predominantly (anti)baryons (and thus a fraction of the initial enhancement of multi-strange (anti)baryons) by baryon-antibaryon annihilation during the rescattering stage. It was recently shown [155] that this is to a large extent a manifestation of the lack of detailed balance in the codes which include processes like $\bar{p}p \rightarrow n\pi$ (with $n = 5 - 6$) but not their inverse. Rapp and Shuryak [155] argue that, as the system cools below T_{chem} , pions and kaons don't annihilate but instead build up a positive chemical potential which enhances the probability for the inverse reaction and strongly reduces the net annihilation of antibaryons. This is really fortunate, because it is this lack of abundance-changing processes during the hadronic expansion stage which allows us to glimpse the hadronization process itself through the final hadronic abundances, in spite of intense, resonance-mediated *elastic* rescattering among the hadrons between hadronization at $T_{chem} \approx 170$ MeV and kinetic freeze-out at $T_f \approx 120$ MeV.

Of course, the abundances of unstable resonances are *not* frozen in at T_{cr} (see top panel of Fig. 32): Due to their strong coupling to the cooling pion fluid (to which cooling they actively contribute), their abundances readjust to the decreasing temperature. Note, however, that their abundances don't fall with the usual free-space exponential decay law, but more slowly since they keep being recreated by resonant hadronic interactions. But as the temperature drops, their abundances decrease. Detailed balance dictates that, the larger their pionic decay width, the later the resonance yields decouple and the smaller a temperature their decoupling abundances reflect. If we can reconstruct the resonances from their decay

products we therefore expect resonance yields which are smaller than predicted from the thermal fit of the stable hadron yields:

$$\left(\frac{K^*}{K}\right)_{\text{meas}} < \left(\frac{K^*}{K}\right)_{T_{\text{rmchem}}} \quad \text{etc.} \quad (87)$$

Such studies are presently under way.

6.5 Primordial hadrosynthesis: measuring the critical temperature for deconfinement

We can summarize our insights gained in this chapter by stating as our **Fourth Lesson**: The hadron abundances “freeze out” directly at hadronization. What we see in the SPS and RHIC data are hadron abundances established during *primordial hadrosynthesis* via a statistical hadronization process. The measured abundance ratios give for the hadronization temperature $T_{\text{had}} \approx T_{\text{cr}} \approx 170$ MeV, confirming predictions from lattice QCD. The QCD phase transition temperature has thus been measured. This measurement was possible because at SPS and RHIC the fireball expands so rapidly that in the late hadronic rescattering stage no inelastic chemical processes happen anymore. In this way the hadron abundances open a window onto the hadronization phase transition even though their momentum distributions continue to change and cool for several more fm/c.

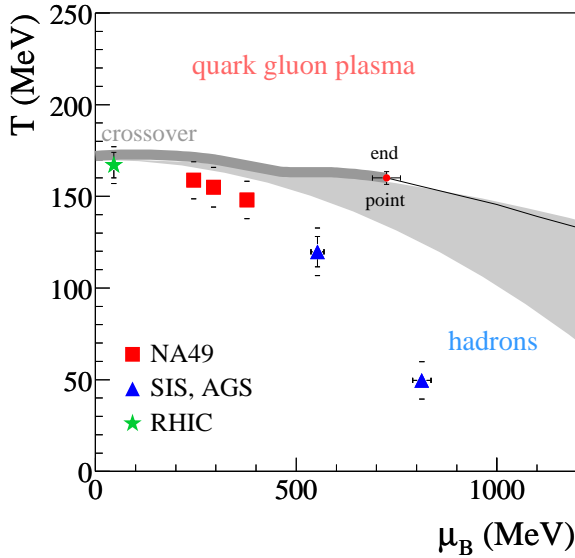


Fig. 33: QCD phase diagram with chemical freeze-out points extracted from hadron abundance ratios from heavy ion ($A \simeq 200$) collisions at center of mass energies $\sqrt{s_{\text{NN}}}$ ranging from 2.4 to 200 GeV [54]. The curve and shaded region indicate estimates for the deconfinement phase transition at finite baryon chemical potential μ_B from recent lattice QCD calculations [2, 156]. The critical endpoint where the transition changes from first order (high μ_B) to continuous crossover (low μ_B) is also indicated (although for unrealistically large quark masses [2]). Figure taken from Ref. [54].

Figure 33 shows the chemical freeze-out points extracted from hadron yields in $A+A$ collisions with $A \simeq 200$, compiled for heavy-ion fixed-target and collider experiments from $\sqrt{s_{\text{NN}}} \approx 2.4$ GeV (SIS) to $\sqrt{s_{\text{NN}}} \approx 200$ GeV (RHIC), and compares them to the latest estimates for the hadronization phase transition from lattice QCD [2, 156]. While for the SPS and RHIC the chemical decoupling temperatures are consistent with the predicted hadronization temperatures, the values extracted at the Brookhaven AGS and in particular at the SIS at GSI lie considerably below the phase transition. In these cases statistical hadronization can not explain the values for T_{chem} . It is likely that, due to the larger net baryon densities in lower-energy heavy-ion collisions, inelastic hadronic rescattering processes happen faster than at higher energies and are able to lead to kinetic readjustment of the chemical temperature below T_{cr} . One should also note, however, that the “quality” of the apparent chemical equilibrium seen at the AGS and SIS is not as good as at the higher energies since many of the heavier hadrons (in particular the strange and multistrange antibaryons) are too rare to be measured reliably. The data points labelled by “SIS,AGS” in Figure 33 thus comprise a much smaller number of measured hadron yields, in particular in the strange sector where only K , \bar{K} , Λ and φ are available at these energies.

7 PARTON ENERGY LOSS AND JET QUENCHING

In Section 4 we saw that in Au+Au collisions at RHIC the soft momentum particles with $p_{\perp} \lesssim 2 \text{ GeV}/c$ behave hydrodynamically. For larger p_{\perp} the hydrodynamic description gradually breaks down. We saw this in Sec. 4.2 when discussing the elliptic flow and how it breaks away from the hydrodynamically predicted increase with p_{\perp} above $p_{\perp} \simeq 2 \text{ GeV}/c$. In the single particle spectra the transition from collective

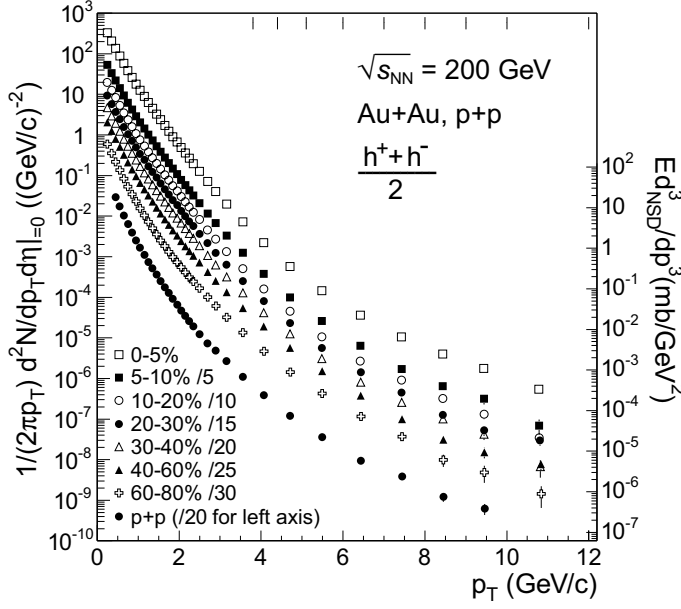


Fig. 34: Charged hadron transverse momentum spectra in p+p and Au+Au collisions at $\sqrt{s_{NN}} = 200 \text{ GeV}$ [157]. The Au+Au data are binned in different centrality classes as indicated. For central and semicentral Au+Au collisions, note the transition from an exponential behaviour at $p_{\perp} \lesssim 2 \text{ GeV}/c$ to a power law for $p_{\perp} > 4 \text{ GeV}/c$.

hydrodynamic behaviour to hard scattering manifests itself by a change of shape: above $p_{\perp} \gtrsim 3-4 \text{ GeV}/c$ the spectra change from a thermal exponential shape to a power law as predicted by perturbative QCD. Figure 34 shows this for Au+Au collisions at RHIC, together with a comparison spectrum from p+p collisions. This power law affects fewer than 0.1% of all produced hadrons, but it is these rare high- p_{\perp} hadrons on which we will focus our attention in this section.

These high- p_{\perp} hadrons stem from the fragmentation of even-higher- p_{\perp} partons which, as noted in Sec. 3.1, are created very early in the collision, at $\tau_{\text{form}} \simeq 1/p_{\perp}$. On their way out of the evolving collision fireball they interact with the hot matter and probe its properties (density, opacity, etc.). In this respect they are very similar to positrons in PET (= Positron Emission Tomography) where one injects a positron-emitting source into some living organ and then explores properties of that organ by detecting these positrons and their energies outside the body. Measuring the properties of hard hadrons emitted from a relativistic heavy-ion collisions thus corresponds to Parton Emission Tomography, but since this would have the same acronym which might lead to all kinds of confusion, and since we don't really detect partons but rather their hadronic fragments which form a jet, I follow M. Gyulassy [158] and call this method **JET** (for **Jet Emission Tomography**).

7.1 Radiative energy loss of a fast parton

The idea of jet quenching by parton energy loss goes back to an unpublished preprint by J.D. Bjorken in 1982 [159], but he incorrectly identified elastic parton scattering as the dominant medium interaction by which the fast parton loses energy. The correct mechanism, namely induced gluon bremsstrahlung, was identified by Gyulassy and collaborators [160] and first fully evaluated by Baier, Dokshitzer, Mueller, Peigné, and Schiff [161]. Its quantitative effect on the energy loss has now been calculated by several groups under various approximations (see [162] for a recent review).

In QCD the dominant process by which a fast parton with $E_{\text{parton}} \gg 1 \text{ GeV}$ loses energy is by induced gluon radiation, see Fig. 35. The color charge of the fast parton (which could be a quark or a gluon)

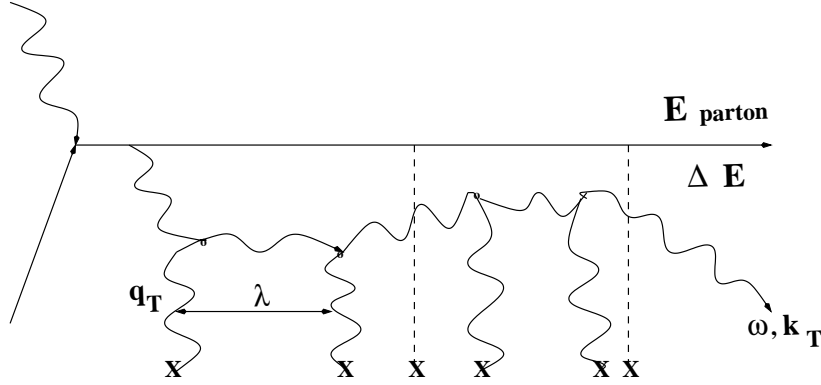


Fig. 35: Typical gluon radiation diagram (from [162]).

interacts with the color charges of the medium (which can be modeled as static external charges since their motion can be neglected relative to that of the fast particle) and, as a result, emits a bremsstrahlung gluon. What makes things different from and more complicated than the analogous process in QED is the fact that the emitted gluon itself carries color charge and again interacts with the color charges in the medium (see Fig. 35), and that all these medium interactions must be added up coherently. In contrast to the fast particle, whose trajectory can be taken as a straight line, the reinteractions of the much softer emitted gluon with the medium induce a random walk in its transverse momentum k_T . The reinteractions of the emitted gluon with the medium are characterized by a mean free path λ_g , also indicated in the Figure.

In the limit $E_{\text{parton}} \rightarrow \infty$ and for a thick target, $L \gg \lambda_g$, BDMS [161] found for the energy loss

$$\Delta E_{\text{BDMS}} = \frac{C_R \alpha_s}{4} \frac{\mu^2}{\lambda_g} L^2 \tilde{v} \quad (88)$$

where C_R is the color Casimir eigenvalue of the fast parton ($= N_c$ for gluons), μ is the color Debye screening length of the medium (controlled by its density), and $\tilde{v} \sim 1-3$ is a factor which depends logarithmically on the thickness L of the medium and the gluon mean free path, $\tilde{v} \sim \ln(L/\lambda_g)$. The ratio

$$q \simeq \frac{\mu^2}{\lambda_g} \simeq \rho \int d^2 q_\perp q_\perp^2 \frac{d\sigma}{d^2 q_\perp} \propto \alpha_s^2 \rho \quad (89)$$

plays the role of a momentum transport coefficient of the medium and exhibits the explicit dependence of the energy loss on the density ρ of the medium. The non-Abelian nature of QCD reflects itself in the characteristic *non-linear* dependence of the energy loss (88) on the thickness L of the medium. The extra factor of L compared to the naive expectation arises from the random walk in k_T of the emitted gluon which increases its probability to separate itself (decohere) from the fast parton linearly with L .

The asymptotic expression (88) was improved for “thin” plasmas and finite energy kinematic effects by Gyulassy, Levai and Vitev (GLV) [163] by use of an expansion in powers of the “opacity” of the medium (i.e. the integral over density times cross section along the path of the fast parton, $\bar{n} = L/\lambda_g$). Their leading order contribution, which strongly dominates the energy loss, is

$$\Delta E_{\text{GLV}}^{(1)} = \frac{C_R \alpha_s}{N(E)} \frac{\mu^2}{\lambda_g} L^2 \ln \frac{E}{\mu}. \quad (90)$$

While the characteristic quadratic L dependence of Eq. (88) is not altered by keeping only the first term in the opacity expansion, the dependence of the energy loss on the parton energy $E = E_{\text{parton}}$ is quite different, due to the factor $N(E)$ in the denominator. For $E \rightarrow \infty$ this factor approaches the BDMS

value, $N(E) \rightarrow 4$, but as the parton energy E decreases $N(E)$ increases rapidly, suppressing energy loss for low- E partons. In the range $2 \text{ GeV} \leq E \leq 10 \text{ GeV}$, for fixed L the fractional energy loss $\Delta E_{\text{GLV}}^{(1)}/E$ is almost constant [164].

7.2 Soft vs. hard particle production

According to QCD and asymptotic freedom, the production of high- p_{\perp} partons can be calculated perturbatively and is proportional to the number of binary nucleon-nucleon collisions which for a nucleus-nucleus collision $A+B$ at impact parameter b is given by

$$N_{\text{coll}}(b) = \sigma_0 \int dx dy T_A(x+b/2, y) \cdot T_B(x-b/2, y). \quad (91)$$

Here σ_0 is the total inelastic nucleon-nucleon cross section, the integral is over the transverse plane, and $T_A(x, y) = \int \rho_A(x, y, z) dz$ is the nuclear thickness function of a nucleus of mass A with density profile ρ_A . The impact parameter b can be estimated from the total charge multiplicity, by equating equal fractions of the total multiplicity divided by the maximum multiplicity measured in the most central collisions with the corresponding fractions of the total cross section, calculated geometrically as a function of b [165]. Due to the fact that for fixed impact parameter B the number of produced hadrons fluctuates, this determination of b from dN_{ch}/dy is uncertain by a fraction of 1 fm, which induces a corresponding uncertainty in the relation between N_{coll} and dN_{ch}/dy [165].

The argument that hard particle production should scale $\sim N_{\text{coll}}$ exploits the fact that hard particles are produced on short time scales $\tau \sim 1/p_{\perp}$, and that hard particle production on successive nucleons in the nucleus therefore happens incoherently. The same is not true for soft hadron production which involves the coherent scattering of a projectile nucleon with several target nucleons, due to the Landau-Pomeranchuk-Migdal (LPM) effect of a finite formation (or “decoherence”) time (see the last paper in [160] for an explanation of the LPM effect). The net result of the LPM effect is a reduction of soft particle production by destructive interference, resulting in its phenomenologically observed approximate scaling with the number N_{part} of participating (or “wounded”) nucleons: each struck nucleon contributes only once to soft particle production, and suffering more than one collision in sequence does not increase the soft particle yield. The number N_{part} of wounded nucleons can again be calculated geometrically, by a formula similar to Eq. (91) but involving the sum of the nuclear thickness functions instead of their product (see e.g. Ref. [63]).

7.3 Suppression of high- p_{\perp} hadrons in central Au+Au collisions at RHIC

In the 5% most central Au+Au collisions at $\sqrt{s_{\text{NN}}} = 200 \text{ GeV}$ at RHIC, the average number of participating nucleons is $\langle N_{\text{part}} \rangle = 344$ (i.e. 172 times higher than in a p+p collision) whereas the number of binary nucleon-nucleon collisions is $\langle N_{\text{coll}} \rangle = 1074$ (i.e. 1074 times higher than in a p+p collision) [165]. The difference between “participant scaling” (expected for soft particles) and “binary collision scaling” (expected for hard processes) is in this case a factor of $1074/172 = 6.2$. The “nuclear modification factor”

$$R_{AA} = \frac{1}{N_{\text{coll}}^{AA}} \frac{dN^{AA}/dy dp_{\perp}}{dN^{pp}/dy dp_{\perp}} \quad (92)$$

for $A = 197$ (gold) should therefore be $R_{AA} = 1$ for particles whose production scales with N_{coll} , and $R_{AA} \simeq 0.16$ for particles whose production scales with N_{part} . Hence, as a function of increasing p_{\perp} , we should expect R_{AA} to rise from a value near 1/6 at low p_{\perp} to about 1 at high p_{\perp} .

However, it has been known for over 25 years from minimum bias p+A collisions at Fermilab [166] that R_{AA} reaches values even larger than 1 at $p_{\perp} \gtrsim 2 \text{ GeV}/c$. The explanation of this “Cronin effect” goes as follows: At high transverse momenta the p_{\perp} -spectrum of hadrons produced in p+A is not only shifted *up* in normalization by a factor $N_{\text{coll}} \simeq A$ as appropriate for a hard scattering process,

but on top of this also *horizontally* towards higher p_\perp (which at fixed p_\perp , of course, manifests itself as an additional gain, due to the falling nature of the p_\perp -spectrum). The horizontal shift towards larger p_\perp arises from the fact that the partons inside the projectile nucleon, before making the hard collision which ends up producing the measured high- p_\perp hadron, already suffer multiple elastic collisions with other target nucleons which they encounter first, thereby acquiring transverse momentum k_\perp which grows in a random walk with the square root of the number of these elastic collisions. Once the hard inelastic collision happens, the projectile parton already brings in this “initial k_\perp ”, thereby giving an extra k_\perp kick to the produced hard parton. Since this extra k_\perp is a decreasing fraction of the observed p_\perp as p_\perp becomes larger, the Cronin enhancement should disappear as $p_\perp \rightarrow \infty$. (For the same reason the Cronin effect should become weaker as $\sqrt{s_{NN}}$ increases.) Hence, for large p_\perp , R_{AA} should indeed approach the value 1, but not from *below* due to soft scaling at low p_\perp , but rather from *above* due to Cronin enhancement at intermediate p_\perp [167]. This behavior is seen in the two top curves (labelled “no dE/dx ”) in the right part of Fig. 36.

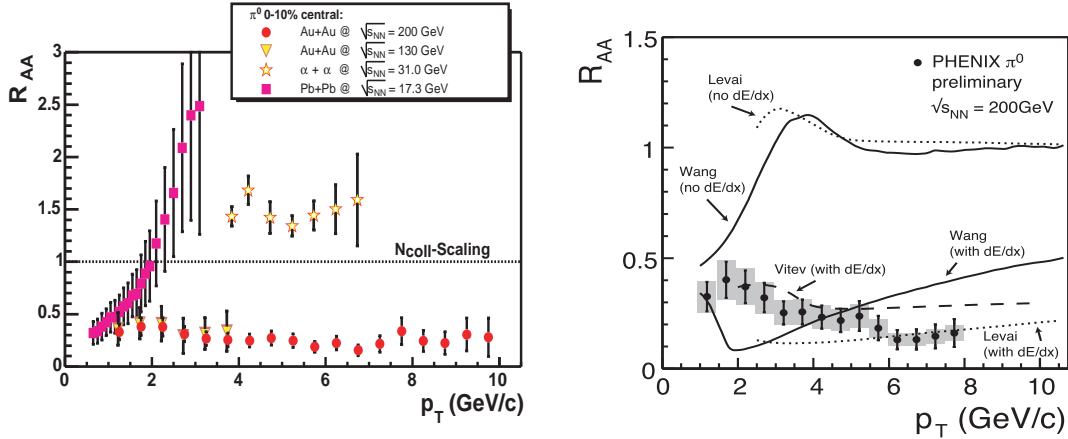


Fig. 36: Left: The nuclear modification ratio R_{AA} defined in Eq. (92) for neutral pions measured in $\alpha + \alpha$ collisions at the ISR [168], in Pb+Pb collisions at the SPS [169], and in Au+Au collisions at RHIC [170, 171]. (Figure taken from Ref. [172].) Right: R_{AA} for π^0 in central Au+Au collisions at RHIC [170] together with theoretical calculations [164, 167, 173]. (Figure taken from Ref. [174].)

The left panel of Figure 36 shows the measured nuclear modification factor for neutral pion production in Pb+Pb collisions at the SPS and in Au+Au collisions at RHIC. For comparison also results from $\alpha + \alpha$ collisions at the ISR in the range $4 \text{ GeV}/c \leq p_\perp \leq 7 \text{ GeV}/c$ are included which exhibit the Cronin effect in this p_\perp region. The Pb+Pb data at $\sqrt{s_{NN}} = 17 \text{ GeV}$ show a dramatic growth of R_{AA} with increasing p_\perp , starting from participant scaling at low p_\perp but then exceeding the binary collision limit and exhibiting a strong Cronin enhancement above $p_\perp \gtrsim 2 \text{ GeV}/c$. (This Cronin effect is larger than in the ISR data, due to both the larger collision system, implying a larger initial k_\perp , and the lower center of mass energy.)

In stark contrast, the RHIC Au+Au data at both 130 and 200 GeV c.m. energy hardly rise at all above the participant scaling level. With some good will $R_{AA}^{\pi^0}$ is seen to feature a small peak around $p_\perp \simeq 2 \text{ GeV}$, but at a level of less than 50% of the binary collision limit. At higher p_\perp , instead of increasing towards 1, R_{AA} decreases again towards a value of about 0.2. No sign of the Cronin effect and of binary collision scaling anywhere! If we jump ahead to Fig. 37 which shows in the lower parts of both panels (labelled by “Au+Au”) the p_\perp -dependence of R_{AA} for all charged particles, and if we assume that charged and neutral pions (triangles in the left panel) have the same nuclear modification factor, we see that R_{AA} for heavier charged hadrons must be larger than for pions in the region $1 \text{ GeV}/c \lesssim p_\perp \lesssim 4 \text{ GeV}/c$, but also drop back to well below 1 for $p_\perp \gtrsim 4\text{--}5 \text{ GeV}/c$.

The conclusion we must draw from these data is that in central Au+Au collisions at RHIC high- p_\perp hadron production is suppressed by at least a factor 5 compared to the perturbative QCD prediction of

binary collision scaling plus Cronin effect (top curves in the right panel of Fig. 36). In fact, looking at various collision centralities in Au+Au collisions, it was shown explicitly by the PHOBOS Collaboration [175] that above $p_{\perp} \gtrsim 4$ GeV the charged hadron spectra scale again linearly with N_{part} (i.e. like a soft process), instead of scaling with N_{coll} as expected for a hard process. Furthermore, a crucial control experiment has recently been completed where the nuclear modification factor was measured in d+Au collisions (top parts of Fig. 37). One sees that in deuteron-gold collisions $R_{AA} = R_{dAu}$ increases from

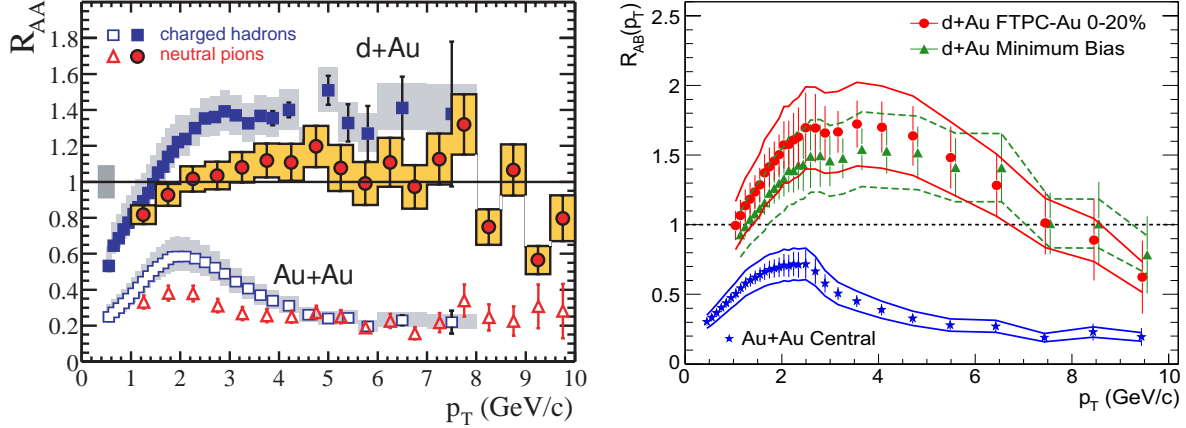


Fig. 37: The nuclear modification ratio R_{AA} for neutral pions (left) and charged hadrons (left and right), measured in d+Au and central Au+Au collisions at $\sqrt{s_{NN}} = 200$ GeV, by PHENIX [176] (left) and by STAR [177] (right). At intermediate p_{\perp} , $1.5 \text{ GeV}/c < p_{\perp} < 4 \text{ GeV}/c$, the R_{AA} is systematically larger for charged particles than for π^0 , indicating a larger R_{AA} for kaons and protons than for pions in this p_{\perp} -range.

participant scaling at low p_{\perp} to above 1 at $p_{\perp} \simeq 1.5 \text{ GeV}/c$ and shows the expected Cronin enhancement (rather than a suppression) which persists at least up to $p_{\perp} = 8 \text{ GeV}/c$. Again all charged particles taken together (which includes heavier hadrons such as kaons and protons) show a larger Cronin enhancement than pions alone (left panel in Fig. 37), and in central d+Au collisions the Cronin effect is a bit larger than in minimum bias collisions (right panel in Fig. 37), as expected from the random walk argument for the initial k_{\perp} .

So the suppression of high- p_{\perp} hadrons in central Au+Au collisions must be a final state effect which involves the dense matter created in the heavy-ion collision. It can not be explained as an initial state effect, i.e. by some property of the internal structure of the gold nucleus which shows up when probing it at high energies (such as the existence of a “color glass condensate”, see the short discussion in Sec. 3.4 and the recent review [28]): such an effect should still be visible (i.e. some suppression should persist) if only one of the colliding nuclei is gold [178].

The right panel in Figure 36 shows that only theories which include an energy loss dE/dx for the fast partons that produce the high- p_{\perp} hadrons can account for the R_{AA} data at RHIC. Although the different theoretical predictions shown in the graph, which use different approximations for the implementation of the radiative energy loss, give somewhat different p_{\perp} -dependences of R_{AA} and do not agree perfectly with the data, it is obvious that a significant amount of energy loss is required to account for the observed suppression by more than a factor 5 relative to the expected binary collision scaling plus Cronin (upper curves).

The observed scaling with N_{part} instead of N_{coll} suggests a very interesting geometric interpretation: Due to the approximately constant density inside an atomic nucleus, the number of participating nucleons is proportional to the volume of nuclear matter affected by the collision, $N_{\text{part}} \propto V_{\text{fireball}}^{\text{init}}$. The number of binary collisions scales very accurately as $N_{\text{coll}} \propto N_{\text{part}}^{4/3}$. So the difference between participant and binary collision scaling is a factor $N_{\text{part}}^{-1/3} \propto V_{\text{fireball}}^{-1/3} \propto 1/R_{\text{fireball}}$, i.e. a surface/volume ratio: the high- p_{\perp} hadron production data in central Au+Au collisions at RHIC are consistent with the sim-

ple hypothesis that high- p_{\perp} hadrons are only emitted from the surface, but not from the interior of the fireball! Now why should this be the case?

7.4 Jet quenching in central Au+Au collisions at RHIC — “JET of the QGP”

Experiments provide a unique answer also to this question [179]: Jets from partons which have to travel a significant distance through the dense fireball matter formed in the collision lose so much energy that they are no longer recognizable as jets and become part of the hot matter of soft particles. To show this experimentally one must first find jets. This is not easy due to the huge number of soft hadrons with $p_{\perp} < 2$ GeV which contribute so much transverse energy that the usual method of finding a spike in E_T in a certain small bin of solid angle fails. Another method for finding jets does work, however: One triggers on a fast particle (say, with $4 < p_{\perp} < 6$ GeV/c [179]) and then looks for azimuthal angular correlations with other, not too soft hadrons (say, with $p_{\perp} > 2$ GeV/c, in order to remove most of the background from uncorrelated soft hadrons). Since fast partons fragment into a jet of hadrons pointing within a relatively narrow angular cone (“jet cone”), jets manifest themselves by positive angular correlations at small angles relative to the fast trigger particle. This is shown in Fig. 38 where it gives rise to the peak at $\Delta\varphi = 0$.

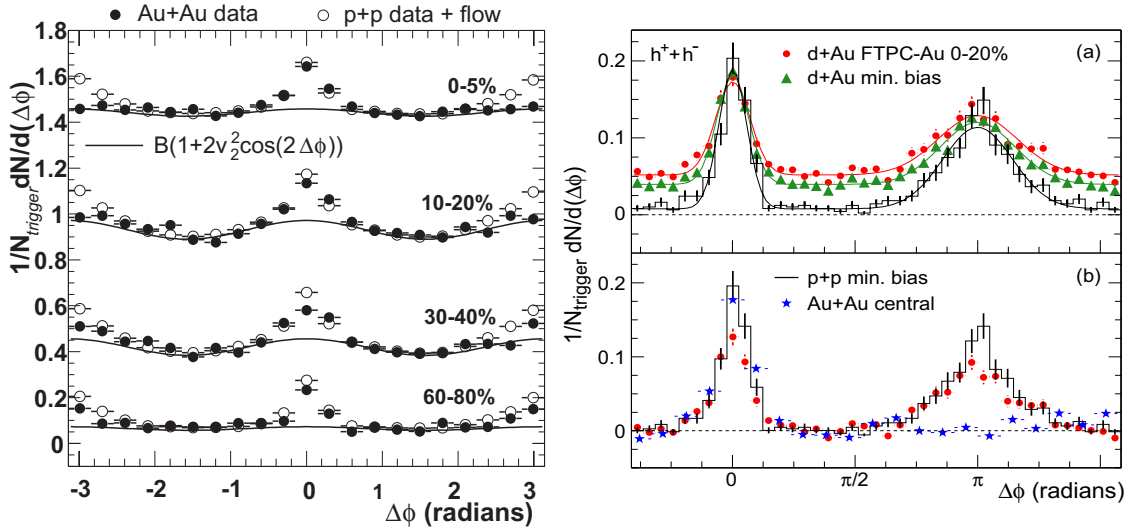


Fig. 38: Jet suppression in central Au+Au collisions at $\sqrt{s_{NN}} = 200$ GeV at RHIC. Left: Azimuthal angular correlations in Au+Au collisions, in four centrality bins, compared with properly scaled p+p data to which the effect of elliptic flow v_2 measured in the same p_{\perp} - and centrality window has been added. (For details see Ref. [179].) Whereas such a superposition of p+p data and elliptic flow can reproduce the peripheral (60-80%) Au+Au data, it overpredicts the far-side correlations at $\Delta\varphi = \pi$ for semicentral and central collisions. Right: Azimuthal angular correlations in p+p as well as min. bias and central d+Au collisions (upper diagram), and in p+p, central d+Au and central Au+Au collisions (lower diagram) [177]. For details about the subtraction procedure in the bottom part see the original paper [177].

In perturbative QCD, hard partons are produced in pairs with 180° opening angle in the pair center of mass frame. This leads to a second azimuthal angular correlation peak at $\Delta\varphi = \pi$. The solid histogram in the right panel of Fig. 38 shows this for p+p collisions at $\sqrt{s_{NN}} = 200$ GeV [177]. The “far-side” peak is flatter and wider than the “near-side” peak, due to well-understood trigger effects and a non-zero probability for semihard gluon emission by one of the two fast partons. Except for a somewhat higher background from uncorrelated pairs due to increased soft particle production (“pedestal effect”), the same pattern is seen in minimum bias and central d+Au collisions (Fig. 38, upper part of the right panel).

However, as one goes to Au+Au collisions and moves from peripheral to central collisions (bottom to top in the left panel of Fig. 38), the away-side peak at $\Delta\varphi = \pi$ disappears. Whatever enhanced angular correlation survives in almost central Au+Au collisions at $\Delta\varphi = \pi$ is perfectly compatible with the measured elliptic collective flow v_2 in the p_\perp -range where the angular correlations are measured [179]. Whereas the far-side jet correlations should be localized in a narrow window of relative pseudorapidity $\Delta\eta$ between the correlated particles, elliptic flow is a global collective effect which is correlated with the reaction plane and therefore present at both small and large relative pseudorapidity. By subtracting the correlations for pairs with $\Delta\eta > 0.5$ from those for pairs with $\Delta\eta < 0.5$ one in fact completely removes the elliptic flow contribution [179]. For semicentral Au+Au collisions the result of this procedure is a strongly reduced far-side angular correlation peak, and in central Au+Au collisions it is *completely absent* (lower diagram in the right panel of Fig. 38)!

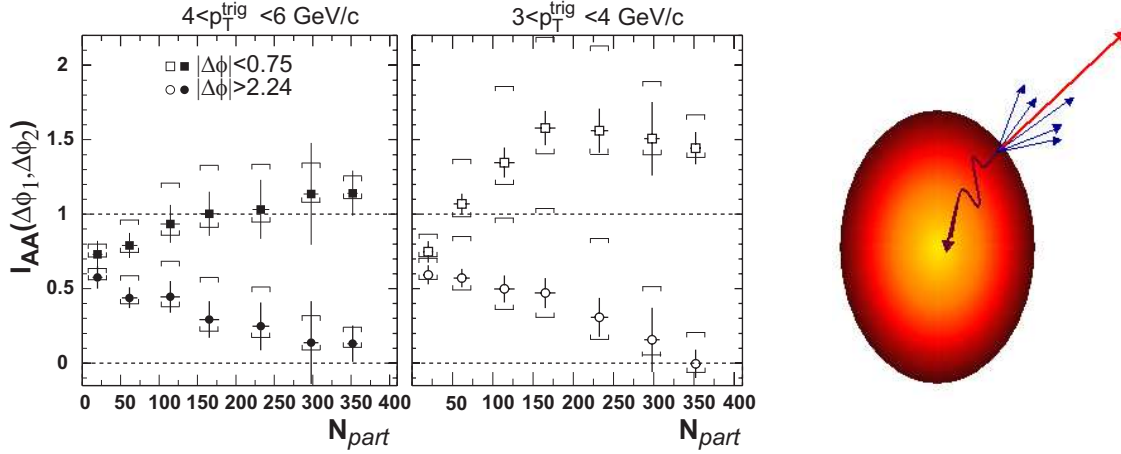


Fig. 39: Left: Suppression of near-side (squares) and far-side angular correlations (circles) in Au+Au collisions at RHIC, for two different lower p_\perp cuts for the trigger particle [179]. Note the disappearance of the far-side correlations in central collisions (i.e. for large numbers N_{part} of participating nucleons). Right: Cartoon illustrating outward jet emission from the fireball surface and quenching of its inward-moving partner by the dense interior.

One can further quantify this by comparing the area under both near- and far-side peaks of the azimuthal correlation function (after subtracting elliptic flow) with the corresponding areas in p+p collisions. Figure 39 shows the ratio of these areas for the near-side peak as squares and for the far-side peak as circles. For very peripheral Au+Au collisions both ratios are close to, but slightly less than 1. The reduction below 1 can be understood as a trigger effect [180]. As the Au+Au collisions become more central (i.e. N_{part} increases), the near-side correlations seem to increase, in particular for lower values of the trigger- p_\perp , which may indicate an incomplete subtraction of elliptic flow effects. The away-side correlations, on the other hand, get weaker in less peripheral collisions and completely vanish in central collisions. If the elliptic flow were larger than assumed in the subtraction, this would bring down both the near- and far-side correlation strength, rendering the disappearance of the far-side jets even more dramatic.

The interpretation suggested by these data is indicated by the cartoon in the right part of Figure 39: The high- p_\perp trigger hadron identifies a jet moving outward from the fireball. The yield of these high- p_\perp hadrons scales by a factor $N_{part}^{-1/3} \propto 1/R_{fireball}$ more weakly than expected from perturbation theory, so these outward-moving jets come only from a thin surface layer. Fast partons created in the interior and trying to move out, as well as the inward-moving partners of the observed outward-moving jets, lose so much energy in the dense medium that they no longer make hadrons with $p_\perp > 2$ GeV which are included in the angular correlation function. (If they still produced hadrons with $p_\perp > 2$ GeV and had lost no energy but only their angular correlation with the fast trigger particle, the total yield at high p_\perp should still scale with N_{coll} , i.e. R_{AA} should be 1.)

This amounts to “complete jet suppression”: The hot and dense medium (which we know from Sec. 4 must be a thermalized QGP) suppresses all jets from fast partons except for a small fraction being produced near the surface and moving outward. Since in jet fragmentation the leading hadron carries on average about half the p_{\perp} of the hard parton, a trigger hadron with a p_{\perp} between 4 and 6 GeV/c corresponds to $p_{\perp} \simeq 10$ for both primary partons. The complete disappearance of the far-side jet in central Au+Au collisions requires the far-side parton to lose at least 6 GeV of momentum such that its fragments are all below the 2 GeV/c cut imposed on the angular correlation function. The energy lost by these partons thus becomes part of the thermalized and hydrodynamically expanding medium at $p_{\perp} < 2$ GeV/c.

So here is our **Fifth Lesson**: The quark-gluon plasma strongly suppresses jets. Inward-moving partons with $p_{\perp} \lesssim 10$ GeV don’t make it to the opposite edge and become part of the low- p_{\perp} “thermal soup”. Only outward-moving jets formed near the fireball surface survive. The era of JET (Jet Emission Tomography) of the quark-gluon plasma has begun: by investigating the A -, b - and emission-angle dependence of the far-side jet suppression and combining it with information extracted from soft particle emission we should be able to accurately determine the fireball conditions (density and temperature) in the early stage.

8 CONCLUSIONS AND DISCLAIMERS

The title of these lectures has been “Concepts in Heavy-Ion Physics”, but these lecture notes do not give a comprehensive overview of all the relevant concepts. In 3×75 minutes one simply can’t cover everything. Notable omissions include (I give references to good recent reviews) J/ψ suppression [181] as well as direct photon and thermal dilepton emission [13, 182]. While RHIC has not yet produced sufficient data on the first two of these items, J/ψ suppression has been a hot subject at the SPS, and some very interesting signals were also seen in the photon and dilepton spectra [10, 183]. I also omitted a more detailed discussion of the very interesting quark-coalescence approach to the production of hadrons at intermediate transverse momenta ($1.5 \text{ GeV}/c < p_{\perp} < 6 \text{ GeV}/c$) where some really nice systematics has been discovered which strongly indicates that in this kinematic region quark counting rules, causing a meson-baryon splitting of the elliptic flow and hadron yields instead of the hydrodynamic mass splitting observed at lower p_{\perp} [184]. I may include a more detailed discussion of these topics in some future lecture notes.

Relativistic heavy-ion physics is making progress in huge strides. These lectures have taught us a few important lessons which, I think, are now solidly established, but with the steady stream of RHIC data new, smaller lessons are being taught to us by Nature every week and keep complementing the picture literally as I sit here writing these notes. (Just compare these notes and the many new data I present here with the copied transparencies distributed at the summer school! And this write-up doesn’t even mention everything that happened during the last year ...) Nevertheless, let me repeat once more what I think are the important and firm conclusions one can draw at this point in time (note that, in spite of the new evidence and significantly improved data, these still agree with what I said at the school over a year ago):

- The heavy-ion reaction zone undergoes violent explosion; this proves the existence of strong thermal pressure and intense rescattering of the quanta produced in the collision. The bulk of the hadron data at $p_{\perp} < 2$ GeV is well described by hydrodynamics, and decoupling occurs at $T_f \approx 100 - 120$ MeV with average transverse flow $\langle \beta_T \rangle \approx 0.5 - 0.6$ (\implies “The Little Bang”).
- The measured elliptic flow in non-central collisions almost exhausts the hydrodynamic upper limit. This provides stringent limits on the time scale for thermalization, $\tau_{\text{therm}} < 1$ fm/c, and shows that the quark-gluon plasma is a strongly coupled fluid and thermalization in the QGP is controlled by non-perturbative processes.
- At τ_{therm} the energy density of the thermalized system exceeds the critical value for quark deconfinement by more than an order of magnitude. Hence, this thermalized state must be a Quark-Gluon

Plasma. At RHIC energies, the QGP lives for about 5–7 fm/c before hadronizing. At the time of hadron formation the elliptic flow has already saturated.

- Soft hadronization at $T_{\text{crit}} \approx 170$ MeV is a statistical process which generates a chemical equilibrium distribution. This equilibrium is not due to kinetic processes involving inelastic scattering between hadrons, but the result of a statistical formation process following the principle of maximum entropy. Due to rapid expansion and dearth of inelastic processes among hadrons, the hadronic chemical composition decouples immediately. Therefore the critical temperature for hadronization $T_{\text{cr}} = T_{\text{chem}}$ can be extracted from the final hadron yields. One finds $T_{\text{cr}} \approx 170$ MeV, confirming lattice QCD predictions.
- The QGP induces strong energy loss for high- p_{\perp} partons. Partons with $p_{\perp} \lesssim 10$ GeV which travel inward through the fireball lose enough energy to become indistinguishable from the soft hadron background (“complete” jet quenching). Only outward-moving surface jets are emitted, explaining why high- p_{\perp} hadron production ($p_{\perp} \leq 8$ GeV) is found to scale $\propto N_{\text{part}}$ instead of $\propto N_{\text{coll}} \propto N_{\text{part}}^{4/3}$ as perturbatively expected.

ACKNOWLEDGEMENTS

I would like to thank the summer school organizers for their warm hospitality and for creating a wonderful summer school spirit. I am grateful to M. van Leeuwen, Ziwei Lin, K. Reygers and Th. Ullrich for help with some of the figures. I would also like to thank Nick Ellis for his constant prodding and his patience with my slow writing. I hope it was worth it! This work was supported in part by the U.S. Department of Energy under Grant DE-FG02-01ER41190.

References

- [1] F. Karsch, Nucl. Phys. A **698** (2002) 199c.
- [2] Z. Fodor and S.D. Katz, JHEP **03** (2002) 014.
- [3] K.K. Szabo and A.I. Toth, JHEP **0306** (2003) 008.
- [4] F. Karsch and E. Laermann, Phys. Rev. D **50** (1994) 6954.
- [5] F. Karsch, private communication, based on work presented in F. Karsch, E. Laermann, and A. Peikert, Nucl. Phys. B (Proc. Suppl.) **83-84** (2000) 390; Phys. Lett. B **478** (2000) 447; and in A. Peikert’s PhD thesis (unpublished). See also Fig. 10 in Ref. [6]
- [6] F. Karsch and E. Laermann, “Thermodynamics and in-medium hadron properties from lattice QCD”, in *Quark-Gluon Plasma 3*, R.C. Hwa and X.N. Wang (Eds.) (World Scientific, Singapore, 2004), p. 1 [arXiv:hep-lat/0305025].
- [7] U. Heinz, P.R. Subramanian, H. Stöcker, and W. Greiner, J. Phys. G **12** (1986) 1237.
- [8] K. Rajagopal, Comments Nucl. Part. Phys. A **2** (2002) 120 [arXiv:hep-ph/0009058].
- [9] D.H. Rischke, Prog. Part. Nucl. Phys. **52** (2004) 197.
- [10] see <http://cern.web.cern.ch/CERN/Announcements/2000/NewStateMatter/> and U. Heinz, M. Jacob, arXiv:nucl-th/0002042.
- [11] M. Gyulassy, I. Vitev, X.N. Wang, and B.W. Zhang, “Jet quenching and radiative energy loss in dense nuclear matter”, in *Quark-Gluon Plasma 3*, R.C. Hwa and X.N. Wang (Eds.) (World Scientific, Singapore, 2004), p. 123 [arXiv:nucl-th/0302077].

- [12] T. Matsui and H. Satz, Phys. Lett. B **178** (1986) 416.
- [13] P.V. Ruuskanen, “Photons and lepton pairs: The deep probes of quark-gluon plasma”, in: *Particle Production in Highly Excited Matter*, H.H. Gutbrod and J. Rafelski (Eds.), NATO ASI Series B: Physics Vol. **303** (1993) 593 (Plenum, New York).
- [14] R. Hagedorn, Nuovo Cim. Suppl. **3** (1965) 147.
- [15] F. Becattini and U. Heinz, Z. Phys. C **76** (1997) 269.
- [16] J. Rafelski and B. Müller, Phys. Rev. Lett. **48** (1982) 1066 [Erratum-ibid. **56** (1986) 2334].
- [17] J. Rafelski, Phys. Rept. **88** (1982) 331.
- [18] E. Schnedermann, Z. Phys. C **64** (1994) 85.
- [19] J. Sollfrank, P. Koch, and U. Heinz, Z. Phys. C **52** (1991) 593.
- [20] E. Schnedermann, J. Sollfrank, and U. Heinz, Phys. Rev. C **48** (1993) 2462.
- [21] K.J. Eskola, K. Kajantie, and J. Lindfors, Nucl. Phys. B **323** (1989) 37.
- [22] K.J. Eskola, K. Kajantie, P.V. Ruuskanen, and K. Tuominen, Nucl. Phys. B **570** (2000) 379.
- [23] B. Andersson, G. Gustafson, G. Ingelman, and T. Sjöstrand, Phys. Rept. **97** (1983) 31.
- [24] L.V. Gribov, E.M. Levin, and M.G. Ryskin, Phys. Rept. **100** (1983) 1.
- [25] A.H. Mueller and J.W. Qiu, Nucl. Phys. B **268** (1986) 427.
- [26] L.D. McLerran and R. Venugopalan, Phys. Rev. D **49** (1994) 2233 and 3352.
- [27] Y.V. Kovchegov and A.H. Mueller, Nucl. Phys. B **529** (1998) 451
- [28] E. Iancu, A. Leonidov, and L. McLerran, “The colour glass condensate: An introduction”, in *QCD perspectives on hot and dense matter*, J.-P. Blaizot and E. Iancu (Eds.), NATO Science Series II: Mathematics, Physics, and Chemistry, Vol. **87** (2002) 73 (Kluwer, Dordrecht, The Netherlands) [arXiv:hep-ph/0202270].
- [29] Y.V. Kovchegov, Nucl. Phys. A **692** (2001) 557.
- [30] K. Geiger, Phys. Rept. **258** (1995) 237.
- [31] D. Molnar and M. Gyulassy, Phys. Rev. C **62** (2000) 054907.
- [32] H.T. Elze and U. Heinz, Phys. Rept. **183** (1989) 81.
- [33] R. Baier, A.H. Mueller, D. Schiff, and D.T. Son, Phys. Lett. B **502** (2001) 51.
- [34] A.H. Mueller and D.T. Son, Phys. Lett. B **582** (2004) 279.
- [35] S. Jeon, Phys. Rev. D **52** (1995) 3591.
- [36] P. Arnold, G.D. Moore, and L.G. Yaffe, JHEP **0305** (2003) 051.
- [37] G. Aarts and J.M. Martinez Resco, Phys. Rev. D **68** (2003) 085009.
- [38] S.A. Bass *et al.*, Phys. Rev. C **60** (1999) 021902.
- [39] D. Teaney, J. Lauret, and E.V. Shuryak, arXiv:nucl-th/0110037.

- [40] D. Teaney, J. Lauret, and E.V. Shuryak, Nucl. Phys. A **698** (2002) 479.
- [41] J.D. Bjorken, Phys. Rev. D **27** (1983) 140.
- [42] F. Cooper and G. Frye, Phys. Rev. D **10** (1974) 186.
- [43] P.V. Ruuskanen, Acta Phys. Pol. **18** (1987) 551.
- [44] U. Heinz, K.S. Lee, and E. Schnedermann, “Hadronization of a Quark-Gluon Plasma”, in *Quark-Gluon Plasma*, R.C. Hwa (Ed.) (World Scientific, Singapore, 1990), p. 471.
- [45] K.S. Lee, U. Heinz, and E. Schnedermann, Z. Phys. C **48** (1990) 525.
- [46] T. Peitzmann, Eur. Phys. J. C **26** (2003) 539.
- [47] E. Schnedermann, J. Sollfrank, and U. Heinz, “Fireball spectra”, in: *Particle production in highly excited matter*, H.H. Gutbrod and J. Rafelski (eds.), NATO Asi Series B Vol. **303** (1993) 175 (Plenum Press, New York).
- [48] U. Mayer and U. Heinz, Phys. Rev. C **56** (1997) 439.
- [49] E. Schnedermann and U. Heinz, Phys. Rev. C **50** (1994) 1675.
- [50] P.F. Kolb, J. Sollfrank, and U. Heinz, Phys. Lett. B **459** (1999) 667.
- [51] U. Heinz and P.F. Kolb, Phys. Lett. B **542** (2002) 216.
- [52] P.J. Siemens and J.O. Rasmussen, Phys. Rev. Lett. **42** (1979) 880.
- [53] R. Scheibl and U. Heinz, Phys. Rev. C **59** (1999) 1585.
- [54] M. van Leeuwen *et al.* (NA49 Collab.), Nucl. Phys. A **715** (2003) 161c.
- [55] O. Barannikova and F. Wang *et al.* (STAR Collaboration), Nucl. Phys. A **715** (2003) 458c.
- [56] J.M. Burward-Hoy *et al.* (PHENIX Collaboration), Nucl. Phys. A **715** (2003) 498c.
- [57] W. Broniowski and W. Florkowski, Acta Phys. Polon. B **33** (2002) 1935.
- [58] P.F. Kolb and U. Heinz, “Hydrodynamic description of ultrarelativistic heavy-ion collisions”, in *Quark-Gluon Plasma 3*, R.C. Hwa and X.N. Wang (Eds.) (World Scientific, Singapore, 2004), p.634 [arXiv:nucl-th/0305084].
- [59] P.F. Kolb, J. Sollfrank, and U. Heinz, Phys. Rev. C **62** (2000) 054909.
- [60] J.-Y. Ollitrault, Phys. Rev. D **46** (1992) 229.
- [61] T. Hirano, K. Morita, S. Muroya, and C. Nonaka, Phys. Rev. C **65** (2002) 061902.
- [62] K. Morita, S. Muroya, C. Nonaka, and T. Hirano, Phys. Rev. C **66** (2002) 054904.
- [63] P.F. Kolb, P. Huovinen, U. Heinz, K. Eskola, and K. Tuominen, Nucl. Phys. A **696** (2001) 175.
- [64] U. Heinz and P.F. Kolb, “Two RHIC puzzles: Early Thermalization and the HBT Problem”, in *Proceedings of the 18th Winter Workshop on Nuclear Dynamics, Nassau, Bahamas, Jan. 20-27, 2002*, (G.D. Westfall and W. Bauer, eds.), EP Systema, Debrecen, Hungary (2002), p. 205 [arXiv:hep-ph/0204061].
- [65] J. Velkovska *et al.* (PHENIX Collaboration), Nucl. Phys. A **698** (2002) 507.

- [66] C. Adler *et al.* (STAR Collaboration), Phys. Rev. Lett. **87** (2001) 262302.
- [67] M. Calderon de la Barca Sanchez, “Charged Hadron Spectra in Au+Au Collisions at a Centre-of-Mass Energy of 130 GeV”, Ph.D. Thesis, arXiv:nucl-ex/0111004.
- [68] P. Braun-Munzinger, D. Magestro, K. Redlich, and J. Stachel, Phys. Lett. B **518** (2001) 41.
- [69] K. Adcox *et al.* (PHENIX Collaboration), Phys. Rev. Lett. **88** (2002) 242301.
- [70] D. Teaney, arXiv:nucl-th/0204023.
- [71] R. Rapp, Phys. Rev. C **66** (2002) 017901.
- [72] T. Hirano and K. Tsuda, Phys. Rev. C **66** (2002) 054905.
- [73] P.F. Kolb and R. Rapp, Phys. Rev. C **67** (2003) 044903.
- [74] C. Suire *et al.* (STAR Collaboration), Nucl. Phys. A **715** (2003) 470c.
- [75] P. Huovinen, P.F. Kolb, U. Heinz, P.V. Ruuskanen, and S.A. Voloshin, Phys. Lett. B **503** (2001) 58.
- [76] H. van Hecke, H. Sorge, and N. Xu, Phys. Rev. Lett. **81** (1998) 5764.
- [77] H. Sorge, Phys. Rev. Lett. **78** (1997) 2309.
- [78] P.F. Kolb and U. Heinz, Nucl. Phys. A **715** (2003) 653c.
- [79] H. Sorge, Phys. Rev. Lett. **82** (1999) 2048.
- [80] B. Zhang, M. Gyulassy, and C.M. Ko, Phys. Lett. B **455** (1999) 45.
- [81] D. Molnar and M. Gyulassy, Nucl. Phys. A **697** (2002) 495, Erratum-ibid. A **703** (2002) 893; Nucl. Phys. A **698** (2002) 379.
- [82] K.H. Ackermann *et al.* (STAR Collaboration), Phys. Rev. Lett. **86** (2001) 402.
- [83] K. Adcox *et al.* (PHENIX Collaboration), Phys. Rev. Lett. **89** (2002) 212301.
- [84] C. Adler *et al.* (STAR Collaboration), Phys. Rev. Lett. **87** (2001) 182301.
- [85] S. Esumi *et al.* (PHENIX Collaboration), Nucl. Phys. A **715** (2003) 599c; S.S. Adler *et al.* (PHENIX Collaboration), Phys. Rev. Lett. **91** (2003) 182301.
- [86] P. Sorensen *et al.* (STAR Collaboration), J. Phys. G **30** (2004) S217; J. Adams *et al.* (STAR Collaboration), Phys. Rev. Lett. **92** (2004) 052302.
- [87] D. Molnar and S.A. Voloshin, Phys. Rev. Lett. **91** (2003) 092301.
- [88] U. Heinz and P.F. Kolb, Nucl. Phys. A **702** (2002) 269.
- [89] Y.V. Kovchegov and K.L. Tuchin, Nucl. Phys. A **708** (2002) 413.
- [90] N. Borghini, P.M. Dinh, and J.-Y. Ollitrault, Phys. Rev. C **63** (2001) 054906.
- [91] N. Borghini, P.M. Dinh, and J.-Y. Ollitrault, Phys. Rev. C **64** (2001) 054901.
- [92] C. Adler *et al.* (STAR Collaboration), Phys. Rev. C **66** (2002) 034904.
- [93] C. Adler *et al.* (STAR Collaboration), Phys. Rev. Lett. **90** (2003) 032301.

- [94] D. Teaney, Phys. Rev. C **68** (2003) 034913.
- [95] U. Heinz and S.M.H. Wong, Phys. Rev. C **66** (2002) 014907.
- [96] U. Ornik, M. Plümer, B.R. Schlei, D. Strottman, and R.M. Weiner, Phys. Rev. C **54** (1996) 1381.
- [97] C. Alt *et al.* (NA49 Collaboration), Phys. Rev. C **68** (2003) 034903.
- [98] J. Slivova *et al.* (CERES/NA45 Collaboration), Nucl. Phys. **A715** (2003) 615.
- [99] B.B. Back *et al.* (PHOBOS Collaboration), Phys. Rev. Lett. **89** (2002) 222301.
- [100] T. Hirano, Phys. Rev. C **65** (2001) 011901(R).
- [101] U. Heinz and P.F. Kolb, J. Phys. G **30** (2004) S1229.
- [102] U. Heinz and B.V. Jacak, Ann. Rev. Nucl. Part. Sci. **49** (1999) 529.
- [103] U.A. Wiedemann and U. Heinz, Phys. Rept. **319** (1999) 145.
- [104] R.M. Weiner, Phys. Rept. **327** (2000) 249.
- [105] B. Tomášik and U.A. Wiedemann, “Central and non-central HBT from AGS to RHIC”, in *Quark-Gluon Plasma 3*, R.C. Hwa and X.N. Wang (Eds.), p. 715 (World Scientific, Singapore, 2004) [arXiv:hep-ph/0210250].
- [106] R. Hanbury Brown and R.Q. Twiss, Phil. Mag. **45** (1954) 663, and Nature **178** (1956) 1046.
- [107] U. Heinz, in *Correlations and Clustering Phenomena in Subatomic Physics*, M.N. Harakeh *et al.*, (eds.), NATO ASI Series **B359** (1997) 137 (Plenum, New York) [arXiv:nucl-th/9609029].
- [108] U. Heinz, P. Scotto, and Q.H. Zhang, Annals Phys. **288** (2001) 325.
- [109] U. Heinz and Q.H. Zhang, Phys. Rev. C **56** (1997) 426.
- [110] J. Adams *et al.* (STAR Collaboration), Phys. Rev. Lett. **91** (2003) 262301.
- [111] T. Csörgő, B. Lörstad, and J. Zimányi, Z. Phys. C **71** (1996) 491.
- [112] U.A. Wiedemann and U. Heinz, Phys. Rev. C **56** (1997) 3265.
- [113] S. Pratt, T. Csörgő, and J. Zimányi, Phys. Rev. C **42** (1990) 2646.
- [114] S. Chapman, J.R. Nix, and U. Heinz, Phys. Rev. C **52** (1995) 2694.
- [115] H. Heiselberg and A.P. Vischer, Phys. Lett. B **421** (1998) 18; and Eur. Phys. J. C **1** (1998) 593.
- [116] B. Tomášik and U. Heinz, arXiv:nucl-th/9805016; and Acta Phys. Slov. **49** (1999) 251.
- [117] T. Csörgő and B. Lörstad, Phys. Rev. C **54** (1996) 1390.
- [118] M. Herrmann and G.F. Bertsch, Phys. Rev. C **51** (1995) 328.
- [119] B.R. Schlei, U. Ornik, M. Plümer, and R.M. Weiner, Phys. Lett. B **293** (1992) 275.
- [120] S. Chapman and U. Heinz, Phys. Lett. B **340** (1994) 250.
- [121] B. Tomášik, U.A. Wiedemann, and U. Heinz, Heavy Ion Phys. **17** (2003) 105.
- [122] Z.W. Lin, C.M. Ko, and S. Pal, Phys. Rev. Lett. **89** (2002) 152301.

- [123] D.H. Rischke and M. Gyulassy, Nucl. Phys. A **608** (1996) 479.
- [124] C. Adler *et al.* (STAR Collaboration), Phys. Rev. Lett. **87** (2001) 082301.
- [125] K. Adcox *et al.* (PHENIX Collaboration), Phys. Rev. Lett. **88** (2002) 192302.
- [126] A. Enokizono *et al.* (PHENIX Collaboration), Nucl. Phys. A **715** (2003) 595c; S.S. Adler *et al.* (PHENIX Collaboration), arXiv:nucl-ex/0401003.
- [127] S. Soff, S.A. Bass, and A. Dumitru, Phys. Rev. Lett. **86** (2001) 3981.
- [128] L.D. McLerran and S.S. Padula, arXiv:nucl-th/0205028, Nucl. Phys. A, in press.
- [129] D. Molnar and M. Gyulassy, Phys. Rev. Lett. **92** (2004) 052301.
- [130] A. Dumitru, arXiv:nucl-th/0206011.
- [131] U.A. Wiedemann, Phys. Rev. C **57** (1998) 266.
- [132] M.A. Lisa, U. Heinz, and U.A. Wiedemann, Phys. Lett. B **489** (2000) 287.
- [133] U. Heinz, A. Hummel, M.A. Lisa, and U.A. Wiedemann, Phys. Rev. C **66** (2002) 044903.
- [134] A. Hummel, M.Sc. Thesis, Ohio State University, 2002, unpublished.
- [135] N. Borghini and J.-Y. Ollitrault, arXiv:nucl-th/0407041.
- [136] U. Heinz, Acta Phys. Polon. B **35** (2004) 29.
- [137] F. Retiere and M.A. Lisa, arXiv:nucl-th/0312024.
- [138] M.A. Lisa *et al.* (E895 Collaboration), Phys. Lett. B **496**, 1 (2000).
- [139] J. Adams *et al.* (STAR Collaboration), Phys. Rev. Lett. **93** (2004) 012301.
- [140] E.T. Jaynes, Phys. Rev. **106** (1957) 620; *ibid.* **108** (1957) 171.
- [141] C. Slotta, J. Sollfrank, and U. Heinz, “Rapidity dependence of strange particle ratios in nuclear collisions”, in *Strangeness in Hadronic Matter*, J. Rafelski (Ed.), AIP Conf. Proc. **340** (1995) 462.
- [142] J. Letessier, A. Tounsi, U. Heinz, J. Sollfrank, and J. Rafelski, Phys. Rev. D **51** (1995) 3408.
- [143] U. Heinz, J. Phys. G **25** (1999) 263.
- [144] F. Becattini, Z. Phys. C **69** (1996) 485.
- [145] F. Becattini, M. Gaździcki, and J. Sollfrank, Eur. Phys. J. C **5** (1998) 143.
- [146] G. van Buren *et al.* (STAR Collaboration), Nucl. Phys. A **715** (2003) 129c.
- [147] P. Braun-Munzinger, J. Stachel, J.P. Wessels, and N. Xu, Phys. Lett. B **344** (1995) 43.
- [148] U. Heinz, Nucl. Phys. A **661** (1999) 140.
- [149] F. Becattini, M. Gaździcki, and J. Sollfrank, Nucl. Phys. A **638** (1998) 403c.
- [150] J. Adams *et al.* (STAR Collaboration), Phys. Rev. Lett. **92** (2004) 112301.
- [151] R. Lietava *et al.* (WA97 Collaboration), J. Phys. G **25** (1999) 181 (see p.460 in the same volume for the correct Fig. 7!).

- [152] J. Sollfrank, F. Becattini, K. Redlich, and H. Satz, Nucl. Phys. A **638** (1998) 399c.
- [153] J. Rafelski, Phys. Lett. B **262** (1991) 333; A. Bialas, Phys. Lett. B **442** (1998) 449.
- [154] S.A. Bass, A. Dumitru, M. Bleicher, L. Bravina, E. Zabrodin, H. Stöcker, and W. Greiner, Phys. Rev. C **60** (1999) 021902; and S.A. Bass, private communication.
- [155] R. Rapp and E.V. Shuryak, Phys. Rev. Lett. **86** (2001) 2980; C. Greiner and S. Leupold, J. Phys. G **27** (2001) L95.
- [156] C.R. Allton *et al.*, Phys. Rev. D **66** (2002) 074507.
- [157] J. Adams *et al.* (STAR Collaboration), Phys. Rev. Lett. **91** (2003) 172302.
- [158] M. Gyulassy, P. Levai, and I. Vitev, Phys. Lett. B **538** (2002) 282.
- [159] J.D. Bjorken, Fermilab-Pub-82/59-THY, Batavia (1982); and Erratum (unpublished).
- [160] M. Gyulassy and M. Plümer, Phys. Lett. B **243** (1990) 432; M. Gyulassy and X.N. Wang, Nucl. Phys. B **420** (1994) 583; X.N. Wang, M. Gyulassy and M. Plümer, Phys. Rev. D **51** (1995) 3436.
- [161] R. Baier, Y.L. Dokshitzer, S. Peigne, and D. Schiff, Phys. Lett. B **345** (1995) 277; R. Baier, Y.L. Dokshitzer, A.H. Mueller, S. Peigne and D. Schiff, Nucl. Phys. B **483** (1997) 291; and *ibid.* B **484** (1997) 265.
- [162] R. Baier, Nucl. Phys. A **715** (2003) 209c.
- [163] M. Gyulassy, P. Levai, and I. Vitev, Phys. Rev. Lett. **85** (2000) 5535; Nucl. Phys. B **594** (2001) 371.
- [164] P. Levai, G. Papp, G. Fai, M. Gyulassy, G.G. Barnafoldi, I. Vitev, and Y. Zhang, Nucl. Phys. A **698** (2002) 631c.
- [165] D. Kharzeev and M. Nardi, Phys. Lett. B **507** (2001) 121.
- [166] D. Antreasyan, J.W. Cronin, H.J. Frisch, M.J. Shochet, L. Kluberg, P.A. Piroue, and R.L. Sumner, Phys. Rev. D **19** (1979) 764.
- [167] X.N. Wang, Phys. Rev. C **61** (2000) 064910.
- [168] A.L.S. Angelis *et al.*, Phys. Lett. B **185** (1987) 213.
- [169] M.M. Aggarwal *et al.* (WA98 Collaboration), Eur. Phys. J. C **23** (2002) 225.
- [170] K. Adcox *et al.* (PHENIX Collaboration), Phys. Rev. Lett. **88** (2002) 022301.
- [171] S.S. Adler *et al.* (PHENIX Collaboration), Phys. Rev. Lett. **91** (2003) 072301.
- [172] K. Reygers, talk presented at 8th International Conference on Nucleus-Nucleus Collisions, June 17-21, 2003, Moscow, available at <http://www.phenix.bnl.gov/conferences.html>
- [173] I. Vitev and M. Gyulassy, Nucl. Phys. A **715** (2003) 779c.
- [174] T. Peitzmann, Nucl. Phys. A **715** (2003) 349c.
- [175] B.B. Back *et al.* (PHOBOS Collaboration), Phys. Lett. B **578** (2004) 297.
- [176] S.S. Adler *et al.* (PHENIX Collaboration), Phys. Rev. Lett. **91** (2003) 072303.

- [177] J. Adams *et al.* (STAR Collaboration), Phys. Rev. Lett. **91** (2003) 072304.
- [178] D. Kharzeev, E. Levin, and L. McLerran, Phys. Lett. B **561** (2003) 93.
- [179] C. Adler *et al.* (STAR Collaboration), Phys. Rev. Lett. **90** (2003) 082302.
- [180] D. Hardtke, private communication.
- [181] H. Satz, Rept. Prog. Phys. **63** (2000) 1511.
- [182] C. Gale, Nucl. Phys. A **698** (2002) 143c.
- [183] U. Heinz, Nucl. Phys. A **685** (2001) 414.
- [184] B. Müller, “Hadronic signals of deconfinement at RHIC”, in *New Discoveries at RHIC – The Strongly Interactive QGP*, T.D. Lee and N.P. Samios (Eds.), RBRC Scientific Articles, Vol. 9, p. 77 (Brookhaven National Laboratory, 2004) [arXiv:nucl-th/0404015].